



ISAS - INTERNATIONAL SCHOOL FOR ADVANCED STUDIES

Large Scale Structure and Cosmic Microwave Background Anisotropies as tests of Dark Matter Models

Thesis submitted for the degree of
Doctor Philosophiæ

Astrophysics Sector

Candidate:

ELENA PIERPAOLI

Supervisors:

LUIGI DANESE

SILVIO BONOMETTO

Acknowledgments

This Thesis and more generally all my work of these years has been possible because of the concurrence of many different events.

Not only it is due to my commitment, but also to the opportunities I had to get involved in different activities. Therefore, I would like to thank Prof. Danese for introducing me into the Planck project, which is by far one of the most promising experiments of the near future. Because of that, I also had the possibility to meet different scientists, and to approach very different arguments and methods. I consider this a great advantage I had, and it has been possible because of his constant support.

While staying at SISSA, I still collaborated with Milano University. Most of the work presented in the Thesis is the result of a long—duration collaboration with Prof. Bonometto. He introduced me to the theory of perturbations, and to the issues related to structure formation. Not only I should thank him for that, but also for allowing me to use Milano University facilities with no restrictions, as a long-term visitor. I take this opportunity to thank him for something that dates a long time ago, that is the enthusiasm he transferred me for science, which certainly concurred in my decision of undertaking this not easy path, four years ago.

SISSA is an environment where people of different disciplines can easily get in contact and exchange expertises. I personally had some exchanges with the particle physics sector, and particularly I would like to acknowledge Prof. Masiero for the collaboration opportunity he gave me and more generally for his ever open attitude in exchanging knowledges.

A special thank goes to Dr. Borgani for the fruitful (although unfortunately unconstant) collaborations we had during these years. He taught me a lot, with enthusiasm and generosity. I hope our ways will continue to cross, at least in the unplanned way of these years.

More in general, I would like to thank all the people I worked with during these

years, in particular the people I got in contact with because of the Planck project. They are too many to mention, but any single collaboration was an opportunity of human and scientific exchange.

I would also like to thank all the staff of the astrophysics sector, because in more than one occasion I could see that they were ready to help me even if I was not directly a member of their research group or involved in their research activities.

My work here in SISSA has been supported by the effort of the computer center staff, the secretaries and all the personnel that ensured an efficient environment. I greatly appreciated all their prompt helpfulness in many occasions, and I hope they realize how essential they are for our work.

SISSA is a unique place also because all the continents are shrunk here, under the excuse of science. The result is a unique atmosphere where not only you learn science, but also you constantly revise your *Weltanschauung*. I enjoyed this environment very much, and I believe I learned a lot also under this point of view.

Finally, there is a special ensemble of people I still would like to thank.

Like in any performance, most of the people who made it possible don't appear on the scene, but quietly stand behind. Let them stay there. They don't need official acknowledgements: they are already satisfied because they know how much they were involved in each single experience of my past years.

– D'ora in avanti sarò io a descrivere le città, – aveva detto il Kan. – Tu nei tuoi viaggi verificherai se esistono.

Ma le città visitate da Marco Polo erano sempre diverse da quelle pensate dall'imperatore.

– Eppure io ho costruito nella mia mente un modello di città da cui dedurre tutte le città possibili, – disse Kublai. – Esso racchiude tutto quello che risponde alla norma. Siccome le città che esistono si allontanano in vario grado dalla norma, mi basta prevedere le eccezioni alla norma e calcolare le combinazioni più probabili.

– Anch'io ho pensato un modello di città da cui deduco tutte le altre, – rispose Marco. – E' una città fatta solo di eccezioni, (...). Se una città così è quanto c'è di più improbabile, diminuendo il numero degli elementi abnormi si accrescono le probabilità che la città ci sia veramente. Dunque basta che io sottragga eccezioni al modello, e in qualsiasi ordine proceda arriverò a trovarmi davanti una delle città che, pur sempre in via d'eccezione, esistono. Ma non posso spingere la mia operazione oltre un certo limite: otterrei delle città troppo verosimili per essere vere.

Table of Contents

Table of Contents	i
Introduction	1
1 The Unperturbed Universe	9
1.1 Introduction	9
1.2 The Einstein equations	9
1.3 The cosmological constant	11
1.4 Thermal history of the Universe	13
1.5 Inflation	15
1.5.1 Primordial spectral index from inflation	16
1.6 Dark Matter candidates	19
1.6.1 Gravitinos	22
1.6.1.1 Computation of g_*	25
1.6.2 Neutrinos	26
1.6.3 Volatile particles	28
2 Anisotropies: Linear theory	33
2.1 Introduction	33
2.2 The metric and Einstein equations	33
2.2.1 Gauge choice	34
2.3 Unperturbed distribution of Volatile Dark Matter	35
2.4 Perturbed distribution function for Volatile particles	37
2.5 Thermally-distributed particles	43
2.6 Equations for radiation massless neutrinos, cold and baryonic matter	44
2.7 Equations for the gravitational field	45
2.8 Final equations	49
2.9 Initial conditions	51

2.9.1	Volatile dark matter	51
2.9.2	Gravitinos	53
2.10	Technical issues	54
3	Power Spectra	57
3.1	Introduction	57
3.2	The matter power spectrum	57
3.2.1	Gravitino WDM	61
3.2.2	Volatile dark matter with radiative decay	64
3.2.3	Volatile dark matter with non-radiative decay	67
3.3	The radiation spectrum	76
3.4	Effects of dark matter content on the CMB	78
3.4.1	CMB spectra for volatile models	80
4	Comparison with Observations	87
4.1	Introduction	87
4.2	The mass variance and the shape parameter	88
4.2.1	Bulk Velocities	90
4.2.1.1	Volatile particles and bulk flows	91
4.3	Press-Schechter theory	91
4.3.1	Cluster abundance	93
4.3.2	High-redshift objects	94
4.4	Volatile models with radiative decay	96
4.4.1	Cluster abundance	96
4.4.2	High-redshifts objects	97
4.5	Volatile particles with non-radiative decay	100
4.5.1	Relations between different constraints	101
4.6	Constraining volatile models	102
4.6.1	Volatile particles with radiative decay	102
4.6.2	Volatile models with non-radiative decay	103
4.6.3	Volatile models compared to CMB experiments	108
4.6.4	Summary on volatile models	112
4.7	Light gravitinos warm dark matter	114
	Summary and Conclusions	123
	Bibliography	129

Introduction

This thesis deals with perturbation evolution in cosmologies characterized by different mixture of dark matter components, aiming both to predict the expected Cosmic Microwave Background (CMB) features and to analyze the linear theory of density fluctuations.

There can be scarce doubts that, in the last ten billions years, fluctuations in the energy density of the Universe have attained a non-linear regime, up to scales of several Mpcs. However, non-linearity can be a powerful eraser of initial conditions and the great efforts put to simulate non-linear evolution, over an increasingly wide dynamical range, still provides us with a limited set of model dependent predictions. Large scale structure and CMB anisotropies can be studied already at a linear level, with a theory which is highly predictive and model discriminatory.

In this framework, our original contribution concerns the predictions for radiation and matter power spectrum in a class of mixed dark matter models (volatile models) and in some variants of warm dark matter models. In both cases, predictions have also been compared with available data, in order to constrain the parameters of the models.

The interest of this study resides in the fact that, in the past years, a number of observations provided new information on the spatial distribution of matter on large scale. At the same time, after COBE discovery of anisotropies in the microwave background, many balloon-borne experiments provided the amplitude of anisotropies on smaller scales. Therefore, the combination of detections of anisotropy in the CMB and observations of the large-scale structure distribution of galaxies can now probe the primordial density fluctuations on spatial scales varying by three orders of magnitude, ranging from ~ 1 to 1000 Mpc with a superposition of the two kinds of data on scales of ~ 100 Mpc.

Moreover, CMB became recently very attractive because of the future missions MAP and Planck, which will certainly be very powerful in determining the basic

cosmological parameters. However, even with the impressing spatial resolution and spectral coverage of the Planck satellite, CMB data analysis alone can leave some ambiguity in the determination of cosmological parameters, since the contemporary variation of different parameters can have compensating effects on the predicted power spectrum. In this respect, a joint analysis of large scale structure and CMB is desirable.

As long as the nature of dark matter is concerned, the angular power spectrum of the radiation is affected by different kinds of dark matter already at angular scales $l \sim 200$. Typical differences with standard cold dark matter (CDM) are lower than 10% in the power spectrum, up to $l \sim 500$. This precision will be definitely attained with the future space missions. However, we shall see that in volatile models CMB predictions differ much more significantly from CDM, so that present CMB data can already be used to draw some conclusions on their parameter space.

As long as the matter power spectrum is concerned, different dark matter contents lead to very different predictions, and therefore very different scenarios for structure formation.

Moreover, the dark matter nature is related to high-energy physics. The possibility that structure formation depends on the nature of hot or warm components is to be explored also as a tool to provide high-energy physics data, which may be complementary to the results attained with laboratory experiments.

In this thesis two different class of dark matter models are studied in detail: the volatile dark matter model and the gravitino warm dark matter model.

Volatile models are characterized by a dark matter component coming from an early decay of a heavy particle. The first motivation for this work came from particle physics, because we were interested in studying the cosmological implications of a model in which the neutralino, an already well known cold dark matter candidate, decays into an axino and a photon. The decay-produced axino would behave more like a hot dark matter component, and, together with a thermal relics of axinos providing a cold component, would give rise to a mixed dark matter scenario.

The (axino) volatile model appeared appealing for several reasons. Firstly, it allowed to obtain a cold and a hot component with the same particle, therefore avoiding the problem of a fine-tuning between the abundance of particles with very different nature providing the hot and the cold dark matter. Secondly, the power spectra of volatile models have the characteristic of providing smaller power on high scales if compared to CDM, just as cold + hot dark matter (CHDM) models, also referred to as *mixed models*, with stable massive neutrinos providing the hot

component. Mixed models are actually among the best dark matter models in reproducing the observed large scale structure. Soon after COBE results, it became clear that the standard cold dark matter (CDM) scenario predicts too much power on small scale when a normalization to large scales is performed. Adding a hot component to the cold one is a way of subtracting power on small scale, while leaving the large scale unaffected. Recent analyses that take into account also the CMB data confirm the mixed models as preferable ones [1].

However, in CHDM models mentioned above, the abundance of the hot component is univocally linked to the mass of the hot dark matter particle, and therefore to the redshift at which the hot component typically become non-relativistic. Here, owing to the production mechanism of the hot component, the abundance of the hot component Ω_h and its derelativization redshift z_{nr} can be varied almost independently, giving rise to a wider set of possible power spectra. Scale invariant power spectra were normalized to COBE results, compared to the available phenomenological ones and used to predict observable quantities like bulk velocities, number of clusters and high redshift damped Lyman- α systems. Comparing predictions with available data, we found a preferred subset in the parameter space for $\Omega_h \simeq 0.2$ and $z_{nr} \simeq 2 \times 10^4 \Omega_h$.

Following a similar pattern, we extended our analysis to volatile models in which the decay give rise to a hot dark matter particle and a sterile scalar. Firstly, we analyzed the features of the power spectra of these models with respect to the standard neutrino CHDM ones, and then we compared model predictions with both large scale structure and CMB data, allowing also the primordial spectral index n to vary. In particular, owing to COBE determination of the spectral index, we considered the consequences of taking $n \geq 1$. Besides the independence of abundance and derelativization redshift cited above, these models differ from usual CHDM models with massive neutrinos mainly for two reasons: the hot dark matter component has a different phase-space distribution and the background radiation is higher due to the presence of the sterile scalar. We analyzed the impact of these two aspects on both the radiation and matter power spectrum, and found that the latter causes the main differences with respect to the neutrino CHDM case. The presence of the sterile component implies equivalence to be shifted towards lower redshifts. As a consequence, the matter power spectrum is further damped on small scales, when the same normalization on big scales is performed. For the same reason, the first doppler peak in the radiation power spectrum is higher than in CDM and CHDM models. This feature goes in the direction of alleviating the problems that CDM

and CHDM models have in matching the results of Saskatoon experiment.

A detailed analysis has been performed in order to restrict the space parameter $\Omega_h - z_{der}$, for different values of n . Considering large scale structure data only, we found that the most stringent linear constraint arises from fitting the extra-power parameter Γ . Other significant constraints arise comparing the expected abundances of galaxy clusters and high- z systems with observational data. If low values of Γ are permitted, mixed models with $1 \leq n \leq 1.4$ can have up to $\sim 45\%$ of non-cold component, without violating any further linear constraint. Keeping to models with $\Gamma \geq 0.13$, a suitable part of the parameter space still allows up to $\sim 30\%$ of hot component. It is worth pointing out that the effect of a late equivalence on the matter power spectrum is similar to the one obtained by tilting the initial power spectrum to values $n < 1$. On the contrary, the effect on the radiation power spectrum is a higher doppler peak, which mimes the effect of an $n > 1$. For this reason, while large scale structure can be fitted by taking simultaneously a low derelativization redshift z_{der} (down to $\simeq 600$) and a high n , CMB data from balloon-borne experiment implies a severe selection on this part of the parameter space. Therefore $n \gtrsim 1.3$ seems excluded by balloon-borne experiment outputs, while a good fit of almost all CMB and large scale structure data is found for Ω_h values between 0.11 and 0.16, $n \sim 1.1$ and $z_{der} \sim 2000-5000$. A smaller n is allowed, but z_{der} should never be smaller than $\simeq 1200$.

The impact of having a different distribution function for the hot component has been investigated comparing volatile models with *technical* CHDM models in which extra degrees of freedom have been added to the massless neutrinos to account for the extra-radiation caused by the sterile scalar in volatile models. The difference is of the order of a few percent at maximum on all scales both in the radiation power spectrum and in the matter one. While in the matter power spectrum this difference is very tiny, and not appreciable with experiments, such a precision may be attained in the future CMB experiments.

A further model presented in this thesis considers a light gravitino as the constituent of dark matter. The gravitino is the lightest supersymmetric particle in gauge-mediated supersymmetry breaking (GMSB) models. According to particle physics predictions, its mass can vary a lot, from a fraction of eV to O(GeV), depending on the SUSY breaking scale. However, when the relic number density of gravitinos is computed, it is found that a gravitino with mass higher than ~ 1 keV would overclose the Universe. On the other hand, a much too light gravitino would contribute to the overall energy density for a tiny fraction, and therefore would be

cosmologically irrelevant. For these reasons, we analyzed the formation of cosmic structures in models where the gravitino have a mass of $100 \text{ eV} - 1 \text{ keV}$. These gravitinos were once in equilibrium with radiation and therefore their phase-space distribution have a thermal origin. In this respect, they are similar to the standard candidate of hot dark matter, i.e. the stable massive neutrino. After evaluating the number of degrees of freedom at the gravitinos decoupling (g_*), we computed the transfer function for matter fluctuations and show that gravitinos behave like warm dark matter (WDM) with free-streaming scale comparable to the galaxy mass scale. It is already known that just replacing the cold component with a warm one in the standard CDM scenario does not provide a viable scenario for the formation of cosmic structures[2]. In fact, the effect of introducing the warm component is that of suppressing fluctuations only at the galaxy mass scale, while leaving the power spectrum unaffected on the cluster mass scales, where standard CDM fails.

Therefore, if we desire a GMSB scheme to provide the dominant DM content of the Universe, we need some prescriptions to improve the WDM scenario. To this purpose, we analyzed what happens if we followed the same pattern as for improving CDM, namely either adding a hot neutrino component or lowering the density parameter. Our analysis focused on the interesting class of GMSB schemes, although many of our conclusions may equally well apply to models with a generic WDM other than the light gravitino.

The purpose of our analysis was twofold. On one hand, given the success of suitable CHDM and low-density CDM models in accounting for several observational constraints (in particular providing a low level of density fluctuations at the $10h^{-1}\text{Mpc}$ scale to avoid cluster overproduction, while having enough power at about $1h^{-1}\text{Mpc}$ to form galaxies at an early enough epoch), we asked whether the agreement can be kept when a warm gravitino component replaces the cold candidate. On the other hand, from a more particle physics oriented point of view, we would like to make use of the cosmological constraints related to the DM issue to infer constraints on the GMSB models, in particular shedding some light on the range of the allowed (or at least cosmologically favoured) scales of SUSY breaking in this class of theories.

We considered different low-density variants of the WDM model, both with and without cosmological constant, and compare the predictions on the abundances of neutral hydrogen within high-redshift damped Ly- α systems and on the number density of local galaxy clusters with the corresponding observational constraints. We found that none of the models satisfies both constraints at the same time, un-

less a rather small Ω_0 value ($\lesssim 0.4$) and a rather large Hubble parameter ($\gtrsim 0.9$) is assumed. Furthermore, in a model with warm + hot dark matter, with hot component provided by massive neutrinos, the strong suppression of fluctuation on scales of $\sim 1 h^{-1}\text{Mpc}$ precludes the formation of high-redshift objects, when the low- z cluster abundance is required. We concluded that all different variants of a light gravitino DM dominated model show strong difficulties for what concerns cosmic structure formation. This result gives a severe cosmological constraint on the gauge-mediated SUSY breaking scheme. Given the difficulties that gravitinos present with respect to structure formation, we didn't consider necessary to analyze the CMB predictions.

This is the content of the thesis. However, this is only a fraction of the work that I carried out during these years. A relevant portion of my time has been dedicated to the Planck project. Namely, I performed the simulations of high-resolution CMB all-sky maps that were used to simulate the future observations. A first result of this work concerns the effects of beam distortions on the anisotropies measurements, and it is presented in ref. [3]. More recently, I have been studying the problem of the deconvolution of different processes from the observed images. Multi-wavelength information is a crucial point in this analysis, because different processes have a different frequency dependence. Moreover, also statistical knowledges on the spatial distribution of emitting sources and eventual correlations among them can be taken into account. Therefore, suitable techniques that make use of all these information should be considered. Already developed techniques are the generalized Wiener filtering and the maximum entropy method. These techniques however currently apply to small portions of the sky and work in Fourier space. An all sky analysis is desirable, which can eventually take into account the local characteristics of some processes, both for frequency dependence and spatial distribution. I investigated the possibility of using wavelet transform to this aim. This work is still in progress, and is not presented here.

The thesis is organized as follows:

- Chapter one is dedicated to an introduction of notations, and to a general presentation the dark matter candidates that are then investigated. Neutrinos are reviewed, since they are by far the most famous dark matter candidates, especially after the recent Super-Kamiokande results. Moreover, they are often used as a reference scenario. Other dark matter candidates, like gravitinos and volatile particles, are also presented. A section is dedicated to inflation, with particular care to the predictions that it implies on the primordial spectral index n .
- Chapter two provides a derivation of the relevant equations that are needed to

study the evolution of perturbations in linear theory. The derivation is performed for the volatile models, and final equations are given for all the models presented.

– Chapter three introduces the basic tools that are needed for the comparison with the data at a linear stage. The spectra of the models are presented and discussed.

– Chapter four is dedicated to the comparison of the models to the observations.

A final summary and discussion of the results conclude this thesis.

1 The Unperturbed Universe

1.1 Introduction

In this Chapter we summarize the fundamental assumptions and observational evidences of the background cosmology and we introduce some notations that will be useful in the following Chapters. We present a brief thermal history of the Universe, which is a fundamental link between particle physics and cosmology. A special care is dedicated to inflation, mainly because of its implications on fluctuation power spectrum. The last part of the Chapter is dedicated to the dark matter candidates in general, and specifically to the ones whose implications on structure formation has been studied in detail (i.e. gravitinos, volatile particles and neutrinos).

1.2 The Einstein equations

The Universe is described in the four-dimensional space. Each *event* is labelled with three spatial coordinates x^i ($i = 1, 2, 3$) and the proper time t measured by a clock in the rest-frame of the point P of coordinates x^i . The metric

$$ds^2 = g_{\alpha\beta} x^\alpha x^\beta \quad (\alpha, \beta = 0, 1, 2, 3) \quad (1.1)$$

represents the distance in the four-dimensional space between two events whose coordinates are x^α and $x^\alpha + dx^\alpha$. Under the assumption of isotropy and homogeneity, the expression:

$$ds^2 = (cdt)^2 - dl^2 = (cdt)^2 - a(t)^2 \left[\frac{dr^2}{1 - Kr^2} + r^2(d\theta^2 + \sin^2\theta d\phi^2) \right] \quad (1.2)$$

represents the metric in its most general form. In the above expression, dl is the distance measured at a time t , $a(t)$ is the expansion parameter¹ and (r, θ, ϕ) are co-

¹we recall here the definition of *redshift* $1 + z = \frac{a_0}{a}$. In the rest of this thesis the redshift z will therefore be used as a synonym of expansion rate. The value of a_0 is conventionally taken equal to 1.

moving coordinates, while K represents the curvature of the Universe ($K = 0, +1, -1$ for a flat, closed and open Universe respectively).

General Relativity allows to relate the metric tensor $g_{\alpha\beta}$ to the energy content of the Universe. The link is provided by the Einstein equations:

$$R_{\alpha\beta} - \frac{1}{2}g_{\alpha\beta}R - \Lambda g_{\alpha\beta} = \frac{8\pi G}{c^4}T_{\alpha\beta} \quad (1.3)$$

where $R_{\alpha\beta}$ is the Ricci tensor ($R = g^{\alpha\beta}R_{\alpha\beta}$), Λ is the cosmological constant, G is the gravitational constant and c is the speed of light and $T_{\alpha\beta}$ is the energy-momentum tensor. For a perfect fluid the energy-momentum tensor is:

$$T_{\alpha\beta} = (p + \rho c^2)U_\alpha U_\beta - pg_{\alpha\beta} \quad (1.4)$$

where p and ρc^2 are pressure and energy density respectively, while U_α is the four-velocity of the fluid ($U_\alpha = g_{\alpha\nu} \frac{dx^\nu}{ds}$).

From the above expression one can easily deduce the Friedman equations:

$$\dot{a}^2 + Kc^2 = \frac{8\pi G}{3}\rho a^2 + \frac{\Lambda a^2}{3} \quad (1.5)$$

$$\ddot{a} = -\frac{4\pi G}{3}\left(\rho + 3\frac{p}{c^2}\right)a + \frac{\Lambda a}{3} \quad (1.6)$$

Eqns.(1.5) and (1.6) describe the evolution of $a(t)$, once the equation of state $p(\rho)$ is given.

A general equation of state of the kind

$$p = w\rho c^2 \quad (1.7)$$

is adequate to describe both the pressureless matter ($p = w = 0$) and a relativistic fluid in thermal equilibrium ($w = 1/3$).

Two fundamental parameters for the description of the evolution of the Universe are the Hubble parameter $H(t)$ and the matter content Ω_o . The Hubble parameter is defined as $H(t) = \frac{\dot{a}}{a}$ and its actual value $H(0) = H_o$ is usually expressed by means of the dimensionless parameter $h = H_o/(100 \text{ Km/s Mpc}^{-1})$, whose determination is still quite uncertain, allowing a range $0.5 \lesssim h \lesssim 0.85$ [4]. Ω_o is defined as

$$\Omega_o = \frac{\rho_{o,m}}{\rho_{o,cr}} = \frac{\rho_o \pi G}{3H_o^2} \quad (1.8)$$

where

$$\rho_{o,cr} = 1.8788 \times 10^{-29} h^2 g \text{ cm}^{-3} \quad (1.9)$$

is the critical energy density, and $\rho_{o,m}$ is the actual matter density. In the rest of this thesis the abundance of different components (label i) will be parametrized by $\Omega_i \equiv \frac{\rho_i}{\rho_{o,cr}}$. In the case $\Omega_o = 1$ (and zero cosmological constant), usually referred to as Einstein–de Sitter Universe, eqns.(1.5) and (1.6) allow the simple solutions:

$$a \propto t^{2/3} \quad (if \ w = 0) \quad (1.10)$$

and

$$a \propto t^{1/2} \quad (if \ w = 1/3). \quad (1.11)$$

Since the CMB is closed to a blackbody with a very high precision ([5, 6]) and its temperature is well established, the actual radiation energy density is easily computed:

$$\rho_{o,r} = \frac{\sigma T_{o,r}^4}{c^2} = 2.0154 \times 10^{-34} \theta^4 g \ cm^{-3} \quad (1.12)$$

or, equivalently:

$$\Omega_{o,r} = \frac{\rho_{o,r}}{\rho_{cr}} = 2.4888 \times 10^{-5} h^{-2} \theta^4 \quad (1.13)$$

where we put by definition:

$$\theta = T/2.73 \ K. \quad (1.14)$$

The Universe is now matter dominated, and the radiation doesn't contribute significantly to the actual energy density. Because of the different rate of growth, going back in time the radiation energy density overcomes the matter energy density. The redshift at which matter–radiation equivalence is reached is

$$z_{eq} = 4.0180 \times 10^4 (\Omega_o h^2) \theta^{-4} \quad (1.15)$$

if only photons are considered in the radiation content, or

$$z_{eq} = 2.3898 \times 10^4 (\Omega_o h^2) \theta^{-4} \quad (1.16)$$

if 3 massless neutrinos are also taken into account. If other species than photons and neutrinos contribute to the radiation, z_{eq} can be even lower. We shall see that this situation is realized in some volatile models.

1.3 The cosmological constant

The cosmological constant, introduced a long time ago by Einstein, is an additional term in the equations for the expansion factor $a(t)$.

The presence of a cosmological constant in the Einstein equations has two main consequences, namely on dynamics of the Universe and on structure formation (for a nice review on the cosmological constant see [7]). Although disregarded for a long time by cosmologists, the cosmological constant is now receiving much attention because many different observational evidencies suggest that it is different from zero. Recent evidencies in favour of a cosmological constant come from the high-redshift supernovae measurements [8], and similar experiments are now carried out by two separate groups [9, 10]. These measurements aim to evaluate the deceleration parameter $q_o \equiv -(a\ddot{a}/\dot{a}^2)_o$, that is related to Ω_o and Ω_Λ by the relation $q_o = \frac{1}{2}\Omega_o - \Omega_\Lambda$. In particular, [10] claim that if $\Omega_o + \Omega_\Lambda = 1$, then $\Omega_o < 0$ at 95 % C.L., with a best estimate $\Omega_o = -0.1 \pm 0.5$, if $\Omega_\Lambda = 0$. This result is quite impressive, since Ω_o is clearly positive by definition. Other evidencies come from double radio sources [11] and CMB measurements. The latter in particular are suited to measure $\Omega_o + \Omega_\Lambda$, and therefore may help to break the degeneracy in the $\Omega_o - \Omega_\Lambda$ plane, when considered together with supernovae results. The actual estimate of the cosmological constant constant with CMB measurements is compatible with supernovae results [12].

Another important issue related to the presence of a cosmological constant is the measurements of the age of the Universe and of H_0 .

The dynamical effect of the cosmological constant is visible at low redshifts, because in the early Universe the density of radiation and matter is far more important than the Λ term in Friedman equations. Therefore, let us consider for a moment a dust dominated universe with pressure $p = 0$. The continuity equation then reduces to $(4\pi/3)\rho a^3 = M = \text{const}$. The Friedmann equation reads:

$$\dot{a} = \frac{2GM}{a} - kc^2 + \frac{\Lambda c^2 a^2}{3}.$$

Integrating the equation above, one can see that the effect of Λ on the age of the Universe is to make it longer than in both cases ($\Omega_o = 1, \Lambda = 0$) and ($\Omega_o < 1, \Lambda = 0$), for a given value of H_0 . Therefore the presence of a cosmological constant may help to reconcile the quite high recent estimates of the age of the Universe ($\gtrsim 12 \text{ Gyr}$ s, [13]) with $h \gtrsim 0.5$, as H_0 determinations seem to suggest.

In a flat Universe with cosmological constant, the expansion slows down at low redshifts because the attraction of the matter and the repulsion represented by the cosmological constant tend to balance. After this stage, the cosmological constant dominates causing an accelerated expansion corresponding to an inflationary Universe. This happens when $1 + z \lesssim (2\Omega_\Lambda / \Omega_o)^{1/3}$. To give an example, in a

Universe with $\Omega_o = 0.3$, the cosmological constant start to dominate at $z \sim 0.6$. The existence of a period in which the expansion greatly slows down while the time increase not only has the effect of causing a greater t_0 , but also implies that there is a higher probability of finding galaxies at the redshift interval when the expansion slowed down, and consequently an increased opportunity for lensing of quasars by these galaxies. The observed lensed quasars are quite compatible with an $\Omega_o = 1$ Universe, and so they allow to put quite stringent limits on the value of Λ : $\Omega_\Lambda \leq 0.70$ at 90% C.L. [14], and $\Omega_\Lambda \leq 0.66$ at 95% C.L. if $\Omega_\Lambda + \Omega_o = 1$ is imposed [15].

Despite the number of evidencies in favour of a cosmological constant, we must say that they are all very recent, and therefore may not be completely settled down and accepted by the cosmological community. In the work presented in this thesis, both models with and without cosmological constant have been considered, in particular the presence of a cosmological constant have been envisaged for the gravitino dark matter, as a hope of reconciling prediction with the data. When dealing with volatile models, we kept $\Lambda = 0$, since our analysis already let many parameters to vary, and the presence of a cosmological constant could make the analysis less clear.

1.4 Thermal history of the Universe

In the previous sections we described the dynamics of the Universe. There are evident proofs that the Universe is expanding. Going back in time, the radiation temperature increases, and therefore we expect other particles to be in thermal equilibrium with it.

The thermal equilibrium is provided by the fact that the reaction rates of particles in the thermal bath is much greater than the expansion rate.

They can be either bosons or fermions, which are characterized by a different phase-space distribution:

$$f(\vec{p}) = [\exp((E - \mu)/T_i \pm 1)]^{-1}$$

where E is the energy, μ is the chemical potential of the species, while $+1$ and -1 correspond to Fermi-Dirac and Bose-Einstein species.

From the above expression, it is easy to compute the energy density and pressure at a given temperature.

Assuming that at a certain moment there are different relativistic species, the total radiation and pressure density can be expressed by:

$$\rho_r = \frac{\pi^2}{30} g_* T^4$$

$$p_r = \rho_r/3 = \frac{\pi^2}{90} g_* T^4.$$

The parameter g_* denotes the effective number of degrees of freedom :

$$g_* = \sum_{i=\text{bosons}} g_i \left(\frac{T_i}{T} \right)^4 + \frac{7}{8} \sum_{i=\text{fermions}} g_i \left(\frac{T_i}{T} \right)^4$$

where g_i denotes the internal degrees of freedom of the i species.

Note that bosons and fermion contribute to the overall energy density with a different weight, because of their phase-space distribution.

Note also that g_* is also a function of the T , since in the sum only relativistic particles are included (i.e. it must be $m_i \ll T$).

If only photons and massless (or very light) neutrinos are considered as particles that contribute to the radiation, then the value of g_* is 3.36 (here also the difference between the neutrino and photon temperature has been taken into account).

Going back in time, g_* remains constant until electron-positron annihilation is possible, at $T \geq 1 \text{ MeV}$. For $1 \text{ MeV} \leq T \leq 100 \text{ MeV}$, $g_* = 10.75$, taking into account the electron-positron annihilation, and that $T_\nu = T_\gamma$ at that energies.

The maximum number of degrees of freedom within the standard model is attained at temperatures $T \geq 300 \text{ GeV}$, when all the species contribute to the radiation density. At that time, we have $g_* = 106.75$.

However, many efforts in particle physics are concentrated in building a physics *beyond the standard model*. Supersymmetry (SUSY) is a possible extension, and it has often received attention by cosmologist because some SUSY particles are dark matter candidates. If a supersymmetric theory holds, at early times the value of g_* can be higher than 106.75, the maximum depending upon the number of supersymmetric particles of the theory.

As long as interactions among particles occur frequently enough, the Universe evolves through a series of thermal equilibrium states. This happens if the interaction rate per particle, $\Gamma = n\sigma|v|$ (n being the number density of target particles, σ the cross section of the interaction and $|v|$ the relative velocity), is greater of the expansion rate: $\Gamma \geq H$.

However, note that a massless non-interacting particle which has been once in thermal equilibrium, will conserve the thermal phase-space distribution in time, with a temperature $T \propto a^{-1}$.

With the physics we know, we can't describe the thermal history of the Universe up to very early times, since a much developed quantum-relativistic theory would

be required. A limit is set by the Planck scales: $m_{Pl} = 2.18 \times 10^{-5} \text{g}$, or $T_{Pl} = 1.22 \times 10^{19} \text{GeV}$.

At such early times the Universe was a plasma made of quarks, leptons, gauge bosons and Higgs bosons. As temperature went down, a number of successive symmetry breaking phase transitions took place.

At temperatures between 10^{14} and 10^{16}GeV the grand Unification phase transition took place (GUT), while electroweak phase transition occurred at lower temperatures, around $T \sim 300 \text{GeV}$. During these phase transitions some of the gauge bosons acquire mass via the Higgs mechanism, and the interactions that they mediate will be characterized by a coupling strength G_X . Particles that are subject only to these interactions will decouple from the thermal bath at a temperature $T \sim G_X^{-2/3} m_{Pl}^{-1/3}$. The Peccei–Quinn symmetry breaking eventually occurs when $10^9 \lesssim T \lesssim 10^{12} \text{GeV}$.

At much lower temperatures, between 100 and 300 MeV , quark-hadron transition occurs: after this time quark and antiquark are confined into baryons and mesons.

Nucleosynthesis takes place when the temperature $T \sim 10 - 0.1 \text{MeV}$, while at $T \sim 0.1 \text{eV}$ the Universe recombines.

These two last stages are of crucial importance for modern cosmology, also because they can be directly tested with observations.

Nucleosynthesis implies specific ratios between light element abundances, and can be tested looking at high-redshifts objects; the recombination epoch is tested via CMB observations.

1.5 Inflation

We refer to an inflationary era when the expansion factor has a positive acceleration, $\ddot{a} > 0$.

The hypothesis that the Universe underwent an inflationary era was introduced a long time ago [16], and many variants of the first concept have immediately been proposed [17, 18]. The inflationary mechanism soon acquired importance because it seemed it could give an explanation to the shortcomings of the Big Bang cosmology. The basic idea of inflation is that there was an epoch when the vacuum energy of a field ϕ (the inflaton field, with potential $V(\phi)$) was dominating the energy density of the Universe. The equation of motion of such a field is:

$$\ddot{\phi} + 3H\dot{\phi} + V'(\phi) = 0 \quad (1.17)$$

and its energy density and pressure are:

$$\rho = V + \frac{1}{2}\dot{\phi}^2 \quad (1.18)$$

$$\frac{p}{c^2} = -V + \frac{1}{2}\dot{\phi}^2 \quad (1.19)$$

and therefore if the field is evolving sufficiently slowly ($\dot{\phi}^2 \ll V$) we have that $\frac{3p}{c^2} < -\rho$. Since $\ddot{a} = -\frac{4\pi G}{3}\left(\rho + \frac{3p}{c^2}\right)a$, the above condition implies an accelerated expansion. From the Friedmann equations we can derive that during inflation the Hubble parameter H was (almost) constant, so that the expansion factor a was growing quasi-exponentially. This feature of inflation gives a possible explanation to the so called *horizon problem*, which poses the question of why the Universe is so smooth today even on very large scales. If inflation occurred, even scales that are now out of the horizon may have been in causal contact before the inflating era.

Another tempting feature of inflation is that it provides a mechanism for producing small density fluctuations in the early Universe (see [19] for a comprehensive review). In the inflationary paradigm, fluctuations in the matter-radiation fluid are generated by fluctuations in quantum fields during the inflationary phase.

Another well known prediction of inflation is that the curvature today almost vanishes. In fact, while during inflation the energy density was almost constant, the curvature radius grew exponentially, so that its value today still exceeds the present Hubble radius.

Finally, inflation may help in getting rid of heavy and stable relics (e.g. monopoles) produced before inflation and that would by now overclose the Universe. In fact, their number density scales as a^{-3} , and therefore it decays exponentially during inflation.

As long as structure formation is concerned, inflation is interesting because it provides a way of producing inhomogeneities in the early Universe (as well as gravitational waves, eventually). Here we shall discuss in more detail the predictions on the initial power spectrum for adiabatic density perturbations. After explaining the arguments for a scale-invariant spectrum $n = 1$, we shall show how models with $n \geq 1$ are feasible in the inflationary scenario. We present this case in detail because an $n \geq 1$ was considered while treating volatile models.

1.5.1 Primordial spectral index from inflation

According to the inflationary scenario, density perturbations originated during inflation as quantum fluctuations, and they become classical as they left the horizon.

Let us define $\delta_H(k)$ as the amplitude of the perturbation on a scale k at horizon (re)entry. It is normally assumed $\delta_H^2(k) \propto k^{n-1}$, so that for $n = 1$ all scales have the same amplitude when they enter the horizon. It is possible to link the primordial spectral index n with the potential of the inflaton field.

In particular, the following relation holds [20]:

$$\delta_H^2(k) = \frac{32}{75} \frac{V_*}{m_{Pl}^4} \epsilon_*^{-1} \quad (1.20)$$

where the subscript $*$ denotes the epoch of horizon exit of a scale k ($k = aH$). The quantity ϵ is related to the potential as follows:

$$\epsilon \equiv \frac{m_{Pl}^2}{16\pi} \left(\frac{V'}{V} \right)^2. \quad (1.21)$$

In most inflationary models, the second term in the equation of motion (1.17) balance the third one ($\dot{\phi} \simeq \frac{1}{3} H V'$) so that ϵ is small and positive. Another condition that is usually satisfied is that the absolute value of the quantity

$$\eta \equiv \frac{8\pi}{m_{Pl}^2} \frac{V''}{V} \quad (1.22)$$

is much smaller than one. From eq.(1.20) it is possible to deduce the following expression for n :

$$n = 1 + 2\eta - 6\epsilon \quad (1.23)$$

that, under the slow-roll conditions $|\eta| \ll 1$ and $\epsilon \ll 1$, states that inflation predicts a primordial spectral index close to 1. Since in one-field inflation ϵ is positive by definition, it is easier to get $n < 1$, but there are results in the literature which show that a wide class of inflationary models predict $n > 1$ (see, e.g. [21]), but $\lesssim 1.4$.

In order to get a more physical intuition, let us reexpress n in a different way. Keeping in mind that $n - 1 = \frac{d \log \delta_H^2}{d \log k}$ and that eq.(1.20) holds, the spectral index n can be related to the Hubble parameter H during inflation and to the speed $\dot{\phi}$ of the *slow-rolling-down* process, along the scalar field potential. The critical quantity is the ratio $W(k) = H^2/\dot{\phi}$, where H and $\dot{\phi}$ are taken at the time when the scale $2\pi/k$ leaves the event horizon. The value of the spectral index therefore is:

$$n = 1 + 2 \frac{d(\log W)}{d(\log k)} \quad (1.24)$$

and, if W (slowly) decreases with time, we have the standard case of n (slightly) below unity (it should be reminded that greater scales flow out of the horizon at

earlier times). This decrease is due to an acceleration of the downhill motion of ϕ and an opposite behaviour occurs if $\dot{\phi}$ decreases while approaching a minimum. In this scenario, the very last stages of inflation should rather see a significant ϕ -field acceleration, ending up into a regime of damped oscillations around the true vacuum, when reheating occurs.

Another possibility is that reheating does not arise when an initially smooth acceleration finally grows faster and faster, as the slope of the potential steepens; on the contrary, reheating starts abruptly, thanks to a first order phase transition, perhaps to be identified with the break of the GUT symmetry. Before such transition and since the Planck time, most energy content naturally resided in potential terms, so granting a vacuum-dominated expansion. This picture of the early stage of the cosmic expansion is the so-called *hybrid inflation*, initially proposed by Linde [22].

A toy-model realizing such scenario [23, 24] is obtained from the potential

$$V(\varphi, \chi) = (\mu^2 - \lambda\chi^2)^2 + 2g^2\varphi^2\chi^2 + m^2\varphi^2 \quad (1.25)$$

depending on the two scalar fields φ and χ , expected to be slowly and fastly evolving, respectively. If the slowly evolving field is embedded in mass terms, the potential reads

$$V(\chi) = M^2\chi^2 + \lambda\chi^4 + \Lambda^4 \quad (1.26)$$

where

$$\Lambda^4 = \mu^4 + m^2\varphi^2 \quad \text{and} \quad M^2 = 2(g^2\varphi^2 - \lambda\mu^2). \quad (1.27)$$

Eq. 1.26 shows that V has a minimum at $\chi = 0$, provided that $M^2 > 0$. If $M^2 < 0$, instead, the minimum is for $\bar{\chi} = \sqrt{-M^2/2\lambda}$, yielding μ when $\varphi = 0$.

Large φ values therefore require that χ vanishes and then the potential

$$V(\varphi, 0) = \mu^4 + m^2\varphi^2 \quad (1.28)$$

allows a Planck-time inflation, as φ rolls downhill taking V from an initial value $\sim t_{Pl}^{-4}$ to $\sim \mu^4$. This downhill motion is expected to decelerate when the second term at the r.h.s. of eq.1.28 becomes negligible in respect to μ^4 , which essentially acts as a cosmological constant. This deceleration abruptly breaks down when the critical value $\varphi_c = \sqrt{\lambda}\mu/g$ is attained, for which M^2 changes sign. At that point the configuration $\chi = 0$ is unstable and the transition to the true vacuum configuration $\bar{\chi}$ reheats (or heats) the Universe.

There are a number of constraints to the above picture, due to the requirements that at least 60 e-foldings occur with $\varphi > \varphi_c$ and that fluctuations have a fair

amplitude. Such constraints are discussed in several papers (see, *e.g.*, [25], and references therein) and cause the restriction $n \lesssim 1.4$.

Let us however outline that *hybrid* inflation is not just one of the many possible variations on the inflationary theme. In spite of the apparent complication of the above scheme, it is an intrinsically simple picture and one of the few patterns which can allow to recover a joint particle–astrophysical picture of the very early Universe, as was naturally hoped before it became clear that the Higgs’ field of the GUT transition could not be the inflaton [26, 27].

1.6 Dark Matter candidates

There are many astrophysical evidences for an $\Omega_o \geq 0.2$, with $\Omega_b \leq 0.1$.

This imply that the majority of the matter in the Universe is not made by atoms.

Two main possibilities are available: either the dark matter (DM) is constituted by massive compact objects like primordial black holes, neutron stars, jupiters, or dwarfs; or it is made of non-baryonic particles. The latter perspective is of interest also for the particle physicists world, since the Universe can be an ideal environment where to test theories that cannot be tested with actual laboratory experiment. In this paragraph we will therefore focus on this issue, giving an overview of the most attractive dark matter particle candidates. More attention will be devoted to some specific candidate in the next sections, since they where studied more in detail in the original work of this thesis.

The particle physics standard model is now a milestone since it passed several experimental tests, for example the gauge bosons W and Z has been discovered and the top quark has been found in the mass range expected by the electroweak radiative corrections. It is therefore clear that any possible extension of the standard model should reproduce it with great accuracy up to energies $\sim 100 \text{ GeV}$.

Nevertheless, many particle physicists are convinced that the standard model in not the whole story. The main motivations are that the standard model does not unify the elementary interactions (gravity, in particular, is left out), and it leaves problems with the fermion masses and mixing. Very recently (May 1998) the Super-Kamiokande team claimed to have found $5 \times 10^{-4} < \Delta m^2 < 6 \times 10^{-3} \text{ eV}^2$ from $\nu_\mu - \nu_\tau$ oscillations [28]. This news excited also the astrophysics world, because the standard model predicts null mass for neutrinos and leaves no room for extra relic massive particles besides (few) baryons, and therefore does not help in solving the dark matter problem, since there is no way to account for $\Omega_o \geq 0.1$. We can envisage two main particle physics candidates for DM: massive neutrinos and the

lightest supersymmetric particle (LSP).

The two best candidates we have to play the role of LSP are the lightest neutralino (i.e. the lightest among the fermionic partners of the neutral gauge and Higgs fields) and the gravitino (the fermionic partner of the graviton in the gravity multiplet) [29]. Which of the two is the actual LSP strictly depends on the mechanism one envisages for the SUSY breaking, or, more precisely, for the transmission of the breaking of SUSY from some hidden sector to the observable sector of the theory (ordinary particles and their superpartners belong to this latter sector). If the “messengers” of the SUSY breaking are of gravitational nature (as it happens in the more “orthodox” supergravity models), then the lightest neutralino is likely to be the LSP. In these schemes the gravitino mass sets the scale of SUSY breaking in the observable sector and, hence, it is expected to be in the $10^2 - 10^3$ GeV range. On the other hand, it has been vigorously emphasized recently (after ten years of silence about this alternative) that gauge, instead of gravitational interactions may be the vehicle for the transmission of the SUSY breaking information to the observable sector [30]. In these scenarios the scale of SUSY breaking is much lower than in the supergravity case and consequently, as we will see below, the gravitino mass is much lower than 10^2 GeV. Hence in this class of gauge mediated SUSY breaking (GMSB) models the gravitino is more likely to play the role of LSP with a mass which can range a lot, depending on the specific scale of SUSY breaking, say from a fraction of eV up to $O(\text{GeV})$. In gravity-mediated models with $m_{\tilde{G}} \sim 10^2 - 10^3$ GeV, we face the traditional gravitino cosmological problems [31, 32, 33, 34, 35]. Namely, unless gravitinos are strongly diluted at inflation and they are not regenerated in the reheating phase ($T_{reh} \lesssim 10^8$ GeV), they would spoil the canonical picture of big-bang nucleosynthesis (BBN).

On the other hand, if the gravitino is lighter than the neutralino, the latter is no longer stable, and decays to the gravitino. It was pointed out [36] that its decays would also destroy the BBN if its life time is sufficiently large. A limit on the life time depends on the abundances of the neutralinos before decay. We quote here a conservative bound of 10^6 sec as an upper bound for the life time of the neutralino from the BBN constraint.

Different dark matter candidates can lead to very different cosmological scenarios, that we schematically describe as hot dark matter (HDM), warm dark matter (WDM) and cold dark matter (CDM) scenarios .

Conventionally, hot dark matter refers to low-mass neutral particles that were still in thermal equilibrium after quark-hadron transition took place, and therefore

neutrinos, if massive, enters this category. Their number density is known and quite close to photon's one, therefore their mass is linked to their abundance by the relation: $\sum m_\nu = 93.625 \Omega_\nu h^2 \theta^{-3} \text{ eV}$, while the number of light neutrinos has been limited by particle accelerators experiment (LEP and CERN) to be $N_\nu = 2.993 \pm 0.011 (1\sigma)$ [37] for $m_\nu \leq m(Z^0) \simeq 46 \text{ GeV}$, in well agreement with Big Bang nucleosynthesis predictions ($N_\nu < 4$ taken as a conservative limit, for $m_\nu \leq 1 \text{ MeV}$). However, we will see in the next Chapters that HDM behaviour with respect to density fluctuations can be obtained even with other particles than neutrinos, namely SUSY particles coming from the decay of heavier ones. The characteristic of HDM is to erase by free-streaming any fluctuation below $\sim 10^{15} M_\odot$. Smaller structures, therefore, form by fragmentation of larger lumps.

Warm dark matter particles normally interact more weakly than neutrinos, therefore they decouple earlier and they are not heated by subsequent annihilation of hadronic species. Their number density is therefore lower (roughly an order or magnitude less than HDM) and their mass higher. Gravitinos, the fermionic partners of gravitons, can constitute the WDM component, provided that supersymmetry is broken at low energies. Another possible candidate is a right-handed (or sterile) neutrino. They both give rise to a scenario where the free-streaming scale is of the order of $10^{11} M_\odot$.

Cold dark matter, instead, is made of particles that are already non-relativistic when the smallest cosmologically relevant scale enters the horizon. Fluctuations aren't damped by free-streaming on any scale, and structures form in a bottom-up scenario. There are mainly two candidates for CDM, namely the axion and the neutralino. Axions are very light particles ($m \sim 10^{-5} \text{ eV}$) associated to the Peccei-Quinn symmetry, and they were never in thermal contact with radiation. The neutralino X^0 is a representative of the lightest SUSY particle for high-energy broken supersymmetry. There are lower bounds on neutralino masses of $m_{X^0} \geq 20 \text{ GeV}$. Neutralinos are kept in thermal equilibrium through the electroweak interactions even when the temperature is below their mass. As a consequence, their number density is therefore greatly lowered by the exponential Boltzmann factor. Their contribution to Ω_0 depends on their mass but also greatly on their decoupling temperature. For instance, if the X_0 results from a large mixing of the gaugino and higgsino components, the annihilation is too efficient to contribute to Ω_0 significantly. On the contrary, if the neutralino is a pure gaugino or higgsino, then there is a possibility that a sufficient number of neutralinos survive and account for a reasonable value of Ω_0 . Requiring an $\Omega_0 \leq 1$ leads to the restriction in the parameter space still allowed

by existing experimental constraints. This is a fruitful example of the interplay between particle physics and astrophysics, in the rest of this thesis we will focus on other results of this kind. To conclude the possible cold dark matter candidates, let us mention the recently proposed case of nonthermal supermassive (SUMO) dark matter with mass possibly larger than the grand-unification scale, and certainly of the electroweak scale [38]. SUMO dark matter resurrect the possibility is made of charged or even strongly interacting particles.

In the following, we will present more in detail the features of dark matter candidates that underlie the cosmological models extensively studied in the next Chapters. We refer here to gravitinos, neutrinos and volatile dark matter.

1.6.1 Gravitinos

In a supersymmetric model [39], each ordinary particle is associated with a superpartner. We assign R-parity even to the ordinary particles and odd to their superpartners. In supergravity, that is a natural extension of the supersymmetric standard models to the framework of local supersymmetry, we have another R-odd particle, the gravitino, which is the superpartner of the graviton. The lightest of the R-odd particles, namely the lightest superparticle, is absolutely stable, under the assumption of the R-parity conservation, which was originally introduced in order to avoid too fast proton decays. The LSP is thus a dark matter candidate, if its expected relic abundances lie within a suitable range of values.

As a starting point, we review some properties of the gravitino. The gravitino mass is related to the SUSY breaking scale Λ_{SUSY} as follows:

$$m_{\tilde{G}} = \frac{1}{\sqrt{3}} \frac{\Lambda_{SUSY}^2}{M_{Pl}}, \quad (1.29)$$

where M_{Pl} is the reduced Planck mass $\sim 2.4 \times 10^{18}$ GeV. On the other hand, the soft SUSY breaking masses for the superparticles are given as

$$m_{soft} \sim \frac{\Lambda_{SUSY}^2}{M}, \quad (1.30)$$

where M effectively represents the mass scale of the interactions that transmit the breakdown of SUSY in the hidden sector to the observable sector, the latter including particles of the SUSY standard model. We call M the messenger mass scale. In the conventional scenario of the gravity-mediated SUSY breaking, the transmission is due to gravitational interactions. In this case, the messenger mass scale is $M \sim M_{Pl}$, so that the gravitino mass will be comparable to the other soft masses. In order to

have the soft masses at the electro-weak scale the SUSY breaking scale should be at an intermediate scale $\sim \sqrt{m_W M_{Pl}}$.

On the other hand, one can consider the case where the SUSY breaking is transmitted by gauge interaction. The idea of the gauge mediation [40, 41, 42, 43, 44, 45] is older than the gravity-mediation, and has recently been revived with fruitful results [30, 46, 47]. In this case the gauge interaction can set the messenger mass scale much lower than the Planck mass. Since the soft masses are fixed at the electro-weak scale, the SUSY breaking scale can be much smaller than the intermediate scale of $\sqrt{m_W M_{Pl}}$. Correspondingly the gravitino can be much lighter than the other superparticles. Now a crucial question is: how light is the gravitino? The answer should depend on the details of the messenger of the SUSY breaking. In most of the gauge-mediated models, there are three independent sectors. They are the hidden sector, the messenger sector and the observable sector. The interaction between the last two sectors is the standard-model gauge interaction, so its strength is fixed. But the interaction between the first two is model dependent, so is the messenger mass scale. For example, in the original models of gauge-mediation [30, 46, 47] it was shown [48] that Λ_{SUSY} cannot be smaller than 10^7 GeV, the corresponding gravitino mass being $\sim 10^2$ keV. However, a lighter gravitino should be possible from viewpoints of both model building and phenomenology. In the SUSY gauge-mediated approach the soft masses arise at the loop level (to avoid the supertrace constraint [49]). Hence a lower bound on Λ_{SUSY} is provided by the relation

$$\Lambda_{SUSY} \gtrsim \frac{16\pi^2}{g^2} m_{soft} \quad (1.31)$$

where g is some gauge coupling constant. For instance, recently Izawa et al. [50, 51] have constructed a model where $m_{soft} \lesssim 0.1g^2/16\pi^2\Lambda_{SUSY}$. In this case, Λ_{SUSY} can be as small as $O(10^5)$ GeV for $m_{soft} = O(10^2)$ GeV. In view of the above consideration, in our work we consider the following gravitino mass range

$$1 \text{ eV} \lesssim m_{\tilde{G}} \lesssim \text{a few TeV}. \quad (1.32)$$

Suppose that the spin 1/2 components of gravitinos were in thermal equilibrium at an early epoch. As temperature went down, the processes which kept the gravitinos in equilibrium became ineffective and they decoupled from the thermal bath. After that, the number of gravitinos per comoving volume was frozen out. This freeze-out took place while the gravitinos were relativistic. Following a standard procedure [52], one can calculate the relic density of the gravitinos [53]

$$\Omega_{\tilde{G}} h^2 = 0.282 \text{ eV}^{-1} m_{\tilde{G}} Y_{\infty}$$

$$= 1.17 \left(\frac{100}{g_*} \right) \left(\frac{m_{\tilde{G}}}{10^3 \text{eV}} \right), \quad (1.33)$$

where $\Omega_{\tilde{G}}$ is the contribution of the (thermal) gravitinos to the density parameter and g_* stands for the effective degrees of freedom of relativistic particles when the freeze-out of the gravitinos takes place. Note that $g_* = 106.75$ for the full set of particle contents of the minimal standard model and $g_* = 228.75$ for those of the minimal supersymmetric standard model. Thus one expects that g_* at the freeze-out will fall somewhere in between the two numbers. The computation of g_* is a crucial point of our analysis and we will come back to it later on. For later convenience, we introduce the yield, Y_∞ , of the gravitinos, defined by

$$Y_\infty = \left(\frac{n_{\tilde{G}}}{s} \right)_\infty = \frac{0.617}{g_*}, \quad (1.34)$$

where $n_{\tilde{G}}$ is the number density of the gravitinos and s is the entropy density. The subscript ∞ means that the ratio is evaluated at a sufficiently late time (i.e., low temperature) at which it is constant.

We will first briefly discuss the case when the relic abundance of the gravitinos calculated in this way exceeds the closure limit, $\Omega_{\tilde{G}} \gtrsim 1$. This corresponds to the gravitino mass region $m_{\tilde{G}} \gtrsim 1 \text{ keV } (g_*/100)h^2$. In this case, as was discussed in refs. [36, 48], entropy production is needed to dilute the gravitino abundance in order not to overclose the Universe. To avoid an excessive reproduction of the gravitinos after the entropy production, its reheating temperature must be low; its upper bound varies from 10^3 to 10^8 GeV , depending on the gravitino mass. The lower the gravitino mass is, the lower the reheating temperature should be. If the reheating temperature happens to saturate the upper bound quoted above, the gravitinos will dominate the energy density of the Universe, and play the role of DM.

On the other hand, the low reheating temperature required by the closure limit leads to the question of how to generate the baryon asymmetry of the Universe. Since the reheating temperature can be still higher than the electro-weak scale, baryogenesis during the electro-weak phase transition may work for some region of the parameter space [54]. Another possibility is to use the Affleck-Dine mechanism, which was explored in detail in ref.[48] in the framework of the gauge-mediated SUSY breaking.

When the gravitino mass is smaller than $(g_*/100)h^2 \text{ keV}$, the thermal relic density of the gravitinos $\Omega_{\tilde{G}}$ is smaller than one. This is the region that we have studied in detail. As we discussed previously, models providing this range for the gravitino mass can be devised. It is also interesting to mention that a possible explanation of

the $ee\gamma\gamma$ event [55] at CDF by the light gravitino scenario [56, 57, 58, 59, 60, 61, 62] requires this range of gravitino mass; otherwise the neutralino would not decay into a photon and a gravitino inside the detector. A particularly interesting parameter region for cosmology is the region in which $0.1 \lesssim \Omega_{\tilde{G}} \lesssim 1$ is realized, and thus the gravitino mass density constitutes a significant portion of the density of the whole Universe. A DM particle with mass within the sub-keV to keV range may constitute the warm dark matter [63, 64, 65, 66, 67]. We will discuss scenarios of cosmic structure formation within a WDM dominated Universe in the following Chapters.

If, instead, the gravitino mass is as small as to give $\Omega_{\tilde{G}} \ll 0.1$, then it becomes cosmologically irrelevant and an alternative DM candidate is required.

1.6.1.1 Computation of g_*

In this section we come back to the question of g_* , the effective degree of freedom of relativistic particles at the freeze-out of gravitinos. Of particular interest is the region where $m_{\tilde{G}} \lesssim 1$ keV so that gravitinos of thermal origin dominate the energy density of the Universe. The crucial relevance of g_* lies in the fact that, for a specified value of $\Omega_{\tilde{G}} h^2$, it fixes the corresponding gravitino mass and, therefore, the free-streaming scale.

The production and destruction rates of the gravitinos due to scattering processes are proportional to the fifth power of the temperature and, therefore, their abundance rapidly drops down as the temperature decreases. Thus, decay and inverse decay processes are more important for a light gravitino whose freeze-out occurs at a rather low temperature [36].

In order to compute g_* , the following Boltzmann equation must be integrated:

$$\dot{n}_{\tilde{G}} + 3Hn_{\tilde{G}} = C, \quad (1.35)$$

where $n_{\tilde{G}}$ is the gravitino number density and H is the expansion rate of the Universe. As a collision term (C), we considered contributions from two body decay (and inverse decay) processes. A numerical integration of eq.(1.35) is necessary in order to take into account the continuous variation of the ratio between the collision rate and the expansion rate. Here we only present the results, addressing the reader to ref. [68] and its Appendix for further details. Results are summarized in Table 1.1. We show the value g_* for a range of model parameters. In this computation, we assumed a typical sparticle mass spectrum in a simple class of gauge-mediated models [69]. Explicitly, we take for the gauginos

$$M_1 = \frac{5}{3} \frac{\alpha_1}{4\pi} \Lambda_G, \quad M_2 = \frac{\alpha_2}{4\pi} \Lambda_G, \quad M_3 = \frac{\alpha_3}{4\pi} \Lambda_G, \quad (1.36)$$

(a)		$m_{\tilde{G}}$ (eV)					
$m_{\tilde{l}_R} = M_1$		10	50	100	200	500	1000
M_1 (GeV)	50	87	93	101	110	122	136
	100	87	89	93	111	114	124
	150	87	89	92	97	109	119
	200	88	90	93	97	105	115

(b)		$m_{\tilde{G}}$ (eV)					
$m_{\tilde{l}_R} = 2M_1$		10	50	100	200	500	1000
M_1 (GeV)	50	87	91	95	102	116	128
	100	87	90	93	98	107	116
	150	88	91	93	97	104	111
	200	88	92	94	98	103	108

Table 1.1: Value of effective degrees of freedom of relativistic particles, at the gravitino freeze-out, g_* , as a function of the gravitino mass $m_{\tilde{G}}$ and the $U(1)_Y$ gaugino mass M_1 . In the case (a) the right-handed slepton mass is $m_{\tilde{l}_R} = M_1$, and in (b) $m_{\tilde{l}_R} = 2M_1$.

and for the sfermion masses

$$m^2 = 2 \left[C_3 \left(\frac{\alpha_3}{4\pi} \right)^2 + C_2 \left(\frac{\alpha_2}{4\pi} \right)^2 + \frac{5}{3} \left(\frac{Y}{2} \right)^2 \left(\frac{\alpha_1}{4\pi} \right)^2 \right] \Lambda_S^2. \quad (1.37)$$

In the above expressions α_i is a gauge coupling constant in the standard model, Y is a hypercharge of $U_Y(1)$, while $C_3 = 4/3$ for a $SU(3)_C$ triplet, $C_2 = 3/4$ for a $SU(2)_L$ doublet, and 0 otherwise. Λ_G, Λ_S are introduced to parameterize the transmission of SUSY breaking from the messenger sector to the observable sector.² We provide g_* values for two cases: (a) the right-handed slepton mass $m_{\tilde{l}_R}$ equals to the bino mass M_1 , *i.e.* $m_{\tilde{l}_R} = M_1$, and (b) $m_{\tilde{l}_R} = 2M_1$. In both cases, we find that g_* is around 100 for a wide range of the parameter space. For a given $\Omega_{\tilde{G}}$, a lower value of g_* implies a lighter gravitino, making structure formations at small scales more difficult, as we will discuss in the following sections. The fact that g_* tends to lie in the lower side should be kept in mind, though we will explore a somewhat wider range for g_* .

²To avoid further complication, we set a light Higgs mass to be the Z^0 mass, and masses of heavier Higgs and higgsinos to be the same as the left-handed slepton mass. Furthermore we did not include D- or F-term contributions to the scalar masses. Also we ignored the mixing in the mass matrix of the neutralino and the chargino sector.

1.6.2 Neutrinos

Neutrinos are leptons and fermions. According to the standard model, they are massless.

This feature, however, is not dictated by an underlying principle, such as gauge invariance: the standard model simply postulates that neutrinos are massless. This is a minimal assumption, which derives from the fact that we simply don't know the scale responsible for neutrino mass, nor the underlying mechanism.

They were dynamically coupled to radiation down to a temperature $T_{\nu,dg} \sim 900 \text{ keV}$. If their mass $m \ll T_{\nu,dg}$, their number density, at any later time, is $n_\nu = (3\zeta(3)/4\pi^2)g_\nu T_\nu^3$ (after electron annihilation $T_\nu = T_{\nu,dg}[a_{\nu,dg}/a(t)] = (4/11)^{1/3}T$) and their momentum distribution (normalized to unity) reads

$$\Phi_\nu(p, t) = \frac{2}{3\zeta(3)} \frac{(p^2/T_\nu^3)}{\exp[p/T_\nu(t)] + 1} \quad (1.38)$$

also when $p \ll m$. Hence, when $T \ll m$, their distribution is not *thermal*, although its shape was originated in thermal equilibrium. Notice that, for high p , Φ_ν is cut off as $\exp(-p/T_\nu)$.

In order to parametrize the models, we define $d = z_{eq}/z_{der}$; here we defined $z_{eq} \equiv 10^4$ (this would be the redshift when the photon density reaches the baryon+DM density, if all DM is CDM and $\theta = 1$). The derelativization redshift z_{der} , instead, occurs when the average particle momentum $\langle p \rangle = m$ (particle mass).

Using the distribution (1.38) we can evaluate

$$\langle p \rangle = (7\pi^4/180\zeta(3))T_\nu = 3.152 T_\nu. \quad (1.39)$$

Accordingly, $\langle p \rangle = m$ when $T_\nu = 0.317 m$ and, for massive ν 's,

$$d = 5.2972 \cdot 4h^2/(m/\text{eV}), \quad (1.40)$$

while

$$\Omega_h = 2.1437 \cdot 10^{-2} g_\nu (m/\text{eV}) \theta^3 / 4h^2 \quad (1.41)$$

Many experiments are dedicated to the detection of neutrino masses, here we report the most stringent upper limits found:

$$m_{\nu_e} \leq 5 \text{ eV} \quad m_{\nu_\mu} \leq 170 \text{ keV} \quad m_{\nu_\tau} \leq 18 \text{ MeV}$$

where the limit on ν_e comes from the tritium beta decay [37], on ν_τ from PSI (90% .C.L.) [70], and on ν_τ from high energy LEP experiments (a more conservative

limit is given by [71] as $m_{\nu_\tau} \leq 24 \text{ MeV}$ at 95% C.L.). As mentioned in the previous section, the most stringent limit on neutrino masses with mass lower than $\sim 1 \text{ MeV}$ has a cosmological motivation. However such limit holds only if neutrinos are stable on cosmological time scales. In models with spontaneous violation of total lepton number neutrinos can decay into a lighter neutrino plus a majoron, or a photon. When decay lifetimes are evaluated, it is found that there are many ways to make the neutrinos sufficiently short-lived so that all mass values consistent with laboratory experiments are cosmologically acceptable for the Ω_0 limit.

Stronger limits on neutrino lifetimes arise from cosmological nucleosynthesis. If a massive ν_τ is stable on the nucleosynthesis time scale (i.e. ν_τ lifetime longer than $\sim 100 \text{ sec}$), it can lead to an excessive amount of primordial helium due to its large contribution to the total energy density. This bound can be expressed through an effective number of massless neutrino species N_ν . If $N_\nu \leq 3.4 - 3.6$, ν_τ masses above 0.5 MeV can be ruled out. However, this limit is substantially weakened if, for example, a high (but still reasonable) value of the coupling constant g between tau neutrino and the majoron is considered.

Astrophysics can constrain neutrino parameters as well, by supernova (SN) theory and observations, SN dynamics and nucleosynthesis. The absence of photons arriving in conjunction with the neutrinos from SN1987A implies that the radiative lifetime of a ν_τ with mass between 100 eV and 1 MeV must be $\tau \geq 2.5 \times 10^7 \text{ sec}$ [72], observation of the energy spectrum of the SN1987A $\bar{\nu}_e$'s may be used to provide very stringent constraints on the parameters characterizing resonant neutrino conversions that could take place in the dense SN medium. SN1987A also allows to put constraints on massless neutrino mixing, while there is no way of constraining it in laboratory, since no vacuum neutrino oscillations are possible.

1.6.3 Volatile particles

By volatile particles we mean particles that originate in the decay of a heavy particle X .

Let $N_{X,dg}$ be the comoving number density of X 's at their decoupling, taking place at some early time t_{dg} , well after they became non-relativistic, and let m_X be their mass. At $t \gg t_{dg}$ their comoving number density reads:

$$N_X(t) = N_{X,dg} \exp[-(t - t_{dg})/\tau_{dy}] \quad (1.42)$$

with $t_{dg} \ll \tau_{dy}$ (decay time). We shall assume a two-body decay process, as is more likely for dynamical reasons:

$$X \rightarrow \nu + \phi \quad (1.43)$$

The decay gives rise to a light (*volatile*) particle v , of mass $m \ll m_X$, and to a massless particle ϕ . It can be either a photon (γ) or a sterile scalar, as is expected to exist in theories where a global invariance is broken below a suitable energy scale (examples of such particles are *familons* and *majorons*). Although both cases are treated in this thesis, we shall show that the latter case (sterile scalar) is potentially more significant. Particle models leading to such DM component were discussed in several papers, in some of them the volatile particle is a SUSY particle ([73],[74]) while in others it may be a neutrino [75]. In [73] for example, the volatile particle is the axino, the fermionic partner of the axion. The axino can be produced by the (radiative) decay of a neutralino, provided that a certain number of conditions are satisfied. The theoretical framework is a SUSY extension of the standard model where a Peccei–Quinn symmetry is introduced in order to solve the strong CP problem. In order to obtain a hot component as a product of the decay process, such framework needs to be restricted in the following way: (a) the lightest neutralino must be an (almost) pure gaugino; (b) the SUSY soft breaking scale is $O(\text{TeV})$; (c) The Peccei–Quinn scale should be around 10^{10} GeV. In such a framework, requiring that the ratio of the neutralino and axino masses is at least 10^5 , the axino behave like hot dark matter if the decay occurs at redshifts $z_{dy} \gtrsim 10^9$. In this scenario, aside of non-thermal axinos, it is possible to have thermal axinos decoupling when the temperature was slightly below the Peccei–Quinn scale. The thermal axinos would behave like cold dark matter, so that all the dark matter content would be accounted for with only one kind of particle. The cosmological consequences of such a scenario are described in refs. [76, 77].

A similar scenario is presented in [74]. Here, in the context of a gauge-mediated SUSY breaking, the dark matter candidate is the gravitino, that again can account for all the dark matter content. In fact, two populations of gravitinos can be present: a thermal population and an non-thermal one, the latter coming from the radiative decay of a biino. Also here the decay would take place at high redshifts ($z_{dy} \simeq 10^8$) and the non-thermally distributed gravitino would behave like hot dark matter, since it would become non-relativistic at a redshift $z_{nr} \simeq 6 \times 10^4$. However, differently from the case presented above, the thermally-distributed component would become non-relativistic at $z_{nr} \simeq 4 \times 10^6$, therefore behaving more like warm dark matter than like cold dark matter.

Once the decay process is over, the volatile momentum distribution reads:

$$\Phi_v(p, t) = 2(Q/p) \exp(-Q) \quad \text{where} \quad Q = p^2/\bar{p}^2 \quad (1.44)$$

and

$$\tilde{p} = (m_X/2)[a_{dy}/a(t)] \quad (1.45)$$

provided that X 's, before they decay, never attain a density exceeding relativistic components. This is avoided if the condition

$$\Omega_h d \ll [1 + 2/(1 + g_\nu/8.8)]^{-1} \quad \text{for } \gamma \text{ decay} \quad (1.46)$$

is fulfilled. We assume here the same definition of z_{der} and d given in the previous paragraph. This choice is taken for the sake of comparison between volatile and neutrino hot dark matter. Here g_ν refers to massless ν 's; *e.g.*, for $g_\nu = 6$, eq. (3.11) yields $\Omega_h d < 0.46$. If matter dominance occurs, the distribution (1.44) is distorted at small p , *i.e.* for particles originating in early decays. In this case the distribution can still be evaluated numerically, but no simple analytical expression can be given. Particles with large p , instead, were born in decays occurring when radiation dominance was recovered and, therefore, the distribution is however cut off as $\exp(-p^2/\tilde{p}^2)$. The cut-off is therefore sharper than in the neutrino case.

Using the distribution (1.44), it is easy to see that the average

$$\langle p \rangle = (\sqrt{\pi}/4)m_X a_{dy}/a(t) = \tilde{p}\sqrt{\pi}/2, \quad (1.47)$$

according to eq. (1.45). v 's will therefore become non relativistic when $\tilde{p} = 2m/\sqrt{\pi}$ ³; henceforth

$$\tilde{p} = (2md/\sqrt{\pi})(z/10^4). \quad (1.48)$$

Eq. (1.48) can be conveniently used in the distribution (1.44), instead of eq. (1.45), as involves model parameters (m and d), instead of early particle features (m_X and τ_{dy}), which should be further elaborated in order to work out $a_{dy} = a(\tau_{dy})$.

Let us now discuss the decay patterns in more detail. First of all, if $\phi \equiv \gamma$, the decay should occur at a redshift $z \gtrsim 10^7$, so to avoid distortions of CBR spectrum [78]. Two further possibilities should then be considered.

If the decay takes place before big-bang nucleosynthesis, the energy density of v 's is limited by the requirement that BBN yields are consistent with observed nuclide abundances; henceforth the number of relativistic spin states $g_\nu \lesssim 7$ [79]. Therefore, the actual limit on the energy density of v 's depends on the number of relativistic ν 's at BBN. If some ν has a mass exceeding ~ 1 MeV (particle data surely allow it for ν_τ) and decays before decoupling, v 's can occupy its place during BBN. As far as

³In the following chapter a different notation for the derelativization redshift may be used, in correspondence to volatile radiative decay. We therefore introduce here z_{nr} , the redshift at which $\tilde{p} = m$. Accordingly, the following relation holds: $z_{nr} = \sqrt{\pi}/2 z_{der}$.

cosmology is concerned, differences between such volatile DM and ordinary hot DM would arise from the following 3 kinematic reasons: (i) the different phase-space distribution of v 's in respect to massive ν 's; (ii) the different energy dependence of fluctuation amplitudes; (iii) the allowed continuous range of HDM derelativization redshift; in the neutrino case, for a given HDM density, the derelativization redshifts are "quantized" by the discreteness of g_ν .

By evaluating the transfer function for volatile models, we shall see that the points (i) and (ii) have a modest impact. Consequences of (iii) would be important only if other cosmological parameters, like Ω_b and h , were very well known. Altogether, therefore, the main differences induced by the above 3 points concern particle aspects. For example, v 's number density can be significantly smaller than ν 's and their masses can be much greater. In spite of that, their density and derelativization redshift z_{der} can be equal and LSS effects are quite similar.

Let then still be $\phi \equiv \gamma$, but let us assume that the decay occurs after BBN; also in this case, there are constraints related to BBN. In fact, decays produce an equal amount of v 's and γ 's. The present CBR temperature normalizes γ abundance after the thermalization of decay photons. Accordingly, a large v density implies a small γ and massless ν density *before* the decay. BBN would therefore take place almost at the *usual* temperature, but earlier in time. Neutron decay would be therefore allowed a smaller time to work and neutron abundance, at the opening of the so-called *Deuterium Bottleneck*, would be greater. From this qualitative framework quantitative limits to the final v abundance allowed by BBN can be derived. We shall not further detail this point here and will only consider a softer limit, ensuing from the obvious requirement that the final v density shall be smaller than γ density, as the latter one has a "contribution" from "primeval" γ 's. For a model with given Ω_h and d , at redshifts $z \gg z_{der}$, the following relation holds:

$$\rho_h/\rho_\gamma = \Omega_h d \quad . \quad (1.49)$$

Therefore, in this case, it must be

$$\Omega_h d \ll 1 \quad (\gamma \text{ decay}) \quad (1.50)$$

Therefore, according to eq.(1.46), this case never implies primeval temporary matter-dominated expansion, at $t < \tau_{dy}$. It should be also outlined that these models can have quite a low massless neutrino density, as X decay increases γ temperature, but does not act on ν background. It can be shown that

$$T_\nu/T_\gamma = (4/11)^{1/3}(1 - \Omega_h d) \quad (\gamma \text{ decay}) \quad (1.51)$$

and a relevant variation of the massless sterile component (SMLC hereafter) can have a significant impact on the transfer function (see next Chapter).

On the contrary, if ϕ 's are sterile scalars and the decay takes place well after BBN, constraints are not so stringent. ϕ 's will behave just as massless ν 's and these models can be characterized by a high SMLC density, which can also have a major impact in shaping the present LSS.

Therefore, significant constraints on the models can arise from this effect, which, however, cannot be discriminated *a priori*. Let us recall that, in the absence of X decay, the ratio $\rho_\nu/\rho_\gamma = 0.68132(g_\nu/6) \equiv w_o$. X decay modifies it, turning g_ν into an effective value

$$g_{\nu,eff} = g_\nu + (16/7)(11/4)^{4/3}\Omega_h d. \quad (1.52)$$

In this case, no matter dominance occurs before τ_{dy} if

$$\Omega_h d < (1 + w_o)/2 \quad (\text{for sterile decay}) \quad (1.53)$$

and ϕ 's contribution to the relativistic component lowers the *equivalence* redshift. When when $d(1 - \Omega_h) > 1 + w_o$, also ν 's are still relativistic at equivalence. Accordingly, the equivalence occurs at either

$$\bar{z}_{eq} = \frac{4h^2}{\theta^4} \frac{10^4}{1 + w_o + \Omega_h d} \quad \text{or} \quad \bar{z}_{eq} = \frac{4h^2}{\theta^4} \frac{10^4(1 - \Omega_h)}{1 + w_o + 2\Omega_h d} \quad (1.54)$$

in the former and latter case, respectively.

Mixed models involving a large volatile fraction, with late derelativization, are therefore allowed only within this scenario. In what follows we shall systematically analyze a large deal of mixed models, also with large Ω_h and d , consistent with this last picture, but we shall find that viable models with $\Omega_h d > 1$ are not so frequent.

2 Anisotropies: Linear theory

2.1 Introduction

In this Chapter we will develop the analytic treatment for the evolution of density perturbations for baryons, photons neutrinos and different kinds of dark matter. Cold, hot and warm dark matter are classified with respect to the behaviour of the particles when a specific comoving scale enters the horizon, but a common general treatment is possible, once the phase-space distribution function of the particles is specified. For a review on fluctuation evolution in linear theory with adiabatic initial conditions see also ref.[80], and for a more complete treatment ref.[81, 82]. In this Chapter we will restrict the analysis to flat Universes with no cosmological constant. Only scalar modes of fluctuations with adiabatic initial conditions will be treated.

Extensive calculations will be performed for volatile models only, while for gravitinos (WDM) models we will only report final results.

2.2 The metric and Einstein equations

In presence of density fluctuations, the metric of space-time is modified. We will perform the calculations in the synchronous gauge where fluctuations in the metric can be expressed by:

$$g^{00} = 1, \quad g_{0i} = 0, \quad g_{ik} = -a^2[\delta_{ik} - h_{ik}(x, t)] \quad (i = 1, \dots, 3) . \quad (2.1)$$

We will consider small perturbations only, so that $|h_{ik}| \ll 1$.

In Chapter 1 we showed how to deduce Friedmann equation, which give the time dependence of the scale factor $a(t)$ from the energy-momentum tensor $T_{\alpha\beta}$ ($\alpha, \beta = 0, \dots, 3$), from Einstein equation of order zero. At the next order, assuming to have small density fluctuations which only depends upon the spatial coordinate

$z = x_3$ (and therefore small gravitational fields), the following relations hold :

$$\frac{1}{2}\ddot{h} + \frac{\dot{a}}{a}\dot{h} = \frac{4\pi G}{c^2}\Delta(2T_{oo} - T) \quad (2.2)$$

$$\frac{1}{2}\frac{\partial}{\partial x^3}\left(\dot{h} - \dot{h}_{33}\right) = \frac{8\pi G}{c^3}T_{03} \quad (2.3)$$

where $\Delta(2T_{oo} - T)$ is the difference between $2T_{oo} - T$ in presence of the density perturbation, and the same quantity for the homogeneous and isotropic background (see e.g. [83]). The T_{03} , instead, is null in the homogeneous limit.

Note that the restriction on the shape of the fluctuations isn't a limitation of the study of the relevant physical cases.

The expressions $\Delta(2T_{oo} - T)$ e T_{03} are among the elements that characterize a specific model. In general, these expressions are evaluated by an integral on the phase-space distribution. These integrations can be performed before the study of the fluctuation evolution only when the gravitational effects of the particles don't depend upon their individual four-momentum. This is the case of a source which is a fluid, or also a distribution of massless particles, or on the contrary, completely non-relativistic. For massive particles, which may become non-relativistic during the evolution of the fluctuation when cosmologically relevant scales enter the horizon, the different momenta can contribute in a different way to the metric fluctuation. The standard process consists in following the evolution of the fluctuations for a sufficient number of momentum values suitably chosen, and then finding an appropriate integration method to recover the overall perturbation from the computed fluctuations. This procedure allows us to transform a set of integral-differential equations in a set of pure differential ones. The number and the values of the momenta chosen, as well as the integration method, depends upon the phase-space distribution function, and the level of accuracy desired in the computation.

2.2.1 Gauge choice

The synchronous gauge is normally used in order to carry out calculations, but results in the literature are often presented with respect to fluctuations in the conformal Newtonian gauge. In the conformal Newtonian gauge, the time is measured by

$$\tau = \int_0^t \frac{dt'}{a} \quad (2.4)$$

and the line element is given by

$$ds^2 = a^2(\tau) \left[-(1 + 2\psi)d\tau^2 + (1 - 2\phi)dx^i dx_i \right]. \quad (2.5)$$

The relation between $\psi - \phi$ and h_{ij} are reported in ref. [80]. The advantage to use the conformal Newtonian gauge is mainly that the metric tensor $g_{\alpha\beta}$ is diagonal, and analytic calculation are simpler. Moreover, in the Newtonian limit ψ plays the role of gravitational potential, and therefore has a simple physical interpretation. The potentials ϕ and ψ can be easily related to the gauge-invariant variables introduced by [81]. No gauge modes are present, since all degrees of freedom are fixed a flat Universe. Despite all the mentioned advantages, calculations have always been performed in the synchronous gauge, because in an expanding background it is always mathematically well behaved with no spurious coordinate singularities.

2.3 Unperturbed distribution of Volatile Dark Matter

In this paragraph we compute the unperturbed spectral distribution of volatile particles, i.e. particles that become from the decay of a heavier particle χ assumed at rest.

We assume a two body decay:

$$\chi \rightarrow v + \phi \quad (2.6)$$

where ϕ can be a photon or a neutral scalar (SMLC).

In the reference frame of χ the following relation holds:

$$m_\chi c^2 = \sqrt{P_v^2 c^2 + m_v^2 c^4} + P_\phi c \quad (2.7)$$

where P_v and P_ϕ are the modulus of the volatile particle and of the SMLC, respectively.

Eq.(2.7) traduces the energy conservation during the decay process. Moreover, since $P_v = P_\phi$ (momentum conservation), the following relation holds:

$$P_v = \frac{1}{2} m_\chi c \left(1 - \frac{m_v^2}{m_\chi^2}\right) \simeq \frac{1}{2} m_\chi c. \quad (2.8)$$

Let us consider now a volatile particle, created at a time t_p with an initial momentum $P^{(in)} \simeq m_\chi c/2$. The expansion of the Universe causes its momentum to decrease, so that at a generic time $t > t_p$ it will be $P = P^{(in)} a(t_p)/a(t)$. If the Universe is in the radiation-dominated epoch, this is equivalent to $P = P^{(in)} (t_p/t)^{1/2}$.

Let N_v be the comoving number density of volatile particles v ; then the fraction of volatile particles with momentum between P and $P + dP$ will be:

$$\phi(P) = \frac{1}{N_v} \frac{dN_v}{dP}. \quad (2.9)$$

Moreover, if N_χ is the comoving number density of χ 's, it will be:

$$\frac{dN_v}{dP} = \frac{dN_v}{dt_p} \frac{dt_p}{dP} = 2 \frac{t_p}{P} \left(- \frac{dN_\chi}{dt} \Big|_{t=t_p} \right) \quad (2.10)$$

and, for $t > t_{dg}$ (t_{dg} being the decoupling time of χ)

$$N_\chi(t) = N_{dg} \exp \left(- \frac{(t - t_{dg})}{t_{Dy}} \right) \equiv \alpha N_{dg} \exp \left(- \frac{t}{t_{Dy}} \right). \quad (2.11)$$

In these relations t_{Dy} is the decay time of the χ particle and N_{dg} is the comoving density of χ at a time t_{dg} . The spectral distribution function of v for $P < P^{(in)}$ can then be expressed as:

$$\phi(P) = \alpha \frac{N_{dg}}{N_v} \frac{t_p}{t_{Dy}} \frac{2}{P} \exp \left(- \frac{t_p}{t_{Dy}} \right) \quad (2.12)$$

per $P < P^{(in)}$. If we define $Q = t_p/t_{Dy}$, then the distribution in eq.(2.12) reads:

$$\phi(P) = 2\alpha \frac{N_{dg}}{N_v} \frac{Q}{P} e^{-Q}. \quad (2.13)$$

It is possible to relate the dimensionless quantity Q with the momentum P , in fact $t/t_{Dy} = (a/a_{Dy})^2 e t_p/t = (P/P^{(in)})^2$; and therefore:

$$Q = \frac{t_p}{t_{Dy}} = \left(\frac{a}{a_{Dy}} \frac{P}{P^{(in)}} \right)^2. \quad (2.14)$$

Once $\phi(P)$ is known, the unperturbed distribution function of the volatile particles ($f_v^{(o)}$) can be easily computed. It reads:

$$\frac{1}{h^3} P^2 dP \int d\Omega f_v^{(o)} = n_v \phi(P) dP \quad (2.15)$$

where n_v is the number density (non-comoving) of the volatile particles, so that $n_v a^3 = N_v$. Since $f_v^{(o)}$ is isotropic, we can compute:

$$f_v^{(o)} = \frac{h^3}{4\pi} \frac{2\alpha N_{dg}}{(aP)^3} Q e^{-Q} \theta(P^{(in)} - P) \quad (2.16)$$

where $\theta(z)(= 1 \text{ for } z > 0, = 0 \text{ for } z < 0)$ is the Heaviside function.

By means of the above expressions for $f_v^{(o)}$ and of Liouville equation, one can compute the source term for the volatile particle in the non-perturbed case. Since $f_v^{(o)}$ only depends upon t and P , Liouville equation $S_v^{(o)} = df_v^{(o)}/dt$ reads:

$$S_v^{(o)} = \frac{\partial f_v^{(o)}}{\partial t} + \frac{\partial P}{\partial t} \frac{\partial f_v^{(o)}}{\partial P} \quad (2.17)$$

or equivalently, considering that $P \propto a^{-1}$,

$$S_v^{(o)} = \frac{\dot{a}}{a} \left(a \frac{\partial f_v^{(o)}}{\partial a} - P \frac{\partial f_v^{(o)}}{\partial P} \right). \quad (2.18)$$

However $f_v^{(o)}(a) \propto a^{-3} Q e^{-Q}$ and $Q \propto a^2$, and therefore

$$\frac{\partial f_v^{(o)}}{\partial a} = -\frac{1}{a} f_v^{(o)} (1 + 2Q). \quad (2.19)$$

In a similar way, considering that $f_v^{(o)}(P) \propto P^{-3} Q e^{-Q} \theta(P^{(in)} - P)$ with $Q \propto P^2$ we obtain:

$$\frac{\partial f_v^{(o)}}{\partial P} = -\frac{1}{P} f_v^{(o)} (1 + 2Q) - f_\theta \delta(P^{(in)} - P) \quad (2.20)$$

where $f_\theta \theta = f_v^{(o)}$ and $\delta(P^{(in)} - P)$ is the Dirac distribution function. By substituting eq.(2.19) and eq.(2.20) into eq.(2.18) we find:

$$S_v^{(o)} = \frac{\dot{a}}{a} P f_\theta \delta(P^{(in)} - P). \quad (2.21)$$

During the radiation dominated epoch $\dot{a}/a = 1/2t$, while the $\delta(P^{(in)} - P)$ constrains $t = t_p$. Therefore we have:

$$\begin{aligned} S_v^{(o)}(P, t) &= \frac{h^3}{4\pi} \alpha \frac{N_{dg}}{a^3} \frac{Q e^{-Q}}{(P^{(in)})^2 t_p} \delta(P^{(in)} - P) \\ &= \frac{h^3}{4\pi} \alpha \frac{N_{dg}}{a^3} \frac{e^{-\frac{t_p}{t D_y}}}{(P^{(in)})^2 t_{D_y}} \delta(P^{(in)} - P). \end{aligned} \quad (2.22)$$

This source term goes into the perturbed equation that we shall soon consider.

2.4 Perturbed distribution function for Volatile particles

Let us consider now a distribution of v which differs from the homogeneous and isotropic one for a small perturbation, and let the latter depend on the spatial coordinates x_i only. Let then be $P_i = n_i P$ the three components of momentum. If we define $\tilde{\epsilon} = \frac{\Delta f_v}{f_v^{(o)}}$, then the perturbed distribution reads:

$$f_v(t, P, x^i, n^i) = f_v^{(o)}(t, P) \left[1 + \tilde{\epsilon}(t, P, x^i, n^i) \right]. \quad (2.23)$$

For this distribution the Liouville equation $df_v/dt = S_v$ still holds. The difference with respect to the case treated in the previous section consists in that $\tilde{\epsilon}$ depend upon the spatial variables and upon the direction of \vec{P} .

By substituting the Liouville equation of order zero from the equation for the perturbed f_v , and keeping only terms at the first order in the fluctuations, it is possible to find a partial differential equation for $\tilde{\epsilon}$ which involves $\frac{\partial \tilde{\epsilon}}{\partial t}$, $\frac{\partial \tilde{\epsilon}}{\partial x^i}$ e $\frac{\partial \tilde{\epsilon}}{\partial \bar{P}}$.

From the partial differential equation for $\tilde{\epsilon}$ we will deduce a differential equation that only involves derivatives with respect to the time. This result can be achieved as follows: (i) performing the Fourier transform on the spatial variables, so that $\partial/\partial x_i \rightarrow ik_i$; (ii) using, instead of P , a comoving momentum $\bar{P} = P(a/\bar{a})$. \bar{a} is a reference redshift; neither \bar{P} nor \bar{a} will be involved in the final results.

Let us then consider

$$f_v(t, \bar{P}, x^i, n^i) = f_v^{(o)}(t, \bar{P})[1 + \tilde{\epsilon}(t, \bar{P}, x^i, n^i)] , \quad (2.24)$$

where

$$f_v^{(o)}(t, \bar{P}) = \frac{h^3}{4\pi} 2\alpha N_{dg} \bar{a}^3 \frac{Q}{\bar{P}^3} e^{-Q} \theta(\bar{P}^{(in)} - \bar{P}) \quad (2.25)$$

($\bar{P}^{(in)} = P^{(in)}a/\bar{a}$), we then have:

$$\frac{df_v}{dt} = \frac{\partial f_v}{\partial t} + \frac{\partial x^i}{\partial t} \frac{\partial f_v}{\partial x^i} + \frac{\partial \bar{P}}{\partial t} \frac{\partial f_v}{\partial \bar{P}} + \frac{\partial n^i}{\partial t} \frac{\partial f_v}{\partial n^i} . \quad (2.26)$$

The last term in eq.(2.26) is of the second order, because both $\frac{\partial n^i}{\partial t}$ and $\frac{\partial f_v}{\partial n^i}$ are of the first order in the fluctuations.

Moreover $\frac{\partial x^i}{\partial t} = n_i P c^2 / q a$, with $q = \sqrt{m_v^2 c^4 + P^2 c^2}$ (energy of the particle) or equivalently

$$\frac{\partial x^i}{\partial t} = \frac{\bar{P}}{\bar{q}} \frac{c^2}{a} n^i \quad (2.27)$$

where $\bar{q} = \sqrt{\frac{a}{\bar{a}} m_v^2 c^4 + \bar{P}^2 c^2}$. On the other hand, for $\frac{\partial \bar{P}}{\partial t}$ the following relation holds:

$$\frac{d\bar{P}}{dt} = P \frac{\dot{a}}{\bar{a}} + \frac{a}{\bar{a}} \frac{dP}{dt} = P \frac{\dot{a}}{\bar{a}} + \frac{a}{\bar{a}} \frac{dP}{dq} \frac{dq}{dt} . \quad (2.28)$$

Making use of the relation $\frac{dq}{dt} = -c^2 \frac{P^2}{q} \left(\frac{\dot{a}}{a} - \frac{1}{2} \dot{h}_{ik} n^i n^k \right)$ and defining $y = 2\dot{h}_{ik} n^i n^k$, we finally find

$$\frac{d\bar{P}}{dt} = \frac{1}{4} y \bar{P} . \quad (2.29)$$

We can note that $\frac{d\bar{P}}{dt}$ is of the first order in the fluctuations. Therefore, the term $\frac{d\bar{P}}{dt} \frac{\partial f_v}{\partial \bar{P}}$ will simply reduced to $\frac{d\bar{P}}{dt} \frac{\partial f_v^{(o)}}{\partial \bar{P}}$, so that $\frac{\partial \tilde{\epsilon}}{\partial \bar{P}}$ doesn't appear any more in the equations. Liouville equation then reads:

$$S_v^{(o)}(1 + \sigma_S) = (1 + \tilde{\epsilon}) \frac{\partial f_v^{(o)}}{\partial t} + f_v^{(o)} \frac{\partial \tilde{\epsilon}}{\partial t} + \frac{\bar{P}}{\bar{q}} \frac{c^2}{a} n^i f_v^{(o)} \frac{\partial \tilde{\epsilon}}{\partial x^i} + \frac{1}{4} y \bar{P} \frac{\partial f_v^{(o)}}{\partial \bar{P}} \quad (2.30)$$

where σ_S is the fluctuation of the source that is caused by an inhomogeneous χ distribution.

In eq.(2.30) partial derivatives with respect to x_i are still present. They can be eliminated by considering for $\tilde{\epsilon}$ a specific spatial shape which consists in a plane wave in the direction $z = x_3$ with wavenumber k . Any wave in the direction z can be expressed by a suitable superposition of such waves, and the restriction to waves which depend upon one coordinate only is not essential, at least in the majority of the problems. Therefore, the only relevant unit vector is $n^3 \equiv \mu$.

In particular, we will have:

$$y = (1 - \mu^2)\dot{h} - (1 - 3\mu^2)\dot{h}_{33}, \quad (2.31)$$

where h is the trace of h_{ik} . Eq.(2.30) then reads:

$$S_v^{(o)}(1 + \sigma_S) = (1 + \tilde{\epsilon})\frac{\partial f_v^{(o)}}{\partial t} + f_v^{(o)}\frac{\partial \tilde{\epsilon}}{\partial t} + i\frac{\bar{P}}{\bar{q}}\frac{kc^2}{a}f_v^{(o)}\mu\tilde{\epsilon} + \frac{1}{4}y\bar{P}\frac{\partial f_v^{(o)}}{\partial \bar{P}}. \quad (2.32)$$

We now define $\tilde{\epsilon} = \epsilon\theta(\bar{P}^{(in)} - \bar{P})$, neglecting that the average velocity of χ in the fluctuations is not zero. However, it can be shown that this velocity is relevant only at higher perturbation orders.

Assuming that volatile particles are produced in the radiation-dominated era, one can obtain:

$$\tilde{\epsilon} = \dot{\epsilon}\theta(\bar{P}^{(in)} - \bar{P}) + \epsilon\bar{P}^{(in)}\frac{\delta(\bar{P}^{(in)} - \bar{P})}{2t}. \quad (2.33)$$

Furthermore

$$\begin{aligned} \frac{\partial f_v^{(o)}}{\partial \bar{P}} &= \frac{\partial f_v^{(o)}}{\partial P}\frac{\partial P}{\partial \bar{P}} = \frac{\bar{a}}{a}\left[-\frac{1}{P}f_v^{(o)}(1 + 2Q) - f_\theta\delta(P^{(in)} - P)\right] \\ &= -\frac{1}{\bar{P}}f_v^{(o)}(1 + 2Q) - \delta(\bar{P}^{(in)} - \bar{P})f_\theta. \end{aligned} \quad (2.34)$$

By substituting the above terms in eq.(2.32) and subtracting the equation at order zero, one can obtain:

$$\tilde{\epsilon}S_v^{(o)} + f_v^{(o)}\left[\dot{\epsilon}\theta + \epsilon\delta\bar{P}^{(in)}\frac{1}{2t} + i\frac{kc^2}{a}\frac{\bar{P}}{\bar{q}}\mu\epsilon\theta - \frac{1}{4}y(1 + 2Q)\right] - \frac{1}{4}y\bar{P}f_\theta\delta = S_v^{(o)}\sigma_S. \quad (2.35)$$

However, considering also eq.(2.21), we have:

$$S_v^{(o)}(\bar{P}, t) = f_\theta\frac{\bar{P}}{2t_p}\delta(\bar{P}^{(in)} - \bar{P}), \quad (2.36)$$

so that, in the fluctuation equation, f_θ can be factorized. Dividing eq.(2.35) by f_θ , one has:

$$\epsilon \theta \frac{\bar{P}^{(in)}}{2t_p} \delta + \theta \left[\dot{\epsilon} \theta + \epsilon \delta \frac{\bar{P}^{(in)}}{2t_p} + i \frac{kc^2}{a} \frac{\bar{P}}{\bar{q}} \mu \epsilon \theta \right] - \frac{1}{4} y [(1 + 2Q)\theta + \bar{P}\delta] = \frac{\bar{P}^{(in)}}{2t_p} \delta \sigma_S. \quad (2.37)$$

In the following we will separate terms that contain θ from terms that contain the Dirac distribution δ . In order to do so, let us remind that

$$g(x)\delta(x-a) = \frac{1}{2} [g(a+0) + g(a-0)] \delta(x-a) \quad (2.38)$$

where $g(a+0)$ and $g(a-0)$ stand for the limit for x which tends to a from the right and from the left respectively.

After some algebra, one can easily find:

$$\theta \left[\dot{\epsilon} + i \frac{kc^2}{a} \frac{\bar{P}}{\bar{q}} \mu \epsilon - \frac{1}{4} y (1 + 2Q) \right] + \delta \left[-\frac{1}{4} \bar{P} y - \sigma_S \frac{\bar{P}^{(in)}}{2t_p} + \epsilon \frac{\bar{P}^{(in)}}{2t_p} \right] = 0. \quad (2.39)$$

Eq.(2.39) must be verified for each \bar{P} , and therefore the following relations must be satisfied:

if $\bar{P} < \bar{P}^{(in)}$:

$$\dot{\epsilon} + i \frac{kc^2}{a} \frac{\bar{P}}{\bar{q}} \mu \epsilon = \frac{1}{4} y (1 + 2Q), \quad (2.40)$$

if $\bar{P} = \bar{P}^{(in)}$:

$$\epsilon = \sigma_S + \frac{1}{2} y t_p. \quad (2.41)$$

Since $\bar{P}^{(in)}(t) = \bar{P}$ if and only if $t = t_p$, the condition (2.41) is verified for any \bar{P} , provided that for each \bar{P} it is evaluated when $t = t_p$.

Let us now consider the expansion

$$\epsilon(k, t, \bar{P}, \mu) = \sum_{l=0}^{\infty} (-i)^l \sigma_l(k, t, \bar{P}) P_l(\mu) \quad (2.42)$$

and substitute it in eq.(2.40). This particular expansion has been chosen because the term $(-i)^l$ allows to solve eq.(2.39) in the real domain.

A similar choice will be performed for the expansion of the radiation fluctuation.

For Legendre polynomials, the following formula holds:

$$\mu P_l = \frac{l}{2l+1} P_{l-1} + \frac{l+1}{2l+1} P_{l+1} \quad (l = 1, 2, \dots); \quad \mu P_0 = P_1$$

and therefore:

$$\mu \epsilon = \sigma_0 \mu P_0 + \sum_{l=1}^{\infty} (-i)^l \sigma_l \left[\frac{l}{2l+1} P_{l-1} + \frac{l+1}{2l+1} P_{l+1} \right] \quad (2.43)$$

or equivalently:

$$\mu\epsilon = \sigma_0 P_1 - i\frac{1}{3}\sigma_1 P_0 - \frac{2}{5}\sigma_2 P_1 + \sum_{l=2}^{\infty} (-i)^{l-1} \left[\frac{l}{2l-1}\sigma_{l-1} P_l - \frac{l+1}{2l+3}\sigma_{l+1} P_l \right] \quad (2.44)$$

while it is trivial to deduce from eq.(2.42):

$$\dot{\epsilon}(k, t, \bar{P}, \mu) = \sum_{l=0}^{\infty} (-i)^l \dot{\sigma}_l(k, t, \bar{P}) P_l(\mu) \quad (2.45)$$

In the end, let us recall that $P_0 = 1$, $P_2 = \frac{1}{2}(3\mu^2 - 1)$ and, considering also eq.(2.31) one can find:

$$\frac{1}{4}y = \frac{1}{2} \left[\frac{1}{3}\dot{h}P_0 + (\dot{h}_{33} - \frac{1}{3}\dot{h})P_2 \right] \quad (2.46)$$

Substituting eqns.(2.44), (2.45) and (2.46) in eqns. (2.40) (2.41) we shall obtain:

$$\begin{aligned} & \sum_{l=0}^{\infty} (-i)^l \dot{\sigma}_l P_l + \frac{\bar{P}}{\bar{q}} \frac{kc^2}{a} \times \\ & \times \left[\frac{1}{3}\sigma_1 P_0 + i(\sigma_0 - \frac{2}{5}\sigma_2)P_1 - \sum_{l=2}^{\infty} (-i)^l \left(\frac{l}{2l-1}\sigma_{l-1} - \frac{l+1}{2l+3}\sigma_{l+1} \right) P_l \right] = \\ & = \frac{1}{2} \left[\frac{1}{3}\dot{h}P_0 + (\dot{h}_{33} - \frac{1}{3}\dot{h})P_2 \right] (1 + 2Q) \end{aligned} \quad (2.47)$$

which is valid for $\bar{P} < \bar{P}^{(in)}$, and:

$$\sum_{l=0}^{\infty} (-i)^l \sigma_l P_l = \sigma_S + t_p \left[\frac{1}{3}\dot{h}P_0 + (\dot{h}_{33} - \frac{1}{3}\dot{h})P_2 \right]$$

which is valid in the case $\bar{P} = \bar{P}^{(in)}$.

The differential equations for the coefficients σ_l are deducible from eq. (2.47) and they reads:

$$\begin{aligned} \dot{\sigma}_0 &= -\frac{1}{3} \frac{\bar{P}}{\bar{q}} \frac{kc^2}{a} \sigma_1 + \frac{1}{6} (1 + 2Q) \dot{h} & l = 0 \\ \dot{\sigma}_1 &= \frac{\bar{P}}{\bar{q}} \frac{kc^2}{a} \left(\sigma_0 - \frac{2}{5}\sigma_2 \right) & l = 1 \\ \dot{\sigma}_2 &= \frac{\bar{P}}{\bar{q}} \frac{kc^2}{a} \left(\frac{2}{3}\sigma_1 - \frac{3}{7}\sigma_3 \right) - \frac{1}{2} (1 + 2Q) \left(\dot{h}_{33} - \frac{1}{3}\dot{h} \right) & l = 2 \\ \dot{\sigma}_l &= \frac{\bar{P}}{\bar{q}} \frac{kc^2}{a} \left[\frac{l}{2l-1}\sigma_{l-1} - \frac{l+1}{2l+3}\sigma_{l+1} \right] & l > 2 \end{aligned}$$

The case $\bar{P} = \bar{P}^{(in)}$ described in eq.(2.4) leads to the following equations:

$$\sigma_0 = \sigma_S + \frac{1}{3} t_p \dot{h} \quad l = 0$$

$$\begin{aligned}\sigma_2 &= -t_p(\dot{h}_{33} - \frac{1}{3}\dot{h}) & l = 2 \\ \sigma_l &= 0 & l \neq 0, 2\end{aligned}$$

As long as the differential equations are concerned, it is important to note that, despite what appears at a first glance, they don't depend on the value of \bar{a} chosen as a reference. In fact, from the definition of \bar{P} and \bar{q} it follows that

$$\frac{\bar{P}}{\bar{q}} = \frac{P}{q} \quad (2.48)$$

Moreover, since Q is related to P , we can write the expression $\frac{P}{q}$ as a function of Q only. In fact:

$$\frac{Pc}{q} = \frac{P}{\sqrt{P^2 + m_v c^2}} = \frac{Q^{\frac{1}{2}}}{\sqrt{Q + \left(\frac{a}{a_{Dy}}\Gamma\right)^2}} \quad (2.49)$$

where

$$\Gamma \equiv \frac{2m_v}{m_\chi} \quad (2.50)$$

with these substitutions the momentum appears in the equations only by means of Q . The momentum of the volatile particles has been parametrized by the variable Q because the momentum of a particle generated at an instant t_p decrease with the expansion, while Q remains constant. Therefore a specific value of Q describes a family of volatile particles which was produced at a certain time. The above differential equation then become:

$$\dot{\sigma}_0 = -\frac{1}{3} \frac{kc}{a} \frac{Q^{\frac{1}{2}}}{\sqrt{Q + \left(\frac{a}{a_{Dy}}\Gamma\right)^2}} \sigma_1 + \frac{1}{6}(1 + 2Q)\dot{h} \quad (2.51)$$

$$\dot{\sigma}_1 = \frac{Q^{\frac{1}{2}}}{\sqrt{Q + \left(\frac{a}{a_{Dy}}\Gamma\right)^2}} \frac{kc}{a} \left(\sigma_0 - \frac{2}{5}\sigma_2 \right) \quad (2.52)$$

$$\dot{\sigma}_2 = \frac{Q^{\frac{1}{2}}}{\sqrt{Q + \left(\frac{a}{a_{Dy}}\Gamma\right)^2}} \frac{kc}{a} \left(\frac{2}{3}\sigma_1 - \frac{3}{7}\sigma_3 \right) - \frac{1}{2}(1 + 2Q) \left(\dot{h}_{33} - \frac{1}{3}\dot{h} \right) \quad (2.53)$$

$$\dot{\sigma}_l = \frac{Q^{\frac{1}{2}}}{\sqrt{Q + \left(\frac{a}{a_{Dy}}\Gamma\right)^2}} \frac{kc}{a} \left[\frac{l}{2l-1}\sigma_{l-1} - \frac{l+1}{2l+3}\sigma_{l+1} \right] \quad l > 2. \quad (2.54)$$

2.5 Thermally-distributed particles

In this section we present the set of equations for particles that were originally in thermal equilibrium with radiation. As far as we are concerned, this is the case for gravitinos (providing the WDM) and therefore we adopt the subscript \tilde{G} , but the similar procedure is applicable, for instance, to massive neutrinos (providing the HDM).

We therefore assume here a distribution function of the form:

$$f_{\tilde{G}} = A \left(e^{Pc/KT_{\tilde{G}}} + 1 \right)^{-1}. \quad (2.55)$$

We shall now take $\bar{a} = a_o$, so that $\bar{P} = P \frac{a}{a_o}$, and we define $\beta = KT_{\tilde{G},o}$ and $Q_{\tilde{G}} = \bar{P}c/\beta$.

Eq. (2.47) now reads:

$$\begin{aligned} & \sum_{l=0}^{\infty} (-i)^l \dot{\sigma}_l P_l + \frac{\bar{P}}{q} \frac{kc^2}{a} \times \\ & \times \left[\frac{1}{3} \sigma_1 P_0 + i \left(\sigma_0 - \frac{2}{5} \sigma_2 \right) P_1 - \right. \\ & \left. \sum_{l=2}^{\infty} (-i)^l \left(\frac{l}{2l-1} \sigma_{l-1} - \frac{l+1}{2l+3} \sigma_{l+1} \right) P_l \right] = \\ & = \frac{1}{2} \left[\frac{1}{3} \dot{h} P_0 + \left(\dot{h}_{33} - \frac{1}{3} \dot{h} \right) P_2 \right] Q_{\tilde{G}} \frac{\exp[Q_{\tilde{G}}]}{\exp[Q_{\tilde{G}}] + 1} \end{aligned} \quad (2.56)$$

and

$$\frac{Pc}{q} = \frac{Q_{\tilde{G}}}{\sqrt{Q_{\tilde{G}}^2 + \left(\frac{T_{der}}{T} \right)^2 \left(\frac{T_o}{T_{\tilde{G},o}} \right)^2}} = \frac{\tau D Q_{\tilde{G}}}{\sqrt{1 + (\tau D Q_{\tilde{G}})^2}}$$

where $KT_{der} = m_{\tilde{G}} c^2$, $D = \frac{T_{ref}}{T_{der}} \frac{T_{\tilde{G},o}}{T_o}$ and $\tau = \frac{T}{T_{ref}}$ by definition (T_{ref} is a reference temperature).

With these conventions, the evolution equations for thermal distribution read:

$$\dot{\sigma}_{0,\tilde{G}} = -\frac{1}{3} \frac{kc}{a} \frac{\tau D Q_{\tilde{G}}}{\sqrt{1 + (\tau D Q_{\tilde{G}})^2}} \sigma_{1,\tilde{G}} + \frac{1}{6} Q_{\tilde{G}} \frac{\exp[Q_{\tilde{G}}]}{\exp[Q_{\tilde{G}}] + 1} \dot{h} \quad (2.57)$$

$$\dot{\sigma}_{1,\tilde{G}} = \frac{\tau D Q_{\tilde{G}}}{\sqrt{1 + (\tau D Q_{\tilde{G}})^2}} \frac{kc}{a} \left(\sigma_{0,\tilde{G}} - \frac{2}{5} \sigma_{2,\tilde{G}} \right) \quad (2.58)$$

$$\dot{\sigma}_{2,\tilde{G}} = \frac{\tau D Q_{\tilde{G}}}{\sqrt{1 + (\tau D Q_{\tilde{G}})^2}} \frac{kc}{a} \left(\frac{2}{3} \sigma_1 - \frac{3}{7} \sigma_3 \right) - \frac{1}{2} Q_{\tilde{G}} \frac{\exp[Q_{\tilde{G}}]}{\exp[Q_{\tilde{G}}] + 1} \left(\dot{h}_{33} - \frac{1}{3} \dot{h} \right) \quad (2.59)$$

$$\dot{\sigma}_{l,\tilde{G}} = \frac{\tau D Q_{\tilde{G}}}{\sqrt{1 + (\tau D Q_{\tilde{G}})^2}} \frac{kc}{a} \left[\frac{l}{2l-1} \sigma_{l-1,\tilde{G}} - \frac{l+1}{2l+3} \sigma_{l+1,\tilde{G}} \right] \quad l > 2. \quad (2.60)$$

While studying gravitino models providing the warm dark matter, we also allowed for massive neutrino hot dark matter component. When Warm + Hot dark matter models are considered, a similar set of equations is used for neutrinos and gravitinos. The D value adopted should be set according to the species considered.

2.6 Equations for radiation massless neutrinos, cold and baryonic matter

Liuville equation is again the starting point in one wants to deduce the evolution equations of the perturbations in the radiation field. The presence of a source term here is caused by two effects: (i) Thomson scattering between baryons and photons (ii) photons eventually produced at χ decay. The latter point can be accounted for just considering a higher photon temperature, provided that the decay occurred early enough.

The perturbation in the radiation field can be expanded on the Legendre polynomials, just like we did for the volatile particles perturbation. The only difference is that now the perturbation integrated over the momentum will be expanded. Let us consider the distribution:

$$f_r(x, t, P, \mu) = f_r^{(o)}(P, t) [1 + \tilde{\epsilon}_r(x, t, P, \mu)] \quad (2.61)$$

in the case of the radiation field, it is convenient to refer to:

$$\delta \equiv \frac{\int dP P^3 \tilde{\epsilon}_r f_r^{(o)}}{\int dP P^3 f_r^{(o)}}. \quad (2.62)$$

Note that this choice is possible only because photons are massless particles. In the case of massive particles previously considered, the ratio $\frac{Pc}{q}$ indicates the relativistic behaviour of the particle: it decrease with time when the particle become non-relativistic.

Let us then expand the Fourier transform of δ :

$$\delta = \sum_{l=0}^{\infty} (-i)^l \delta_l P_l(\mu). \quad (2.63)$$

The related equations therefore are:

$$\dot{\delta}_0 = -\frac{1}{3} \frac{kc}{a} \delta_1 + \frac{2}{3} \dot{h} \quad (2.64)$$

$$\dot{\delta}_1 = -n_e \sigma_T c (\delta_1 - 4w) + \frac{kc}{a} \left(\delta_0 - \frac{2}{5} \delta_2 \right) \quad (2.65)$$

$$\dot{\delta}_2 = -\frac{9}{10} n_e \sigma_T c \delta_2 + \frac{2}{3} \dot{h} - 2\dot{h}_{33} + \frac{kc}{a} \left(\frac{2}{3} \delta_1 - \frac{3}{7} \delta_3 \right) \quad (2.66)$$

$$\dot{\delta}_l = -n_e \sigma_T c \delta_l + \frac{kc}{a} \left(\frac{l}{2l-1} \delta_{l-1} - \frac{l+1}{2l+3} \delta_{l+1} \right) \quad l > 2 \quad (2.67)$$

For massless neutrinos a very similar approach can be taken, the only difference being that they don't scatter with electrons. The final equations are therefore identical to photon's ones when $\sigma_T = 0$ is taken.

Equations for baryonic matter are:

$$\dot{\delta}_m = -\frac{kc}{a} w + \frac{1}{2} \dot{h} \quad (2.68)$$

$$\dot{w} = -\frac{\dot{a}}{a} w + \frac{1}{3} n_e \sigma_T c \frac{\rho_r}{\rho_m} (\delta_1 - 4w) \quad (2.69)$$

where δ_m is the fluctuation in the baryonic matter, n_e is the number density of electrons, σ_T is the Thompson scattering cross-section and w is the fluid velocity of matter. Note that baryons and radiation are coupled by Thompson scattering in the velocity equations. The coupling term is most relevant at high redshifts, when matter and radiation actually behave like a fluid. As the Universe expands, electron density decreases, until when recombination occurs, and the electron number decreases drastically. After recombination, photons and baryons are decoupled. The one-fluid approximation can therefore be used only until a certain time before recombination.

Cold dark matter, instead, is non-relativistic during all the evolution, and interacts only by means of the gravitational field. Its behaviour is described by the simple equation:

$$\dot{\delta}_c = \frac{1}{2} \dot{h} \quad (2.70)$$

2.7 Equations for the gravitational field

Let us consider again eqns. (2.2) and (2.3), and let us specify them for the case of volatile particles. Considering the source term, eq. (2.3) becomes:

$$\dot{h} - \dot{h}_{33} = \frac{16\pi G}{c^3} \frac{1}{ik} T_{03} \quad (2.71)$$

As long as baryons (m index) and cold dark matter (c index) are concerned, we have:

$$T_{00} = T = \rho_i (1 + \delta_i) c^2 \quad , \quad T_{03} = i a \rho_m c^2 w$$

While for radiation: (r index):

$$T = 0 \quad , \quad T_{00} = \rho_r(1 + \delta_r)c^2 \quad , \quad T_{03} = \frac{1}{3}ia\rho_rc^2\delta_{1,r}$$

Moreover, note that $\delta_r = \int_{-1}^1 d\mu \delta = \delta_0$.

Massless neutrinos (ν index) behave just like photons, and therefore:

$$T = 0 \quad , \quad T_{00} = \rho_\nu(1 + \delta_\nu)c^2 \quad , \quad T_{03} = \frac{1}{3}ia\rho_\nu c^2\delta_{1,\nu}$$

We will now give the expression for the volatile particles. The energy-momentum tensor for collisionless particles can be written as:

$$T_{\mu\nu} = \frac{1}{h^3} \int dP \frac{P^2}{q} f_v^{(o)} \int d\Omega P_\mu P_\nu c^2 \left(1 + \tilde{\epsilon} + \frac{1}{2}h - \frac{3}{2}h_{ik}n^i n^k \right) \quad ,$$

and therefore:

$$T_{00} = \frac{1}{h^3} \int dP P^2 q f_v^{(o)} \left[4\pi \int d\Omega \left(1 + \tilde{\epsilon} + \frac{1}{2}h - \frac{3}{2}h_{ik}n^i n^k \right) \right] \quad .$$

However, being that

$$\int d\Omega \left(\frac{1}{2}h - \frac{3}{2}h_{ik}n^i n^k \right) = 0 \quad , \quad (2.72)$$

since $\int d\Omega n^i n^k = \frac{4}{3}\pi\delta_{ik}$, the 00 component reads:

$$T_{00} = \frac{1}{h^3} \int dP d\Omega P^2 q f_v^{(o)} (1 + \tilde{\epsilon}) \quad (2.73)$$

T_{00} is the total energy density of the volatile particles. It shows an unperturbed part and a perturbed one:

$$T_{00} = \rho_v c^2 (1 + \delta_v) \quad (2.74)$$

where

$$\rho_v c^2 = \frac{4\pi}{h^3} \int dP P^2 q f_v^{(o)} \quad (2.75)$$

By substituting the explicit expression for $f_v^{(o)}$ we obtain:

$$\rho_v c^2 = \alpha \frac{N_{dg}}{a^3} \frac{1}{2} m_\chi c^2 \int_0^{(a/a_{Dy})^2} dQ \sqrt{\left(\frac{a_{Dy}}{a}\right)^2 Q + \Gamma^2} e^{-Q} \quad (2.76)$$

and defining

$$e_1 \equiv \int_0^{(a/a_{Dy})^2} dQ \sqrt{\left(\frac{a_{Dy}}{a}\right)^2 Q + \Gamma^2} e^{-Q} \quad , \quad (2.77)$$

we can write:

$$\rho_v c^2 = \alpha \frac{N_{dg}}{a^3} \frac{1}{2} m_\chi c^2 e_1 \quad . \quad (2.78)$$

We now compute the trace of T :

$$T = T_{\mu\nu} g^{\mu\nu} = \frac{m_v^2 c^4}{h^3} \int dP \frac{P^2}{q} f_v^{(o)} \int d\Omega (1 + \tilde{\epsilon}) \quad , \quad (2.79)$$

where the relation $P_\mu^\mu = m_v^2 c^4$ and eq. (2.72) were used.

Also in the trace of T we can distinguish a part due to the unperturbed distribution function and another part related to the perturbation. Therefore the contribution of volatile particles to $\Delta(2T_{00} - T)$ is:

$$\Delta(2T_{00} - T)_v = \frac{1}{h^3} \int dP P^2 \left(2q - \frac{m_v^2 c^4}{q} \right) f_v^{(o)} \int d\Omega \tilde{\epsilon} \quad (2.80)$$

Since we now have to integrate over the solid angle Ω , let us outline that if a function $g(\Omega)$ only depends upon μ , then $\int d\Omega g(\Omega) = 2\pi \int_{-1}^1 d\mu g(\mu)$. Eq. (2.80) then becomes:

$$\Delta(2T_{00} - T)_v = \frac{4\pi}{h^3} \int dP P^2 q \left(1 - \frac{m_v^2 c^4}{2q^2} \right) f_v^{(o)} \int_{-1}^1 d\mu \tilde{\epsilon} \quad (2.81)$$

If we now substitute $f_v^{(o)}$ from eq. (2.16), consider that $\int_{-1}^1 d\mu \tilde{\epsilon} = \sigma_0$ and the usual relation between P and Q , we obtain:

$$\Delta(2T_{00} - T)_v = \frac{\rho_v c^2}{e_1} e_3 \quad (2.82)$$

where e_1 is taken from eq. (2.77) and

$$e_3 \equiv \int_0^{(a/a_{Dy})^2} dQ \frac{(a_{Dy}/a)^2 Q + \frac{1}{2}\Gamma^2}{\sqrt{(\frac{a_{Dy}}{a})^2 Q + \Gamma^2}} e^{-Q} \sigma_0 \quad (2.83)$$

Now we are ready to write the expression of eq.(2.2) for our particular cosmological model. It reads:

$$\ddot{h} = -2\frac{\dot{a}}{a}\dot{h} + 8\pi G \left[\delta_m \rho_m + 2\delta_{0,r} \rho_r + 2n_\nu \delta_{0,\nu} \rho_\nu + \delta_c \rho_c + \frac{\rho_v}{e_1} e_3 \right] \quad (2.84)$$

where n_ν is the number of equivalent massless neutrinos which may also include the effect of the sterile scalar ($n_\nu = g_{\nu,eff}/2$).

If we want to give an explicit form for eq. (2.71) it is necessary to compute the component T_{03} for the volatile particles. We recover eq. (2.7) to this aim, reminding

that $P_0 = P^0$, and $P_i = -Paen^i$ with $e = 1 - \frac{1}{2}h_{ik}n^in^k$. Keeping only terms at the first order in the fluctuations, and using eq. (2.72) again, we find:

$$\begin{aligned} T_{03} &= -a \frac{1}{h^3} \int dP P^3 f_v^{(o)} c \int d\Omega \mu (1 + \tilde{\epsilon}) \\ &= -a \frac{4\pi}{h^3} \int dP P^3 f_v^{(o)} \left(\frac{1}{2} \int_{-1}^1 d\mu \mu (1 + \tilde{\epsilon}) \right) \end{aligned} \quad (2.85)$$

If we now substitute the expression for $f_v^{(o)}$, we have:

$$T_{03} = -\frac{1}{2} a_{Dy} \frac{\rho_v c^2}{e_1} \int_0^{(a/a_{Dy})^2} dQ Q^{\frac{1}{2}} e^{-Q} \int_{-1}^1 d\mu \mu \tilde{\epsilon} \quad (2.86)$$

If we recall that $\frac{3}{2} \int_{-1}^1 d\mu \mu \tilde{\epsilon} = -i\sigma_1$, we find:

$$T_{03} = i \frac{1}{3} a_{Dy} \frac{\rho_v c^2}{e_1} \int_0^{(a/a_{Dy})^2} dQ Q^{\frac{1}{2}} e^{-Q} \sigma_1 \quad (2.87)$$

By defining

$$e_4 \equiv \int_0^{(a/a_{Dy})^2} dQ Q^{\frac{1}{2}} e^{-Q} \sigma_1 \quad (2.88)$$

and keeping in mind the expressions of T_{03} for the other components, we have:

$$\dot{h}_{33} = \dot{h} - \frac{16\pi G}{kc} a \left[\rho_m w + \frac{1}{3} \rho_r \delta_{1,r} + \frac{1}{3} n_\nu \rho_\nu \delta_{1,\nu} + \frac{1}{2} \frac{a_{Dy}}{a} \frac{\rho_v}{e_1} e_4 \right] \quad (2.89)$$

When gravitinos or massive neutrinos are considered, the same procedure can be applied.

If the distribution in eq.2.55 is considered, the relevant expressions are:

$$\rho_{\tilde{G}}^3 c^2 = C_o \frac{\tau^3}{D} e_{1,\tilde{G}} \quad (2.90)$$

where $C_o = \frac{4\pi A}{c^3 h^3} (KT_{ref})^4 \left(\frac{T_{o,\tilde{G}}}{T_o} \right)^4$ and

$$e_{1,\tilde{G}} \equiv \int_0^\infty dQ_{\tilde{G}} Q_{\tilde{G}}^2 \sqrt{\frac{1 + (\tau D Q_{\tilde{G}})^2}{\exp Q_{\tilde{G}} + 1}}. \quad (2.91)$$

Similarly,

$$\Delta(2T_{00} - T)_{\tilde{G}} = C_o \frac{\tau^3}{D} e_{3,\tilde{G}} \quad (2.92)$$

where

$$e_{3,\tilde{G}} \equiv \int_0^\infty dQ_{\tilde{G}} Q_{\tilde{G}}^2 \frac{\frac{1}{2} + (\tau D Q_{\tilde{G}})^2}{\sqrt{1 + (\tau D Q_{\tilde{G}})^2} \exp Q_{\tilde{G}} + 1} \sigma_{0,\tilde{G}} \quad (2.93)$$

and

$$T_{03,\tilde{G}} = i\frac{1}{3}\tau_o D \frac{\rho_{\tilde{G}} c^2}{e_{1,\tilde{G}}} e_{4,\tilde{G}} \quad (2.94)$$

with

$$e_{4,\tilde{G}} \equiv \int_0^\infty dQ_{\tilde{G}} Q_{\tilde{G}}^3 \frac{1}{\exp Q_{\tilde{G}} + 1} \sigma_{1,\tilde{G}}. \quad (2.95)$$

2.8 Final equations

We present here a summary of all the equations that are needed in order to study the fluctuation evolution in all the different components. Some of them are identical in any cosmological model considered, others will depend on the kind of dark matter considered.

The expansion equation is the same, provided that the appropriate energy densities are included. Equations for massless neutrinos, photons, baryons and cold dark matter are also the same:

$$\left(\frac{\dot{a}}{a}\right)^2 = \frac{8\pi G}{3} \left[\sum_{\text{all components}} \rho \right] \quad (2.96)$$

$$\dot{\delta}_m = -\frac{kc}{a}w + \frac{1}{2}\dot{h} \quad (2.97)$$

$$\dot{w} = -\frac{\dot{a}}{a}w + \frac{1}{3}n_e\sigma_T c \frac{\rho_r}{\rho_m}(\delta_{1,r} - 4w) \quad (2.98)$$

$$\dot{\delta}_c = \frac{1}{2}\dot{h} \quad (2.99)$$

$$\dot{\delta}_{0,r} = -\frac{1}{3}\frac{kc}{a}\delta_{1,r} + \frac{2}{3}\dot{h} \quad (2.100)$$

$$\dot{\delta}_{1,r} = -n_e\sigma_T c(\delta_{1,r} - 4w) + \frac{kc}{a}\left(\delta_{0,r} - \frac{2}{5}\delta_{2,r}\right) \quad (2.101)$$

$$\dot{\delta}_{2,r} = -\frac{9}{10}n_e\sigma_T c\delta_{2,r} + \frac{2}{3}\dot{h} - 2\dot{h}_{33} + \frac{kc}{a}\left(\frac{2}{3}\delta_{1,r} - \frac{3}{7}\delta_{3,r}\right) \quad (2.102)$$

$$\dot{\delta}_{l,r} = -n_e\sigma_T c\delta_{l,r} + \frac{kc}{a}\left(\frac{l}{2l-1}\delta_{l-1,r} - \frac{l+1}{2l+3}\delta_{l+1,r}\right) \quad l > 2 \quad (2.103)$$

$$\dot{\delta}_{0,\nu} = -\frac{1}{3}\frac{kc}{a}\delta_{1,\nu} + \frac{2}{3}\dot{h} \quad (2.104)$$

$$\dot{\delta}_{1,\nu} = \frac{kc}{a}\left(\delta_{0,\nu} - \frac{2}{5}\delta_{2,\nu}\right) \quad (2.105)$$

$$\dot{\delta}_{2,\nu} = \frac{2}{3}\dot{h} - 2\dot{h}_{33} + \frac{kc}{a}\left(\frac{2}{3}\delta_{1,\nu} - \frac{3}{7}\delta_{3,\nu}\right) \quad (2.106)$$

$$\dot{\delta}_{l,\nu} = \frac{kc}{a} \left(\frac{l}{2l-1} \delta_{l-1,\nu} - \frac{l+1}{2l+3} \delta_{l+1,\nu} \right) \quad l > 2 \quad (2.107)$$

When volatile dark matter is considered, we have:

$$\dot{\sigma}_0 = -\frac{1}{3} \frac{kc}{a} \frac{Q^{\frac{1}{2}}}{\sqrt{Q + \left(\frac{a}{a_{Dy}} \Gamma\right)^2}} \sigma_1 + \frac{1}{6} (1 + 2Q) \dot{h} \quad (2.108)$$

$$\dot{\sigma}_1 = \frac{Q^{\frac{1}{2}}}{\sqrt{Q + \left(\frac{a}{a_{Dy}} \Gamma\right)^2}} \frac{kc}{a} \left(\sigma_0 - \frac{2}{5} \sigma_2 \right) \quad (2.109)$$

$$\dot{\sigma}_2 = \frac{Q^{\frac{1}{2}}}{\sqrt{Q + \left(\frac{a}{a_{Dy}} \Gamma\right)^2}} \frac{kc}{a} \left(\frac{2}{3} \sigma_1 - \frac{3}{7} \sigma_3 \right) - \frac{1}{2} (1 + 2Q) \left(\dot{h}_{33} - \frac{1}{3} \dot{h} \right) \quad (2.110)$$

$$\dot{\sigma}_l = \frac{Q^{\frac{1}{2}}}{\sqrt{Q + \left(\frac{a}{a_{Dy}} \Gamma\right)^2}} \frac{kc}{a} \left[\frac{l}{2l-1} \sigma_{l-1} - \frac{l+1}{2l+3} \sigma_{l+1} \right] \quad l > 2 \quad (2.111)$$

and equations for the gravitational field yields:

$$\ddot{h} = -2 \frac{\dot{a}}{a} \dot{h} + 8\pi G \left[\delta_m \rho_m + 2\delta_{0,r} \rho_r + 2n_\nu \delta_{0,\nu} \rho_\nu + \delta_c \rho_c + \frac{\rho_\nu}{e_1} e_3 \right] \quad (2.112)$$

$$\dot{h}_{33} = \dot{h} - \frac{16\pi G}{kc} a \left[\rho_m w + \frac{1}{3} \rho_r \delta_{1,r} + \frac{1}{3} n_\nu \rho_\nu \delta_{1,\nu} + \frac{1}{2} \frac{a_{Dy}}{a} \frac{\rho_\nu}{e_1} e_4 \right] \quad (2.113)$$

while with Gravitinos (or massive neutrinos):

$$\dot{\sigma}_{0,\tilde{G}} = -\frac{1}{3} \frac{kc}{a} \frac{\tau D Q \tilde{G}}{\sqrt{1 + (\tau D Q \tilde{G})^2}} \sigma_{1,\tilde{G}} + \frac{1}{6} Q \tilde{G} \frac{\exp[Q \tilde{G}]}{\exp[Q \tilde{G}] + 1} \dot{h} \quad (2.114)$$

$$\dot{\sigma}_{1,\tilde{G}} = \frac{\tau D Q \tilde{G}}{\sqrt{1 + (\tau D Q \tilde{G})^2}} \frac{kc}{a} \left(\sigma_{0,\tilde{G}} - \frac{2}{5} \sigma_{2,\tilde{G}} \right) \quad (2.115)$$

$$\dot{\sigma}_{2,\tilde{G}} = \frac{\tau D Q \tilde{G}}{\sqrt{1 + (\tau D Q \tilde{G})^2}} \frac{kc}{a} \left(\frac{2}{3} \sigma_1 - \frac{3}{7} \sigma_3 \right) - \frac{1}{2} Q \tilde{G} \frac{\exp[Q \tilde{G}]}{\exp[Q \tilde{G}] + 1} \left(\dot{h}_{33} - \frac{1}{3} \dot{h} \right) \quad (2.116)$$

$$\dot{\sigma}_{l,\tilde{G}} = \frac{\tau D Q \tilde{G}}{\sqrt{1 + (\tau D Q \tilde{G})^2}} \frac{kc}{a} \left[\frac{l}{2l-1} \sigma_{l-1,\tilde{G}} - \frac{l+1}{2l+3} \sigma_{l+1,\tilde{G}} \right] \quad l > 2. \quad (2.117)$$

$$\ddot{h} = -2 \frac{\dot{a}}{a} \dot{h} + 8\pi G \left[\delta_m \rho_m + 2\delta_0 \rho_r + 2n_\nu \delta_{0,\nu} \rho_\nu + \delta_c \rho_c + \frac{\rho_{\tilde{G}}}{e_{1,\tilde{G}}} e_{3,\tilde{G}} \right] \quad (2.118)$$

$$\dot{h}_{33} = \dot{h} - \frac{16\pi G}{kc} a \left[\rho_m w + \frac{1}{3} \rho_r \delta_1 + \frac{1}{3} n_\nu \rho_\nu \delta_{1,\nu} + \frac{1}{2} \frac{\tau_o D}{a} \frac{\rho_{\tilde{G}}}{e_{1,\tilde{G}}} e_{4,\tilde{G}} \right] \quad (2.119)$$

When also neutrino hot dark matter is included in order to have a warm + hot dark matter model, the gravitino term should be doubled (we only considered one massive neutrino) and an appropriate D for neutrinos should be taken.

Note that the equations for the expansion parameter a , as well as for \dot{h} and \dot{h}_{33} are integral–differential equations. This comes as no surprise, since different groups of volatile particles (or gravitinos) characterized by different Q ($Q_{\tilde{G}}$) values, contribute altogether to the expansion and to metric fluctuations. The integrals that appear in the above equations are:

$$e_1 \equiv \int_0^{(a/a_{Dy})^2} dQ \sqrt{\left(\frac{a_{Dy}}{a}\right)^2 Q + \Gamma^2} e^{-Q} \quad (2.120)$$

$$e_3 \equiv \int_0^{(a/a_{Dy})^2} dQ \frac{\left(\frac{a_{Dy}}{a}\right)^2 Q + \frac{1}{2}\Gamma^2}{\sqrt{\left(\frac{a_{Dy}}{a}\right)^2 Q + \Gamma^2}} e^{-Q} \sigma_0 \quad (2.121)$$

$$e_4 \equiv \int_0^{(a/a_{Dy})^2} dQ Q^{\frac{1}{2}} e^{-Q} \sigma_1 \quad (2.122)$$

$$e_{1,\tilde{G}} \equiv \int_0^\infty dQ_{\tilde{G}} Q_{\tilde{G}}^2 \sqrt{\frac{1 + (\tau D Q_{\tilde{G}})^2}{\exp Q_{\tilde{G}} + 1}}. \quad (2.123)$$

$$e_{3,\tilde{G}} \equiv \int_0^\infty dQ_{\tilde{G}} Q_{\tilde{G}}^2 \frac{\frac{1}{2} + (\tau D Q_{\tilde{G}})^2}{\sqrt{1 + (\tau D Q_{\tilde{G}})^2}} \frac{1}{\exp Q_{\tilde{G}} + 1} \sigma_{0,\tilde{G}} \quad (2.124)$$

$$e_{4,\tilde{G}} \equiv \int_0^\infty dQ_{\tilde{G}} Q_{\tilde{G}}^3 \frac{1}{\exp Q_{\tilde{G}} + 1} \sigma_{1,\tilde{G}} \quad (2.125)$$

In the end, note that the equation for metric perturbation h is of second order. Since we are not interested in the evaluation of $h(t)$, we will consider $u(t) = \dot{h}$ as the unknown variable. \dot{h}_{33} can be treated similarly. We have for them two algebraic equations instead of two differential equations.

2.9 Initial conditions

2.9.1 Volatile dark matter

We start our computation when all cosmologically relevant scales are out of the horizon. Under this hypothesis, eqns. (2.96)–(2.113) simplify a lot, being that

$\frac{k}{a} \ll \frac{1}{ct}$ and therefore all terms with $\frac{kc}{a}$ are negligible. Besides volatile dark matter, fluctuations in all the other components are:

$$\delta_m = \frac{1}{2}h \quad \delta_c = \frac{1}{2}h \quad \delta_{0,r} = \frac{2}{3}h \quad \delta_{0,\nu} = \frac{2}{3}h \quad (2.126)$$

$$\ddot{h} = -2\frac{\dot{a}}{a}\dot{h} + 16\pi G\delta_0\rho_{tot,r} \quad (2.127)$$

where the adiabatic character of the fluctuations has been imposed in eq.(2.126) and $\rho_{tot,r}$ accounts for all relativistic species. From eqns.(2.126) we can see that δ_m , δ_c , $\delta_{0,r}$ and h are all proportional. Keeping in mind that

$$\rho_{tot,r} = \frac{3}{8\pi G} \frac{1}{4t^2} \quad , \quad (2.128)$$

then eq. (2.127) can be written as:

$$\ddot{h} + \frac{1}{t^2}\dot{h} - \frac{1}{t^2}h = 0 \quad . \quad (2.129)$$

Eq. (2.129) is verified if $h \propto t$. We take $\delta_m \equiv At$ as the reference variable. We will then have:

$$\delta_m = At \quad \delta_c = \delta_m \quad \delta_0 = \frac{4}{3}\delta_m \quad \dot{h} = 2\frac{\delta_m}{t} \quad (2.130)$$

Higher harmonics for the radiation can initially be set to zero: they acquire a value because of the hierarchical coupling of the equations. Matter velocity can be initially set to zero as well, the scattering with radiation will cause it to have values different from zero.

Let us now consider the initial conditions for volatile dark matter. For any Q value, they are given at a time $t = t_p$. Always assuming $\frac{k}{a} \ll \frac{1}{ct}$, one finds:

$$\dot{\sigma}_0 = \frac{1}{6}\dot{h}(1 + 2Q) \quad (2.131)$$

$$\dot{\sigma}_2 = -\frac{1}{2}\left(\dot{h}_{33} - \frac{1}{3}\dot{h}\right)(1 + 2Q) \quad . \quad (2.132)$$

$$\dot{\sigma}_l = 0 \quad l \neq 0, 2 \quad (2.133)$$

Since we consider to be in a radiation-dominated era, we have:

$$\dot{h}_{33} = \dot{h} - 2\frac{8\pi G}{3}\rho_{tot,r}\delta_1\frac{a}{kc} \quad (2.134)$$

while, at first perturbation order,

$$\dot{\delta}_1 = \frac{kc}{a}\delta_0 \quad . \quad (2.135)$$

Considering eq.(2.130) we will have:

$$\delta_1 = \frac{8}{9} \frac{kc}{a} \delta_m t \quad (2.136)$$

and substituting eqns. (2.128), (2.130) and (2.136) into eq.(2.135) we find:

$$\dot{h}_{33} = \frac{14}{9} \frac{\delta_m}{t} = \frac{7}{9} \dot{h} \quad (2.137)$$

We can now integrate the equations for σ_0 and σ_2 . They reads:

$$\sigma_0 = \frac{1}{3} \delta_m (1 + 2Q) + C_0 \quad (2.138)$$

$$\sigma_2 = -\frac{4}{9} \delta_m (1 + 2Q) + C_2 \quad (2.139)$$

Coefficients C_0 and C_2 can be found by imposing that the above expression for σ_0 and σ_2 must be valid at $t = t_p$. At that time, in fact, we know that:

$$\sigma_0 = \sigma_S + \frac{1}{3} t_p \dot{h} \quad (2.140)$$

$$\sigma_2 = -t_p (\dot{h}_{33} - \frac{1}{3} \dot{h}) \quad (2.141)$$

The source term σ_S is due to an inhomogeneous distribution of the χ particles, which are non-relativistic at the moment of the decay. Therefore we can consider $\sigma_S = \delta_c$ and compute:

$$C_0 = \frac{2}{3} \delta_m Q \left(\frac{a_{Dy}}{a} \right)^2 (2 - Q) \quad (2.142)$$

$$C_2 = -\frac{4}{9} \delta_m Q \left(\frac{a_{Dy}}{a} \right)^2 (1 - 2Q) \quad (2.143)$$

and finally:

$$\sigma_0 = \frac{1}{3} \delta_m \left[(1 + 2Q) + \left(\frac{a_{Dy}}{a} \right)^2 2Q(2 - Q) \right] \quad (2.144)$$

$$\sigma_2 = -\frac{4}{9} \delta_m \left[(1 + 2Q) + \left(\frac{a_{Dy}}{a} \right)^2 Q(1 - 2Q) \right] \quad (2.145)$$

These are the initial conditions for the integration of the equations (2.96)–(2.113).

2.9.2 Gravitinos

In the case of gravitinos and neutrinos, the initial conditions are:

$$\sigma_{0,\tilde{G}} = \frac{1}{3} Q_{\tilde{G}} \frac{\exp[Q_{\tilde{G}}]}{\exp[Q_{\tilde{G}}] + 1} \quad (2.146)$$

$$\dot{\sigma}_{2,\tilde{G}} = \frac{1}{4} \frac{\exp[Q_{\tilde{G}}]}{\exp[Q_{\tilde{G}}] + 1} \quad (2.147)$$

2.10 Technical issues

On the basis of the equations treated in this Chapter, we built a Boltzmann code that integrates them. Here we shall sketch some technical issues that were envisaged.

Our code integrates the set of equations for the fluctuation evolution in the synchronous gauge. We sped it up by truncating the hierarchical set of equations of free-streaming particles (photons after recombination, HDM, WDM and massless ν 's), according to the scheme suggested by Ma & Bertschinger [80], slightly modifying it because we don't use conformal time.

As far as volatile particles are concerned, we adopted the Gauss-Laguerre integration method with 10 integration points, and verified that this was enough to obtain an adequate accuracy.

Results with the truncation strategy mentioned above were compared with results with a free number of harmonics and we found that a truncation at the 8th harmonics is mostly sufficient. Results presented in the next Chapters are however obtained with truncation at the 24th harmonics. Models were evolved down to $z = 0$. We evaluated the transfer function for 24 scales ranging from $L = 20000$ Mpc to $L = 0.53054$ Mpc. Results from the public code CMBFAST, yielding the transfer function for mixed models (only with thermal hot component), were compared with the results of our algorithm, for a number of models and for scales fixed by CMBFAST.

Relative discrepancies between code outputs vary from less than 10^{-4} , on scales above ~ 100 Mpc, to slightly above 3 % in the worst cases, which occur for the hot component, when $\Omega_h > 0.3$ and for scales below 2–3 Mpc. In such cases CMBFAST tends to give a transfer function slightly smaller than our code. The typical discrepancy, however, keeps safely below 0.5 %.

Altogether the main source of error comes from the analytic fit to the transfer functions, although the top discrepancy at a single point keeps < 1 % in the worst cases and its typical value is < 0.1 %.

As long as WDM models are concerned, we find that a higher degree of accuracy is needed when dealing with WDM-dominated models if compared to the CDM-dominated ones. The reason is that all the δ_i are coupled by means of the potential; whose evolution equation, in turn, depends upon all the different overdensities, each of them contributing with a weight Ω_i . If the overdensity of the most abundant component is not well evaluated, the error propagates via the potential to all the other components, and over time. In the case of standard MDM, CDM plays this role, it stabilizes the value of the potential so that a lower accuracy in the integrals

over the momenta of the hot component is allowed.

In WDM and WHDM models, gravitinos (and massive neutrinos) are the most abundant components, and their overdensities are evaluated by mean of integrals. It is therefore necessary to choose the integration method that, at the same time, (i) provides the best accuracy, and (ii) minimizes the number of values of the momentum over which the integration is performed, so as to keep the number of differential equations to be solved as small as possible.

Within the class of Gauss integration methods [84], we verified that, keeping fixed the number of integration points in momentum space, Gauss–Legendre integration performs better than Gauss–Laguerre for a thermal distribution, especially for high values of k confirming what outlined by [85]. Furthermore, we found that using Gauss–Legendre integration, 20 integration points are adequate to obtain stable results.

3 Power Spectra

3.1 Introduction

In the previous Chapter we showed how fluctuations evolve in time. Here we are more interested in understanding how structure form, given a specific cosmological model. In order to do so, in this Chapter we introduce the power spectrum, which is the fundamental tool that allows to make predictions about the formation of cosmological structures and the microwave background anisotropies, once the underlying Friedmann background is fixed.

We will discuss the effects of different dark matter component in modelling both matter and CMB power spectra, paying particular attention to the light-gravitinos warm dark matter models and the volatile models, which constitute part of our original work. CDM models, as well as HDM and CHDM models, will be often used as a reference scenario. Most of the content presented here can be found in ref. [76, 77, 68, 86, 87].

3.2 The matter power spectrum

The matter power spectrum is defined as:

$$P(k) = \langle |\delta(k)|^2 \rangle \quad (3.1)$$

where $\delta(k)$ is the total matter fluctuation, that takes into account all the massive components in the Universe. The power spectrum has a different shape at different redshift, according to the status of fluctuation evolution up to that z . In general we are interested in the power spectrum when structure form, at very low redshifts (say $z = 0$). At this stage it is useful to describe the power spectrum as a product of an *initial* power spectrum $P_{in}(k)$, which tells us how the power spectrum was when all the cosmologically relevant scales were out of the horizon, and a *transfer*

function $T(k)$ that summarizes the effect of the evolution of density perturbations on the power spectrum:

$$P(k) = P_{in}(k)T^2(k) \quad (3.2)$$

where

$$T(k) = \frac{\sum_{i=1}^{N_s} \Omega_i \delta_{i,z=0}}{\sum_{i=1}^{N_s} \Omega_i \delta_{i,z=z_i}}, \quad (3.3)$$

here N_s is the number of different massive species in the model, δ_i is the energy overdensity of the i -th component and z_i a suitable initial redshift such that the smallest considered scale is much larger than the horizon scale at z_i . $T(k)$ is normalized to unity at scales so large that they enter the horizon after recombination. $T(k)$ conveys all the information about the evolution of a density fluctuation mode at the wavenumber k through the matter-radiation equality and recombination epochs, and therefore depends on both background quantities (like the matter and radiation content) and the substance of the dark matter. The initial power spectrum is commonly considered as a power law $P_{in}(k) = Ak^n$, as is predicted by the most common inflationary scenarios. The overall shape of the power spectrum will therefore depend on n and the shape of the transfer function $T(k)$. In the following we will describe how $T(k)$ depends upon background quantities and the matter content of the model.

Let us now present first the CDM model. The typical shape of the corresponding transfer function is plotted in fig.3.1. It is constant for low k and it decreases at high k . On very large scales, no physical effects damp the fluctuation, and the transfer function is therefore $\simeq 1$.

In a CDM models, small scales are damped due to the *Meszaros effect*. If a perturbation on a scale \tilde{k} enters the horizon at a redshift \tilde{z} while the Universe is still radiation-dominated, the fluctuation in the cold component stop growing because at that time the potential is mostly driven by radiation perturbation, and radiation perturbations are oscillating with baryons, causing no increase in the potential. After equivalence, radiation has a marginal effect in determining the potential evolution, and fluctuations in the cold component start growing again. For the period of time between the entrance of the scale \tilde{k} enters the horizon and the equivalence, the amplitude of the fluctuations on the scale \tilde{k} is frozen, while fluctuations on bigger scales (which are still out of the horizon) are still growing with $\delta(z) \propto (1+z)^{-2}$. The amplitude $\delta(\tilde{k})$ of the fluctuation on the scale \tilde{k} is therefore damped by a factor:

$$\frac{\delta(\tilde{k})}{\delta(k_{>hor})} = \left(\frac{1+z_{eq}}{1+\tilde{z}} \right)^2 = \left(\frac{k_{eq}}{\tilde{k}} \right)^2. \quad (3.4)$$

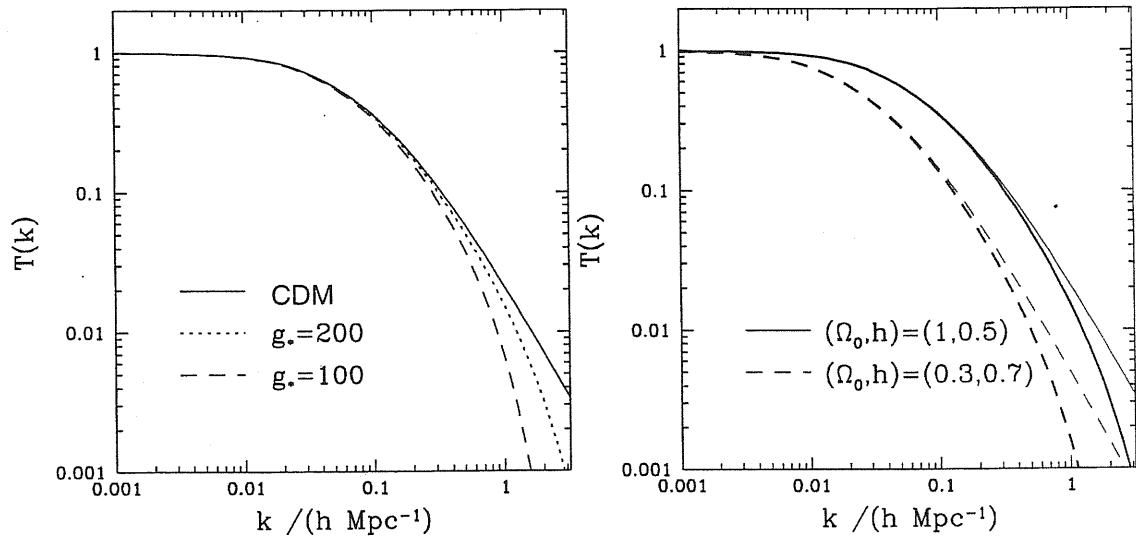


Figure 3.1: The shape of the transfer functions for WDM gravitino models. Left panel: the effect of varying g_* for $\Omega_0 = 1$ and $h = 0.5$; solid, dotted and dashed curves correspond to the CDM case, to $g_* = 200$ and $g_* = 100$, respectively. Right panel: the effect of varying the Friedmann background; heavy and light curves correspond to the CDM and WDM with $g_* = 200$ cases, respectively.

where k_{eq} is the wavenumber of a scale that enters the horizon at equivalence ($k_{eq} = 2\pi/\lambda_{eq} = 2\pi/7.57(\Omega_o h^2)^{-1}\theta^2 Mpc^{-1}$). Perturbations on scales that enter the horizon after equivalence do not suffer from Maszaros effect. We therefore note that the knee in the transfer function is related to the equivalence scale. If for any reason the radiation content is enriched or the matter content reduced, the transfer function will keep qualitatively the same shape, but it will result shifted to the left (λ_{eq} is increased and k_{eq} decreased). This is in fact what happens to the transfer function for open (low Ω_o) or low h models. To some extent, this is what happens also with volatile models. It is often useful to consider an analytic expression for $T(k)$, here we quote the expression provided by [88]:

$$T_{CDM} = \frac{\ln(1 + 2.34q)}{2.34q} \left[1 + 3.89q + (16.1q)^2 + (5.46q)^3 + (6.71q)^4 \right]^{-1/4} \quad (3.5)$$

where $q = k\theta_r^{1/2}/(\Omega_c h^2 Mpc^{-1})$, here $\theta_r = \rho_{er}/(1.68\rho_r)$ is a measure of the ratio of energy density in relativistic particles with respect to photons ($\theta_r = 1$ correspond to the standard case of photon + three massless neutrinos).

Note that the shape of the transfer function is effectively $T_{CDM}(k) \propto k^{-2}$, which implies $P_{CDM}(k) \propto k^{-3}$ for a Harrison-Zeldovich spectrum $n = 1$. However, $P_{CDM}(k)$ reaches this regime for very small scales, while even on galactic scales it is still approximately $P_{CDM}(k) \propto k^{-2}$.

In a CDM model, the Meszaros effect is all we need in order to understand the shape of the power spectrum. Let us now consider a model in which some hot dark matter is added to the cold one (CHDM models, see [89], see also [90, 91, 92, 93, 94, 95, 96, 97, 98, 99]). In this case, also other effects must be taken into account. In fact, hot dark matter particles free-stream and therefore erase the fluctuation if the latter enter the horizon while the particles are still relativistic. As shown in the previous chapter, the fluctuation in the hot component is studied for different values of the momentum, and the overall fluctuation is found by integrating over the momentum. This procedure is necessary because at a certain time some particles may be already non-relativistic, and behave like CDM particles, while others can be still relativistic, and free-stream. Given a fluctuation over a scale \tilde{k} , the higher is the fraction of relativistic particles when that scale enters the horizon, the more visible is the effect of free-streaming. Free-streaming will have two consequences: first (and most important) the fluctuation in the hot component itself will be damped and therefore its contribution to $T(k)$ will be lower than it would be in absence of free-streaming; moreover the potential over that scale will be reduced, causing a less pronounced growth of fluctuations in all the other components. Both of these effects

go in the direction of damping the transfer function on high k . However in CHDM models there is a sort of feed back effect due to the presence of the cold component. In fact, even if the hot dark matter particles are still relativistic when the scale of the fluctuation enters the horizon, they might become non-relativistic soon after. At that moment, the fluctuation in the hot component is partially damped, but if also a cold component is present, the hot dark matter particles feel the potential well of the cold component, their perturbation restart growing and its amplitude can eventually reach the amplitude of the cold one. The result of all these effect is that the transfer function in the CHDM models has less power on small scales than the CDM one, the discrepancy greatly depending on the considered amount of the hot component.

When all the dark matter is hot, then there is a significant damping in the transfer function, which can be approximately described by an exponential cutoff. Bardeen et al. [88] give an analytic expression for the transfer function in a Hot Dark Matter model, if the hot dark matter is provided by a massive neutrino:

$$T_\nu(k) = \exp[-0.16(kR_{f\nu}) - (kR_{f\nu})^2/2][1 + 1.6q + (4.0q)^{3/2} + (0.92q)^2]^{-1} \quad (3.6)$$

where $q = k/(\Omega_\nu h^2 \text{Mpc}^{-1})$ and $R_{f\nu} = 2.6(\Omega_\nu h^2)^{-1} \text{Mpc}$ is the characteristic damping length for neutrinos. We note that for $\Omega_\nu \simeq 0.30$ we obtain $R_{f\nu} = 8.66h^{-2} \text{Mpc}$, which is approximately the scale of equivalence. This is the reason why departure of the HDM and CHDM transfer functions from the CDM one are already visible at the *knee* of $T(k)$.

3.2.1 Gravitino WDM

The situation is very similar if, instead of massive neutrinos, the dark matter is provided by a particle that become non-relativistic at earlier epoch, but when the horizon is already of a cosmologically relevant size. We are referring here to WDM models. Qualitatively WDM models are just like HDM ones, but now the free-streaming length is smaller. Since WDM particles become non-relativistic earlier, when intermediate scale enter the horizon they are already non relativistic and therefore behave like CDM particles with respect to fluctuations, i.e. they don't free-stream. Their transfer function, as quoted in Bardeen et al. [88] is:

$$T_{WDM}(k) = T_{CDM}(k) \exp\left(-\frac{kR_{fs}}{2} - \frac{(kR_{fs})^2}{2}\right). \quad (3.7)$$

The value of R_{fs} depends upon the mass of the particle which provide the warm dark matter. In the case of gravitino (\tilde{G})WDM, presented in Chapt1, we computed

the transfer function as follows. We run the Boltzmann code assuming $\Omega_0 = 1$ and taking $g_* = 100$ and 200; the first value is rather representative of realistic cases, while the larger g_* corresponds to a very cold \tilde{G} population. We numerically computed the transfer function up to $k_{max} \simeq 1 \text{ Mpc}^{-1}$ (for $\Omega_0 = 1$ and $h = 0.5$), with higher k values requiring too high an accuracy to be reached within a reasonable computational time. However, we will show in the following that such a k_{max} value is larger than the free-streaming wavenumber, $k_{fs} = 2\pi/R_{fs}$. Therefore, we expect that the behaviour of the transfer function at $k > k_{max}$ has a marginal influence on the hierarchical clustering regime at $k < k_{fs}$, we are interested in (see next Chapter).

Then we computed the free-streaming scale for the $\Omega_0 < 1$ cases by resorting to the scaling relation $R_{fs} \propto m_{\tilde{G}}^{-1} \propto \Omega_{\tilde{G}}^{-1}$ (cf. eq.(1.33)) As a result, we find that

$$R_{fs} = 0.51 (\Omega_{\tilde{G}} h^2)^{-1} \left(\frac{g_*}{100} \right)^{-4/3} \text{ Mpc} \quad (3.8)$$

always provides an accurate fitting of the exponential suppression of fluctuations on small scales. We note that our value for R_{fs} is larger by a factor ~ 2.5 than that given by Kawasaki et al. [100]. This difference mainly comes from the fact that our value is directly obtained by fitting the exactly computed transfer function, while their value comes from the usual relation between R_{fs} and z_{nr} (see, e.g., eq.(9.88) in the Kolb & Turner book [52]), the redshift at which gravitinos becomes non relativistic, that represents an approximation to the R_{fs} value. We also confirm the warning by Bardeen et al. [88], who pointed out that the exponential cutoff in eq.(3.7) marginally underestimates the transfer function on intermediate scales, $0.1 \lesssim k \lesssim 0.5 (\Omega_0 h^2)^{-1} \text{ Mpc}^{-1}$. However, we did not attempt to look for a more accurate fitting expression, since (a) the effect is always quite small ($\lesssim 5\text{--}10\%$) and (b) we were interested in concentrating our analysis on the small scales relevant to galaxy and galaxy cluster formation, as will be more clear in the next Chapter.

In fig.3.2 we can see different transfer functions for warm dark matter parametrized by the mass of the particle m_o . In correspondence to the lowest mass chosen $T_{WDM}(k)$ is practically indistinguishable from $T_{HDM}(k)$, while the higher is the mass, the more $T_{WDM}(k)$ is similar to $T_{CDM}(k)$, the biggest discrepancies being on very small scales. Fig. 3.1 (left panel) show what happens in the case of gravitino warm dark matter if the value of g_* is changed: according to eq.(1.33) lowering g_* while keeping $\Omega_o = 1$ and the same baryon abundance is just like requiring a lower particle mass.

The situation is different for CHDM models (see fig.3.3). CHDM transfer function are always between CDM and HDM ones, the higher the hot dark matter

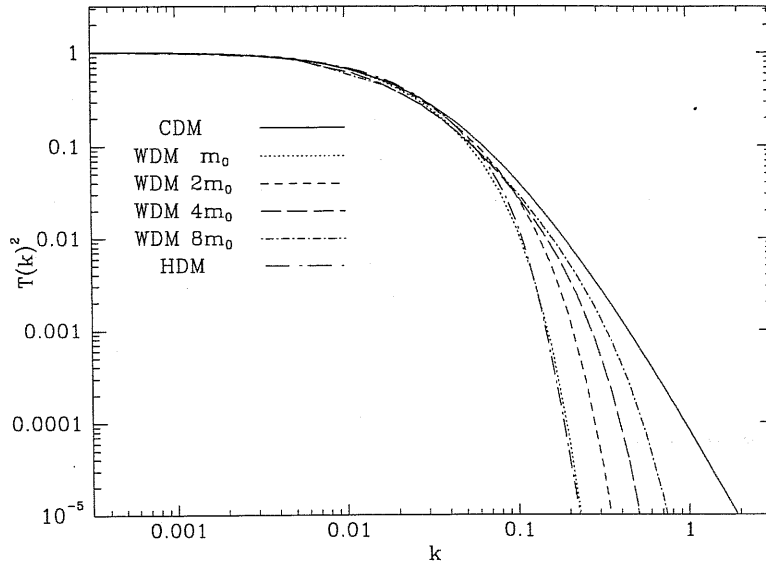


Figure 3.2: Effect of varying the particle mass m_o in WDM models. Figure kindly provided by S. Colombi.

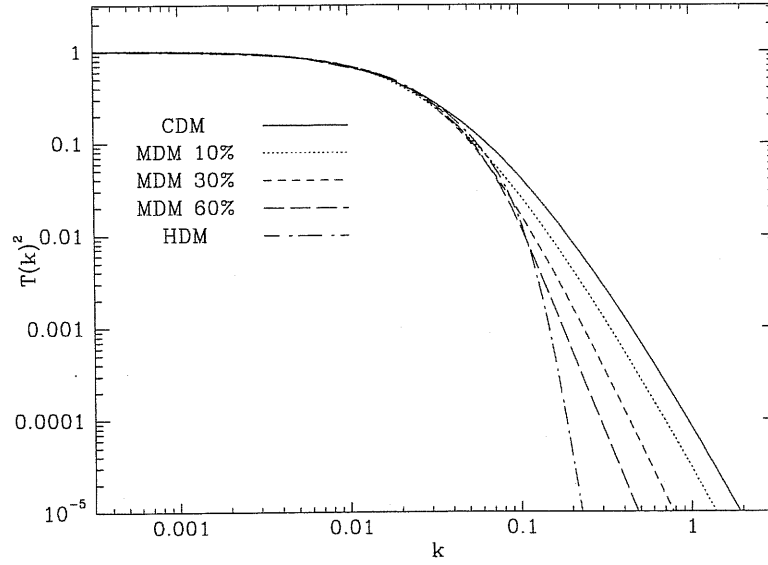


Figure 3.3: Effect of varying the hot dark matter content in CHDM models. Figure kindly provided by S. Colombi.

abundance, the more similar to HDM. The difference with the WDM case is that CHDM models do not present such a strong cutoff on small scales, and their slope at high k is more shallow.

As long as light gravitinos are concerned, we also analyzed a model in which there are both light gravitinos, behaving like WDM, and massive neutrinos, behaving like HDM (hereafter WHDM models). The two populations are characterized by a different free-streaming scale. Transfer functions for WHDM models have been computed for $\Omega_\nu = 0.1, 0.2, 0.3, 0.4$ and 0.5 in the case of only one massive neutrino (cf. ref.[101] for the effect of introducing more than one massive ν), taking $g_* = 100$ and 200 and always assuming $\Omega_0 = 1$. The analytical fitting is provided by eq.(3.7), where the CDM transfer function is replaced by the CHDM one, as provided by Pogosyan & Starobinski [102]. Taking $\Omega_{\tilde{G}} = 1 - \Omega_\nu - \Omega_b$, we find that eq.(3.8) always provides an accurate fitting to the exponential cutoff in the transfer function. The shapes of $T_{WHDM}(k)$ are plotted in Fig.3.4, showing both the effect of changing g_* at fixed Ω_ν (left panel) and the effect of changing Ω_ν at fixed g_* (right panel). From the left panel, we can see that WHDM models present a sharper cutoff on small scales if compared with CHDM, the discrepancies arising at high k values, $k \simeq 1 \text{ hMpc}^{-1}$. On the other hand, the effect of adding a hot component to the warm one is to reduce power already on intermediate scales ($k \simeq 0.1 \text{ hMpc}^{-1}$), as expected from what said in the previous section.

3.2.2 Volatile dark matter with radiative decay

We now discuss the power spectrum for volatile dark matter (VDM) models. Let us first consider the case $\phi \equiv \gamma$ [76, 77], and denote the volatile particle X . We first compare VDM with the standard CHDM model.

In conventional CHDM models, the hot component is assumed to be made of neutrinos with a mass of a few eV originally in thermal equilibrium in the early universe. In such a picture the redshift at which the neutrino becomes non-relativistic is $z_{nr} \simeq 1.4 \times 10^4 (m_\nu/10 \text{ eV})$ and the contribution of ν 's to Ω_0 is $\Omega_\nu \simeq 0.21 g_\nu (m_\nu/10 \text{ eV})$ (g_ν is the number of neutrino spin states with mass m_ν , originally in thermal equilibrium). Accordingly $z_{nr} \simeq 6.7 \times 10^4 \Omega_\nu / g_\nu$ and therefore z_{nr} and Ω_ν are not independent, as g_ν takes only suitable discrete values.

In the scenario we discuss here the VDM particles are produced by the decay of a more massive particle and are consequently never in thermal equilibrium. This means effectively that the parameters z_{der} and Ω_X , where X denotes the VDM species, can be varied independently. This causes VDM to have a quite wide range

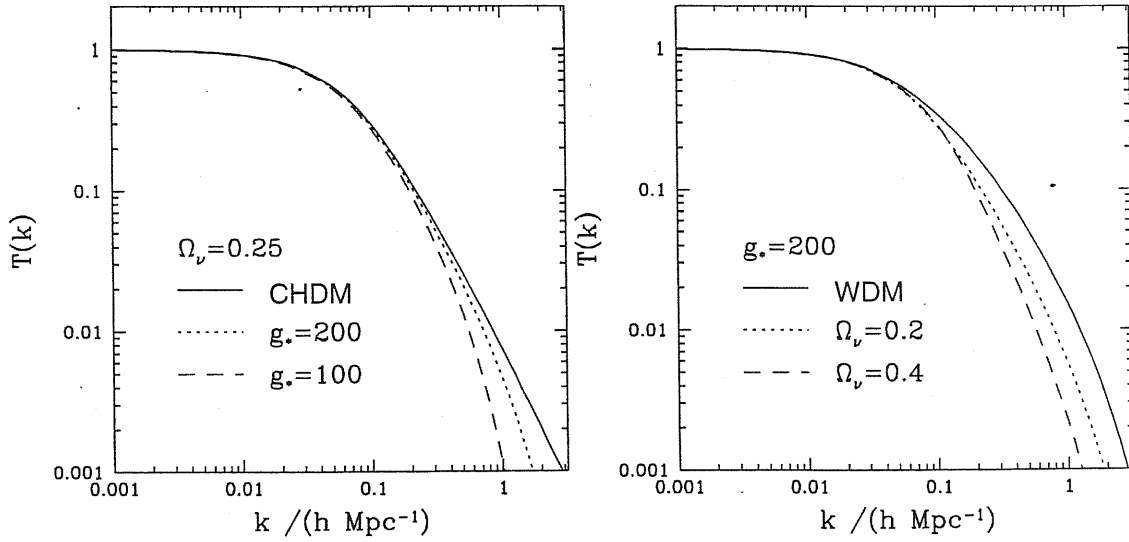


Figure 3.4: The shape of the transfer function for the warm + hot DM models. Left panel: the effect of varying g_* at a fixed value of $\Omega_\nu = 0.25$. Right panel: the effect of varying Ω_ν at a fixed $g_* = 200$.

of spectra, in general much more flexible than CHDM ones. Examples of VDM spectra are presented in fig.3.5 and compared with CDM. Here an initial Harrison-Zeldovich spectrum is assumed.

In [77] several cases of volatile spectra are studied. In order to better display the characteristic of VDM spectra, we consider only models with $\Omega_o = 1$, $H_0 = 50 \text{ km s}^{-1} \text{ Mpc}^{-1}$. As for the baryonic contribution, we consider the two values $\Omega_b = 0.05$ and $\Omega_b = 0.08$, which correspond to the central prediction of standard nucleosynthesis and to the 95% upper limit allowed by this constraint [103] given our chosen value of H_0 . Our criterion to select models in the Ω_X - z_{nr} parameter space can be sketched as follows. Let g^* be the number of helicity states which are allowed by nucleosynthesis and g_ν that associated to neutrinos which are present at the nucleosynthesis epoch. Then $g_X = g^* - g_\nu$ is the number of extra spin states to be associated to VDM particles. If z_{nr} is the redshift at which VDM becomes non relativistic, then the limit for Ω_X reads

$$\Omega_X \lesssim \frac{z_{nr}}{10^5} g_X \quad (3.9)$$

(see [76]). For each Ω_X , we choose three different z_{nr} values, namely $z_{nr} = 2 \times 10^4 \Omega_X$, $5 \times 10^4 \Omega_X$, and $2 \times 10^5 \Omega_X$.

According to [104], standard stellar light element abundances, combined with the results of nucleosynthesis calculations, allow up to $g^* = 7$, a value which is also quite close to the 2σ upper bound provided by [105], therefore we adopted the limit $g^* = 7$. Note, however, that [106] recently gave the more stringent constraint $g^* < 5$ at 95% C.L., which even conflicts with the *usual* 3 neutrino species.

The first value of z_{nr} given above corresponds to $g_X = 5$, if eq.(3.9) holds as an equality. Accordingly, the number of allowed neutrino species is $N_\nu = g_\nu/2 = 1$. This implies that only one massless neutrino is present at nucleosynthesis; the remaining two neutrinos are quite heavy and have been already decayed. Taking $z_{nr} = 5 \times 10^4 \Omega_X$ instead allows $g_X = 3$ with $N_\nu = 2$, while the choice $z_{nr} = 2 \times 10^5 \Omega_X$ allows one helicity state for VDM particles with $N_\nu = 3$.

Models with the first value of z_{nr} would thus be inconsistent with the [106] limits. But note also that, contrary to what one might naively expect, the results we quote below for higher values of z_{nr} cannot be used straightforwardly to accommodate this more stringent constraint because the shape of the transfer function depends explicitly on the number of massless neutrino species. As for Ω_X , we choose values in the interval $0.1 \leq \Omega_X \leq 0.5$, with step 0.1. For each value of Ω_X we allow for both the above baryonic fractions. In Table 3.1 we list the parameters for the resulting 30 models, on which we base the discussion of this paper.

For each model, we follow the evolution of the fluctuations in the baryonic (δ_b), cold (δ_c) and volatile (δ_X) components through equivalence and recombination epochs. An analytic fit to $T(k)$ is provided by the parametric expression:

$$T(k) = \left(1 + \sum_{j=1}^4 c_j k^{j/2} \right)^{-1}, \quad (3.10)$$

as suggested also by [93]. Note that the c_j generally depend on the redshift, due to the residual free-streaming of volatile particles. The values of the fitting parameters at $z = 0$ are given in Table 3.1, with k measured in Mpc^{-1} . The limiting scale down to which transfer functions are computed is 250 Kpc. In Table 3.1 the normalization constant A is also given, allowing for an initial power spectrum $P_{in} = Ak$. The spectrum amplitude A is estimated by matching the quadrupole ($l = 2$) value of $Q_{\text{rms-PS}} = 20 \mu\text{K}$ ([107]; [108], with an approximate 10% uncertainty on this value [109]).

It is worth pointing out a couple of important trends in the $T(k)$. Firstly, at fixed z_{nr} and N_ν , the amount of small scale power relative to large decreases as Ω_X is increased, due to the progressively larger effect of free-streaming. On the other hand, at fixed N_ν and Ω_X , the power on small scales increases relative to large scales

as z_{nr} is increased, since a larger z_{nr} corresponds to smaller velocities at the present time, and a consequent reduction of the effects of free-streaming. Moreover, note that in CHDM models the higher is the Ω_ν the higher is z_{nr} , so that spectra with a pronounced damping on the high k tale, caused by a high Ω_ν , generally don't differ too much from CDM on intermediate scale, because of the high z_{der} value. This is not the case in volatile models.

3.2.3 Volatile dark matter with non-radiative decay

Let us now consider the case of the decay of a heavy particle into a sterile scalar plus a volatile particle [86]. The characteristic feature of these models consists in having a sterile scalar that contributes to the radiation background, on top of radiation and standard massless neutrinos. In practice, it is just like if extra helicity states of neutrinos were added:

$$g_{\nu,eff} = g_\nu + (16/7)(11/4)^{4/3}\Omega_h d \quad (3.11)$$

where $d = z_{eq}/z_{der}$ and Ω_h is the volatile particle abundance. The effect of a greater g_ν is to shift the equivalence to lower redshift.

Also in this case we restricted the parameter space to $\Omega_o = 1$, $\Omega_\Lambda = 0$, $H_o = 50 \text{ km s}^{-1} \text{ Mpc}^{-1}$ and $\Omega_b = 0.1$. Within the above restrictions, we tested models at regular logarithmic interval for z_{der} , taking $\log_2 d = -1, \dots, 5$ (7 values) and at regular interval for hot-dark-matter density, taking $\Omega_h = 0.10, 0.12, \dots, 0.44$, and 0.45 (19 values). A non-systematic sampling of this parameter space allowed us to exclude some models a priori, reducing the total exploration to 120 models. As mentioned above, the parameter choices in the volatile case is much greater than in standard neutrino hot dark matter, however there is a significant overlap between these values of Ω_h and d and those allowed in mixed models with massive ν 's. One of our basic aims was then to obtain a quantitative estimate of the impact of the different momentum distribution on transfer functions. To this aim we re-evaluated $T(k)$, for a few mixed models with HDM made either by massive neutrinos or volatiles, but with the same values of Ω_h , d and $g_{\nu,eff}$.

The results of this comparison for two model sets are shown in Table 3.2. where one we can see that the amount of such shifts is modest. However, this does not decrease the relevance of volatile models, as they allow parameter choices which, otherwise, would be impossible with the standard 3 ν -flavours. Furthermore, these models require and allow a high level of radiation content.

In these models, we also allowed $P(k) = Ak^n T^2(k)$ with $n > 1$. For most models considered, $P(k)$ starts – at low k 's – with values similar to those of standard CDM.

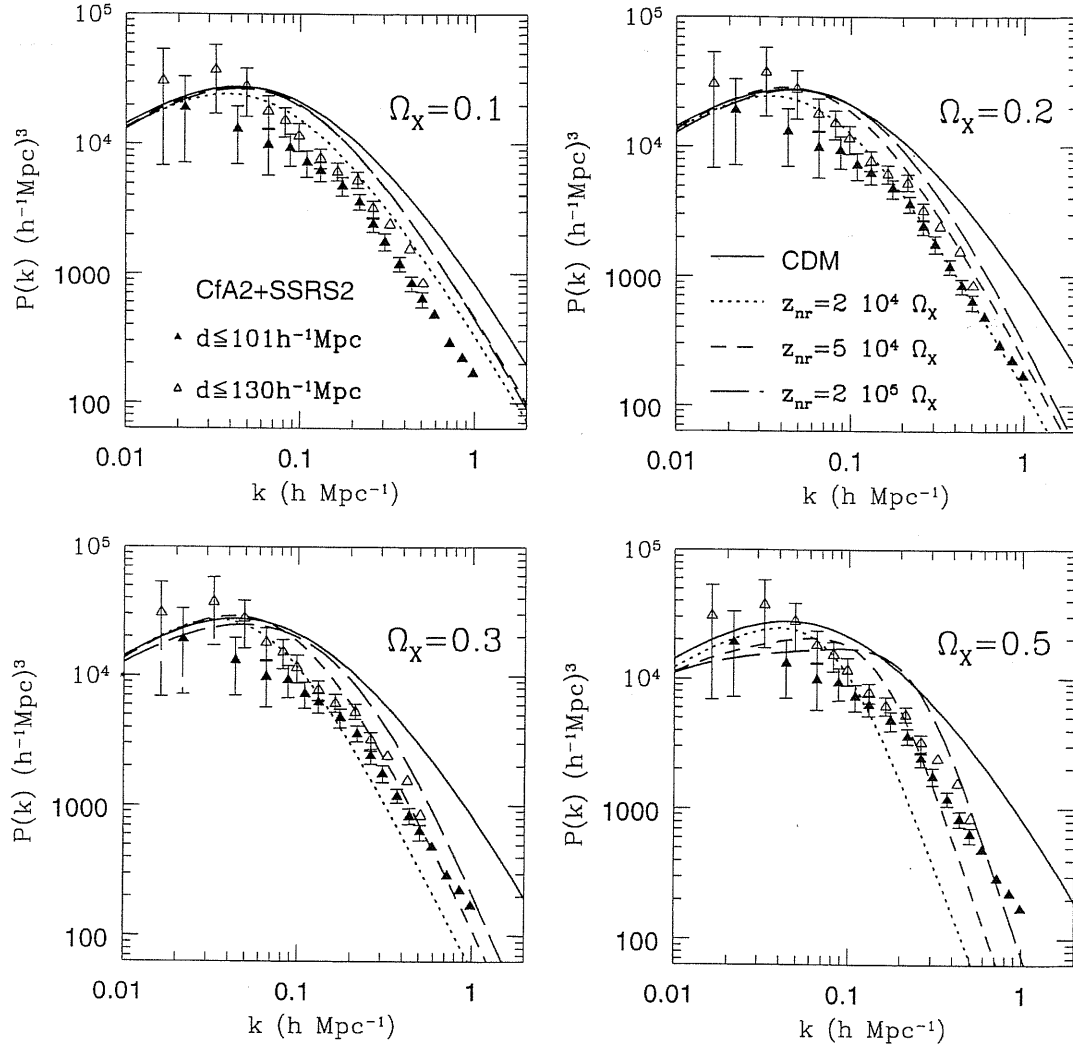


Figure 3.5: Comparison between observational and CVDM linear power-spectra in redshift space. Open and filled triangles are the power-spectrum for two volume limited subsamples of the combined CfA2+SSRS2 survey. Each panel refers to a fixed value of the volatile fraction Ω_X , while the dotted, short-dashed and long-dashed curves correspond to different z_{nr} . For reference, we also plot the CDM (solid curves). All the models are for $\Omega_b = 0.05$.

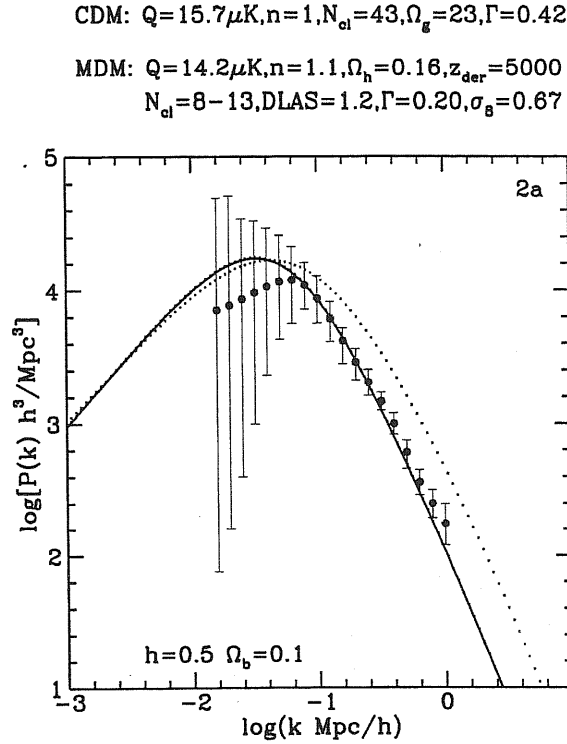


Figure 3.6: Mixed model spectra with volatile hot component (solid line), compared with standard CDM (dotted line). The LCRS reconstructed spectrum is also reported (3σ errorbars). This model is consistent with all constraints.

If $n > 1$, it soon abandons CDM behaviour, raising in a slightly steeper way. Both for $n > 1$ and $n = 1$, however, its bending at maximum is sharper. At the *r.h.s.* of the maximum it returns below CDM. At large k 's ($\sim 1 \text{ Mpc}^{-1}$), its decrease, sometimes, is (slightly) less steep than CDM.

Some examples of such behaviour are given in figs. 3.6 – 3.9 for volatile models and in figs. 3.10 – 3.12 for massive neutrino models; all cases we show have $n > 1$. Models are compared with CDM (dotted curve) and with the spectrum reconstructed by Lin et al. [110] from LCRS data (3σ errorbars). Models are ordered with increasing Ω_h . For volatile models, various values of d are considered, including high values; in particular, in fig. 3.8 we show a spectrum obtained with $z_{der} = 625$. The spectra shown in figs. 3.10– 3.11 are for physical models without extra SMLC. The spectrum in fig. 3.12, instead, is obtained adding an amount of SMLC corresponding to 3 massless ν 's.

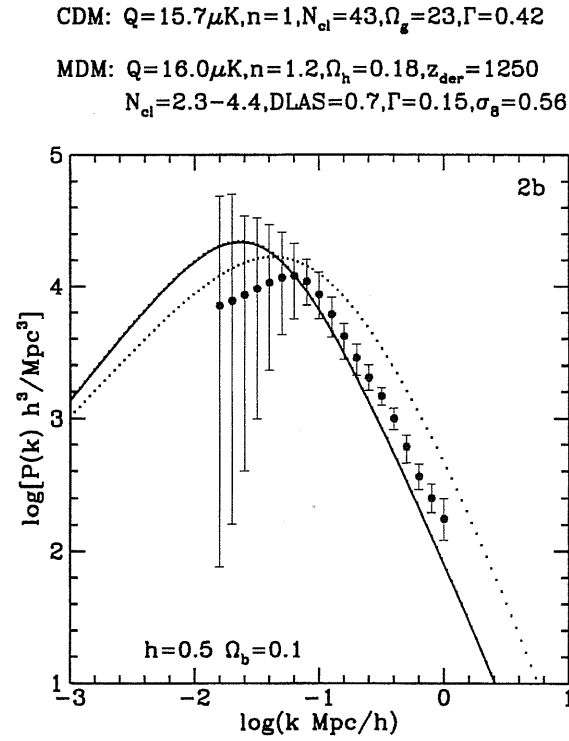


Figure 3.7: Mixed model spectra with volatile hot component (solid line), compared with standard CDM (dotted line). The LCRS reconstructed spectrum is also reported (3σ errorbars). This model is consistent with all constraints.

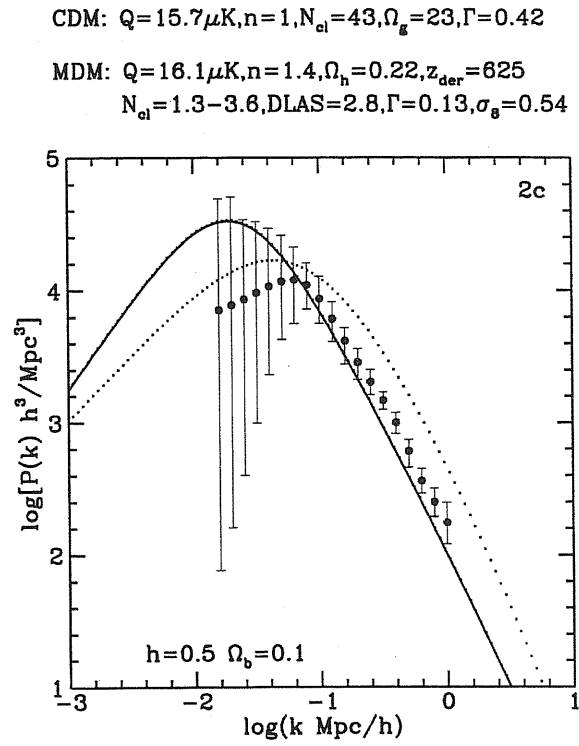


Figure 3.8: Mixed model spectra with volatile hot component (solid line), compared with standard CDM (dotted line). The LCRS reconstructed spectrum is also reported (3σ errorbars). This model is consistent with all constraints.

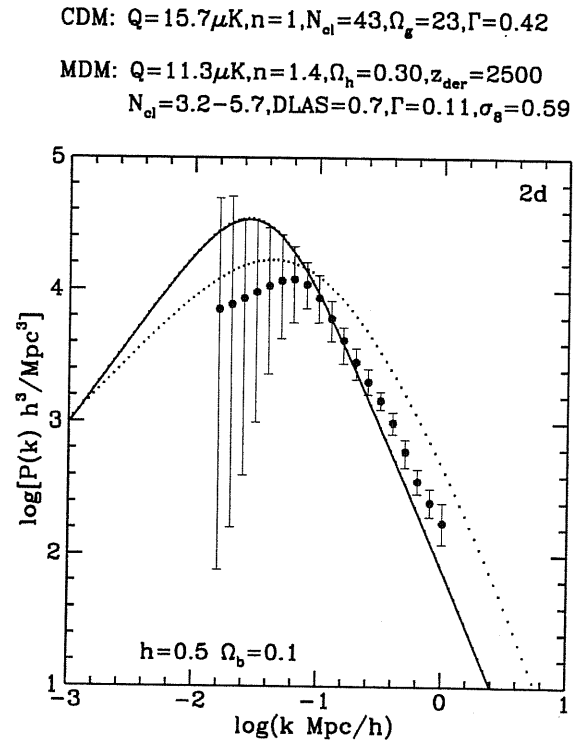


Figure 3.9: This Model is outside the contours plotted in fig.4.6 and has a small Γ . Models like it would agree with data for a still greater n .

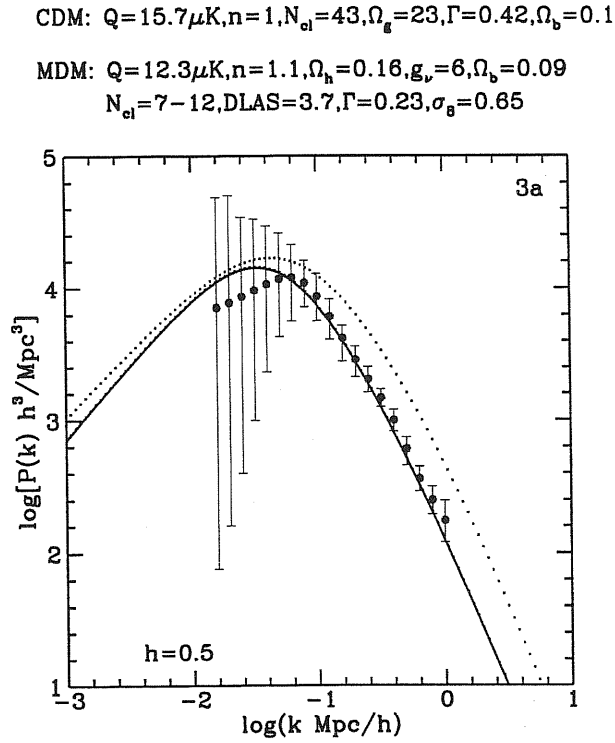


Figure 3.10: Mixed model spectra, with thermal hot component (solid line) compared with standard CDM (dotted line) and LCRS reconstructed spectrum. This model agrees with all constraints. Model *c* is in marginal disagreement, in spite of adding extra SMLC amounting to 3 massless ν 's.

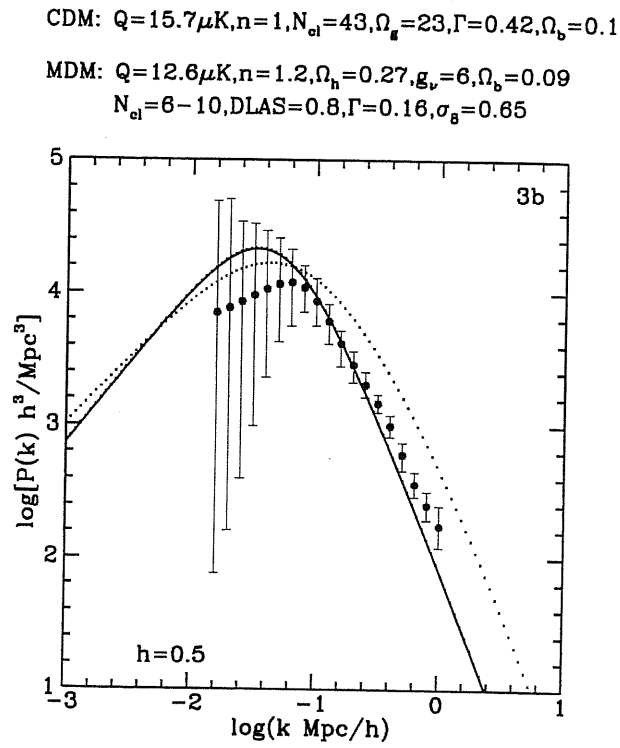


Figure 3.11: Mixed model spectra, with thermal hot component (solid line) compared with standard CDM (dotted line) and LCRS reconstructed spectrum. This model agrees with all constraints.

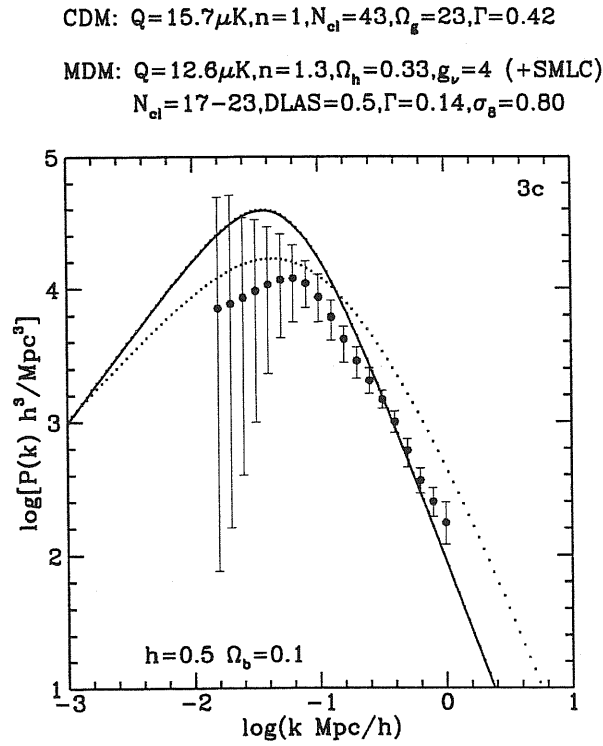


Figure 3.12: Mixed model spectra, with thermal hot component (solid line) compared with standard CDM (dotted line) and LCRS reconstructed spectrum. This model is in marginal disagreement, in spite of adding extra SMLC amounting to 3 massless ν 's.

3.3 The radiation spectrum

The radiation temperature anisotropy ($\Delta \equiv \frac{\delta T}{T} = \frac{1}{4} \frac{\delta \rho_r}{\rho_r}$) at a given spacetime point for a given direction \hat{n} can be considered as a superposition of plane-waves:

$$\Delta(\vec{x}, \hat{n}, \tau) = \int d^3k e^{i\vec{k} \cdot \vec{x}} \Delta(\vec{k}, \hat{n}, \tau) \quad (3.12)$$

$$= \int d^3k e^{i\vec{k} \cdot \vec{x}} \sum_{l=0}^{\infty} (-i)^l (2l+1) \Delta_l(\vec{k}, \tau) P_l(\mu), \quad (3.13)$$

where $\mu = \hat{k} \cdot \hat{n}$ and P_l are the Legendre polynomials.

With no loss of generality, we can consider an observer at the origin. The observed anisotropies $\Delta T/T$ in the sky can be decomposed in spherical harmonics:

$$\Delta T(\hat{n}) = \sum_{l=0}^{\infty} \sum_{m=-l}^l a_{l,m} Y_{l,m}(\hat{n}) \quad (3.14)$$

where $Y_{l,m}(\hat{n}) \equiv Y_{l,m}(\theta, \phi)$ are:

$$Y_{l,m}(\theta, \phi) = \sqrt{\frac{2l+1}{4\pi} \frac{(l-m)!}{(l+m)!}} P_l^m(\cos \theta) e^{im\phi} \quad (3.15)$$

The power spectrum is defined as:

$$C_l = \langle |a_{l,m}|^2 \rangle \quad (3.16)$$

where the brackets denote the ensemble average. Provided that in our model the anisotropies are a gaussian random field, the $a_{l,m}$ coefficients are randomly distributed variables with zero mean and variance given by the C_l . A mode with spherical harmonic index l probes an angular scale on the sky of $\theta \sim l^{-1}$. Broadly speaking, the C_l spectrum typically shows three different regimes, in correspondence to big, intermediate and small scales. On scales bigger than the horizon at recombination ($\lambda_{rec} \simeq 200h^{-1}$ Mpc, or equivalently $\theta_{hor} \simeq 2^\circ \Omega_o^\alpha$, with $\alpha = 1/2$ or $\alpha = 0$ for $\Omega_o \leq 1$ and $\Omega_\Lambda = 1 - \Omega_o$ respectively) the C_l is quite flat; on intermediate scales it shows an oscillatory behaviour and on small scales ($\theta \lesssim 10\Omega_o^{1/2}$ arcmin) oscillations are greatly damped, due to the width of the last scattering surface. Very big scales were not in causal contact at recombination, therefore they can provide direct information on primordial fluctuations. On the contrary, we shall see that intermediate scales are the ones where the different dark matter content may be tested. In any experiment, however, there is a theoretical unavoidable uncertainty due to the fact that we can only observe a two-dimensional projection of a single

realization of the statistical field. This uncertainty is called *cosmic variance*, and it amounts to $\frac{\delta C_l}{C_l} = \sqrt{\frac{2}{2l+1}}$. If the experiment is not full-sky, the uncertainty should be multiplied by a factor $\frac{4\pi}{A}$ (*sample variance*), where A stands for the area covered by the experiment.

C_l is related to $\Delta_l(\vec{k}, \tau)$ by the following expression:

$$C_l = (4\pi)^2 \int dk k^2 P_\psi(k) |\Delta_l(k, \tau_o)|^2 \quad (3.17)$$

where $P_\psi(k)$ is the initial power spectrum ¹.

At the present time τ_o and for a comoving scale given by the wavenumber k , we can compute Δ_l performing a time integral [111]

$$\Delta_l(k, \tau_o) = \int_0^{\tau_o} d\tau S(k, \tau) j_l[(\tau_o - \tau)k] \quad (3.18)$$

over the source function S , which depends upon inhomogeneity evolution inside the last scattering band and from it to now. $j_l(x)$ are spherical Bessel functions.

The physics of microwave background anisotropies due to adiabatic perturbations has been deeply investigated in the last few years (see, e.g., [112]). It has been shown that the characteristics of the peaks in the C_l spectrum are related to the physics of acoustic oscillations of baryons and radiation between the entry of a scale in the horizon and the last scattering band (primary anisotropies), and to the history of photons from last scattering surface to us (secondary anisotropies).

Background features, like the overall matter and radiation density content, h and Λ , have an influence both on the positions of the peaks and on their amplitude, but the latter also depends greatly on the baryon content Ω_b and more slightly on the characteristic of the hot component.

In the following we will sketch the most relevant physical effects that determine the shape of the power spectrum, and outline in particular how the shape of the power spectrum changes when different dark matter content are considered.

Under simple physical assumption, a fully analytic treatment of perturbations is possible and allows to predict the spectrum with a precision of 5 % – 10 % [113]. This approach is very simple and allows an easy comprehension of the most relevant effects that influence the shape of the power spectrum. As described more in detail in [114], the photon–baryon fluid at recombination can be described as a forced harmonic oscillator, where the forcing function depends upon the photon–to–baryon

¹ $P_\psi(k)$ is defined by the following relations: $\Delta_l(\vec{k}, \tau) \equiv \psi_i(\vec{k}) \Delta_l(k, \tau)$ and $\langle \psi_i(\vec{k}_1) \psi_i(\vec{k}_2) \rangle \equiv (P_\psi(k)/T^2) \delta_D(\vec{k}_1 + \vec{k}_2)$, where δ_D is the Dirac delta function.

energy ratio ($R = 3\rho_b/4\rho_\gamma$), as well as upon the potentials Ψ and Φ and their derivatives. As a first approximation, R is considered time independent.

The sources of primary anisotropies are gravity, the Doppler effect and intrinsic temperature variation:

$$\Delta = (\Psi - \hat{n} \cdot \vec{v} + \Theta)_{z_{rec}}. \quad (3.19)$$

While dealing with adiabatic perturbation, it can be shown that in the limit $R \rightarrow 0$:

$$\Psi + \Theta = \frac{1}{3}\Psi \cos(kc_s\tau) \quad (3.20)$$

and

$$\hat{n} \cdot \vec{v} = \frac{i}{3}\Psi \sin(kc_s\tau) \quad (3.21)$$

where $c_s = (3(1 + R))^{-1/2}$ is the sound speed.

From the above expressions we can see that in the limit $R \rightarrow 0$ we would expect no scale dependence of the fluctuation spectrum. In fact, the doppler term and the temperature-potential term oscillate with opposite phase but equal amplitude, so that when they are summed in quadrature they give:

$$\Delta^2 \propto \cos^2(kc_s\tau) + \sin^2(kc_s\tau). \quad (3.22)$$

Considering $R \rightarrow 0$ amounts to ignore the dynamical effects of baryons. When $R \neq 0$ is allowed, the amplitude of the cosine oscillations is enhanced by a factor $(1 + 3R)$, while it reduces the amplitude of the oscillations for the doppler term. Furthermore, the offset of the oscillation for the temperature-potential term is no longer zero but $-R\Psi$.

Since now the cosine oscillations have a bigger amplitude with respect to the sine ones, we expect to see a series of peaks in the C_l spectrum located at $kc_s\tau_{rec} = m\pi$. Furthermore, because of the offset, we expect the odd-numbered to be more pronounced than the even-numbered ones. Moreover, since $R \propto \Omega_b h^2$, the height of the peaks will be sensitive to these parameters.

The previous discussion is relevant for scales that has already entered the horizon at recombinations. On even larger scales, the doppler effect should not be considered, while the sum of the two terms (potential and temperature) gives $\Psi/3$. This is the *Sachs-Wolfe* effect [115], that causes the flat low- l tail in the radiation spectrum $l(l+1)C_l$.

3.4 Effects of dark matter content on the CMB

When a different kind of dark matter is considered, the radiation power spectrum is not greatly affected. When a mixture of cold and standard neutrino hot dark

matter is considered ([80, 116, 117], the most relevant feature is that the second and third doppler peaks are raised of about 10 % with respect to CDM. The first peak is also affected, but at a lower level. Authors [80] and [116] states that this difference is mainly due to an increase of the $\ddot{\Phi}$ that appears in the forcing function. The potential decay is mainly due to neutrino free-streaming, and it is most relevant on scales that have already entered the horizon at recombination.

The presence of massive neutrinos has also the effect of slightly shifting the peaks toward smaller l values. This effect is caused by the different expansion law, which implies a greater conformal time and sound horizon for redshifts $10 \lesssim z \lesssim 10^5$. A greater conformal time causes the peaks of the oscillations to be located at smaller k values, and therefore at smaller l . Moreover, last scattering happens at later conformal time in CHDM models if compared to CDM, and therefore a smaller integrated Sachs–Wolfe effect is expected.

The power spectrum for some WDM models has been evaluated by [118]. This author work out the power spectrum for two gravitino model with $g_* = 107$ and $g_* = 62$, and finds that the each WDM model differ from CDM at most for $\delta C_l/C_l = 0.03$ on all scales $l \lesssim 1400$, while the discrepancies between the two WDM models are of the order of $\delta C_l/C_l = 0.001$ at most. Differently from CHDM, the WDM spectra present lower doppler peaks if compared to CDM.

While considering decaying particles, a wide variety of spectra are obtained, which are caused by the different nature of the particles involved in the decay, different masses, decay-times and decay-products. We will first review all the possible scenarios for decaying neutrinos, and dedicate the last part of the paragraph to the case of volatile particles, presented in [87].

The case of neutrino decay has been deeply investigated during the past few years and tested against large scale structure [119, 120, 121]; its implications on the CMB spectrum has been discussed in [122, 123, 124, 125], but comparisons with recent CMB data start just now to be performed [126, 123, 127].

In the model considered by [123], the dark matter is constituted by a 30 eV neutrino that decays with a lifetime $\tau_\nu \simeq 1 - 2 \times 10^{23}$ sec into a lighter neutrino plus a photon. The photon produced in the decay causes the intergalactic medium to be gradually reionized and the complete reionization is attained at $z \simeq 30$. As long as the CMB is concerned, the main feature of this model is a great damping of the doppler peak, with the damping decreasing as the neutrino lifetime increases. These authors performed also a χ^2 analysis aimed to quantify the agreement-disagreement of this model with current data. The analysis tends to indicate a disagreement,

mainly because the trend of present data seem to suggest the presence of a pronounced doppler peak.

A similar case has been studied by [126], who analyzed the decay of a neutrino into a lighter one plus a sterile particle. They considered a neutrino mass larger than 10 eV, and a lifetime between 10^{13} and 10^{17} seconds (approximately $10^6 - 10^{10}$ years). In this case the main effect of this (quite) late decay is to increase the radiative component at late times when the Universe is well in the matter dominated era. This causes the potential to vary, and consequently large scale anisotropies are boosted via the integrated Sachs–Wolfe effect. The longer is the lifetime of the decaying particles, the lower are l values where the effect is evident. Even if there is no reionization in these models, the predicted C_l of this model shows similarities with the previous case, in that there is not much difference in the amplitudes of anisotropies between the plateau and the first peak. This fact leads the authors to conclude that such a model fails to reproduce current CMB observations.

If larger masses and shorter lifetimes are considered [122, 125], late integrated Sachs Wolfe is no longer present, but the delayed matter–radiation equivalence causes a much higher first doppler peaks, and also the second and the third doppler peaks are shifted to the right. This is quite similar to what happens with volatile models, therefore we postpone the detailed description of its consequences to the next session.

3.4.1 CMB spectra for volatile models

In this section we shall analyze in detail the angular spectrum of volatile models with non–radiative decay, outlining its peculiarities with respect to standard CDM and CHDM where neutrinos provide the *thermal* contribution of dark matter. In order to do so, we needed to modify available public codes, like CMBFAST [111], allowing them to deal with a hot component whose momentum distribution is the one of the volatile dark matter.

As outlined in the previous Chapter, volatile and neutrino models, for given Ω_h and d , are expected to include a different amount of SMLC. In neutrino models SMLC is less than in pure CDM and even vanishes if all ν 's are massive (unless extra SMLC is added *ad hoc*). In volatile models, instead, SMLC is however more than in pure CDM, as scalar ϕ 's are added on top of standard massless ν 's.

Some C_l spectra of volatile models are presented in figs.4.7 – 4.11 of Chapter 4. They show two main features, if compared with standard CDM: the first doppler peak is higher and the second and third doppler peaks are slightly shifted to the right. In principle, we expect volatile model spectra to differ from neutrino model

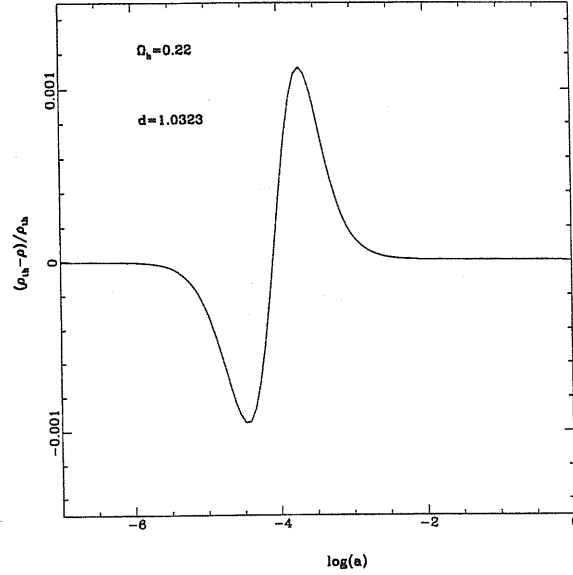


Figure 3.13: density evolution of a volatile model in comparison with the corresponding technical neutrino case.

spectra because of the momentum distribution of volatiles and the extra SMLC they have to include. In the following, we shall try to disentangle these two effects.

To this aim we coupled each volatile models with a *technical* neutrino case with identical Ω_h and d , but a greater number of neutrino degrees of freedom, so to ensure equal high-redshift energy densities. In fig.3.13 we report the scale-factor dependence of the energy densities $\rho(a)$ of volatiles and a massive neutrinos in two coupled models. In the case shown, the two energy densities never differ in ratio more than 10^{-3} ; for different choice of the parameters the curve is just shifted to higher or lower redshifts according to the value of z_{der} . More in detail fig.3.13 states that volatiles have a slower derelativization than neutrinos: the transition phase from the relativistic to the non-relativistic regime starts earlier and goes on for a longer time. This behaviour is related to the different shapes of the two distribution functions, and to the fact that the volatile one is smoother around $\langle p \rangle$, which corresponds to a value significantly smaller than its maximum, after which it is rapidly cutoff (see eqs.1.43–1.44 in Chapter 1).

Friedmann equations show that $\tau(a)\sqrt{\rho(a)}$ is approximately constant. Hence, once we know $\rho(a)$, we can perform a comparison between the conformal times of coupled volatile and *technical* neutrino cases. It shows a marginal discrepancy as already the $\rho(a)$ in the volatile and *technical* neutrino cases are very similar, and

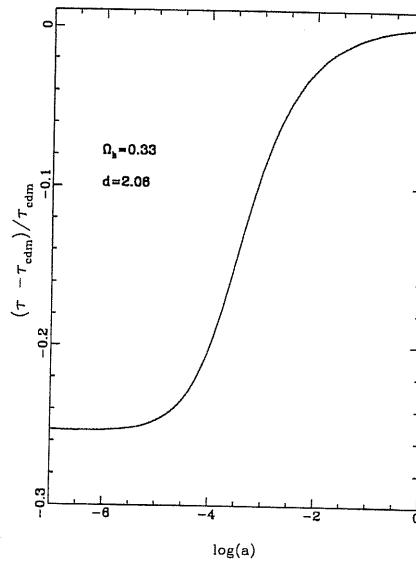


Figure 3.14: comparison of conformal time in a CDM standard model and in a volatile model. At high redshifts, volatile models typically show a smaller conformal time.

moreover the hot component always contributes as a small fraction of the total energy density. On the contrary, if a similar comparison is performed between standard CDM and volatile models, big discrepancies are found, especially at high redshifts. In fact, in the volatile cases the relativistic background is greater due to the contribution of the sterile component, and the conformal time is therefore smaller than in the CDM case (see fig.3.14).

This implies visible effects on the position of the doppler peaks, which are due to the oscillatory phase with which the photon-baryon fluid meets the last scattering band. As already said before, in adiabatic fluctuations the photon-baryon fluid oscillates as $\cos(kr_s)$, where k is the comoving scale and r_s is the sound horizon ($r_s = \int_0^{\tau(a)} d\tau c_s(a)$, $c_s(a)$ is the sound speed). Given the photon-baryon ratio, $r_s(a)$ follow a similar trend as $\tau(a)$. Since in volatile models $\tau(a)$ is smaller than in CDM, so will be $r_s(a)$, and the peaks of the spectrum will appear in correspondence to higher k (i.e. higher l) values. This is a specific features of these models, in neutrino models the same effect plays a role, but shifting the peaks in the opposite direction [116]. For a given primordial spectral index n , the height of the peaks is fixed by (i) the ratio between baryon and photon densities, i.e. $\Omega_b h^2$, and (ii) the ratio between matter and radiation densities. At fixed Ω_b and h the main reason for a higher doppler peak in volatile models (with respect to CDM) is the delayed

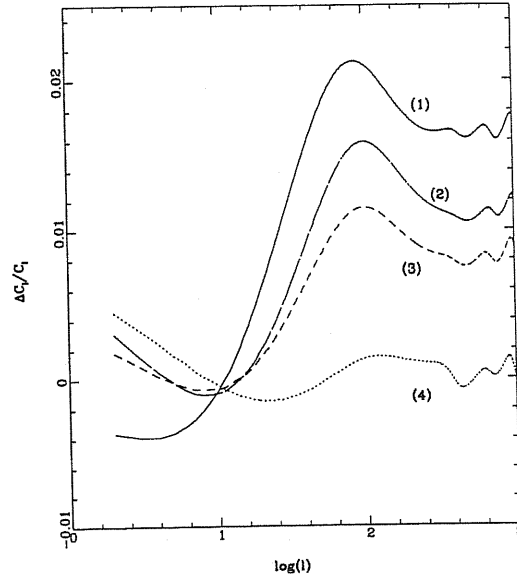


Figure 3.15: differences in the radiation power spectrum between the volatile case and the technical neutrino case. The model parameters are the following: 1) $\Omega_h = 0.16$, $d = 4.25$; 2) $\Omega_h = 0.22$, $d = 1.03$; 3) $\Omega_h = 0.22$, $d = 2.06$; 4) $\Omega_h = 0.33$, $d = 2.06$.

matter-radiation equivalence, for which both SMLC and, possibly, volatiles can be responsible. In neutrino models without *ad-hoc* SMLC, only the possible delay due to late derelativizing ν 's may exist. This is why volatile C_l spectra and standard neutrino ones look so different. However, there is a tiny further contribution in the boost of the peak due to the free-streaming of the hot component. Several authors ([80], [116]) have shown that even in high z_{der} neutrino models the doppler peaks are enhanced with respect to CDM, and in that case the free-streaming of the hot component is to be considered responsible for the enhancement. Free-streaming, in fact, causes a decay in the potential Φ which contributes as a forcing factor (through $\ddot{\Phi}$) in the equations whose solution are the *sonic* oscillations in the photon-baryon fluid, displacing their zero-point and, henceforth, the phase by which they enter the last scattering band. In the standard neutrino case, this effect causes a variation of 10% at most on the C_l , and typically of 2% on the first doppler peak.

In principle one can expect that the different momentum distribution of volatiles may alter the free-streaming behaviour. Such differences, if they exist, can be found by comparing volatile spectra with the *technical* neutrino ones.

The differences between the two spectra are presented and shown in fig.3.15, and amount to 2% at most. Although modest, this is another feature that characterizes

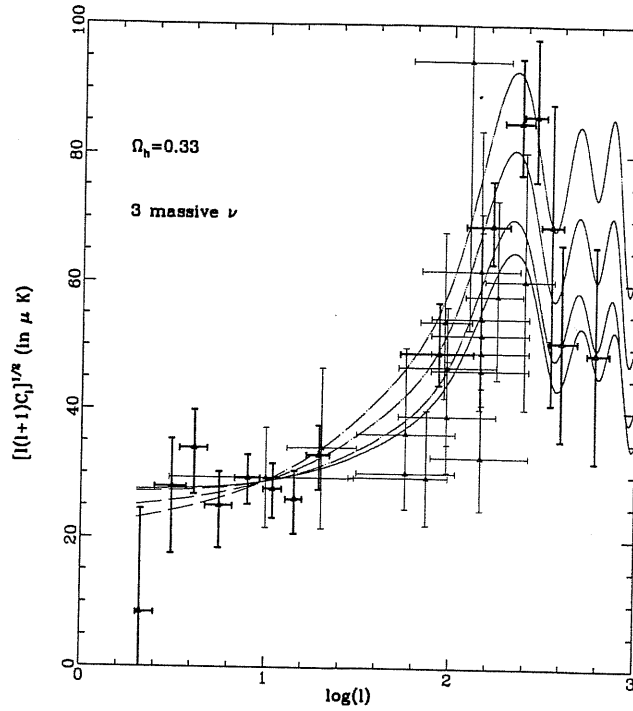


Figure 3.16: a standard neutrino model with different n values. C_l curves from bottom to top correspond to $n = 1, 1.1, 1.2, 1.3$. Bold data points refer to COBE, CAT, Saskatoon, see Scott et al. (1995) for a summary of all the experiments.

volatile models with respect to neutrino one. In comparison with such finely tuned predictions from theoretical models, currently available data are still affected by huge errorbars. However, some feature seems already evident from them. A comparison of model predictions with data shows that the doppler peak observed by the Saskatoon experiment [128] exceeds the one expected in pure CDM once it is normalized to COBE data [129]. While it is evident that volatile models show a higher doppler peak, it is clear that a fit could be reached also changing other parameters, *e.g.*, by taking $n > 1$. In fig.3.16 we show what happens in neutrino models if the spectrum is anti-tilted to $n = 1.1$ and to $n = 1.2$. Indeed, the first doppler peak is raised (which is desirable), but also the following peaks are raised, making difficult the agreement with the results from the CAT experiment [130]. In the next chapter similar considerations will be used in order to constrain the whole set of volatile models.

N_ν	Ω_X	$z_{\text{nr}}/10^4$	$A(10^7)$	c_1	c_2	c_3	c_4
$\Omega_b = 0.05$							
1	0.1	0.2	1.300	-0.6133E+0	0.1494E+2	0.1220E+3	0.6733E+2
1	0.1	0.5	1.306	-0.4284E+0	0.1212E+2	0.9742E+2	0.6607E+2
3	0.1	2.0	1.311	-0.3665E+0	0.1542E+2	0.7916E+2	0.8917E+2
1	0.2	0.4	1.318	0.5110E-1	-0.1016E+1	0.1924E+3	0.1559E+3
1	0.2	1.0	1.319	0.1032E-1	0.4255E+1	0.1113E+3	0.1629E+3
3	0.2	4.0	1.327	0.4886E-2	0.1624E+2	0.3607E+2	0.1997E+3
1	0.3	0.6	1.354	0.1263E+1	-0.2246E+2	0.2301E+3	0.3903E+3
1	0.3	1.5	1.303	-0.5240E+0	0.1509E+2	0.2086E+2	0.4061E+3
3	0.3	6.0	1.266	-0.1997E+1	0.5180E+2	-0.1305E+3	0.4194E+3
1	0.4	0.8	1.325	0.1052E+0	0.8104E+1	-0.1939E+2	0.1053E+4
1	0.4	2.0	1.248	-0.2475E+1	0.5754E+2	-0.2466E+3	0.9205E+3
3	0.4	8.0	1.168	-0.5488E+1	0.1240E+3	-0.4753E+3	0.8259E+3
1	0.5	1.0	1.249	-0.3115E+1	0.1033E+3	-0.7761E+3	0.2781E+4
1	0.5	2.5	1.107	-0.7916E+1	0.1846E+3	-0.9825E+3	0.2091E+4
3	0.5	10.0	1.063	-0.9233E+1	0.1943E+3	-0.8273E+3	0.1325E+4
$\Omega_b = 0.08$							
1	0.1	0.2	1.323	-0.1009E-1	0.8960E+1	0.1418E+3	0.6768E+2
1	0.1	0.5	1.319	-0.2039E-1	0.5736E+1	0.1202E+3	0.6457E+2
3	0.1	2.0	1.318	-0.6469E-1	0.6622E+1	0.1021E+3	0.8145E+2
1	0.2	0.4	1.308	-0.4181E-1	-0.9723E+1	0.2449E+3	0.1497E+3
1	0.2	1.0	1.348	0.9112E+0	-0.1115E+2	0.1681E+3	0.1530E+3
3	0.2	4.0	1.317	-0.1257E+0	0.1017E+2	0.5465E+2	0.1926E+3
1	0.3	0.6	1.443	0.3845E+1	-0.5984E+2	0.3617E+3	0.3668E+3
1	0.3	1.5	1.346	0.7783E+0	-0.3884E+1	0.8075E+2	0.3960E+3
3	0.3	6.0	1.203	-0.3672E+1	0.6458E+2	-0.1643E+3	0.4436E+3
1	0.4	0.8	1.392	0.2294E+1	-0.3311E+2	0.1601E+3	0.1005E+4
1	0.4	2.0	1.244	-0.2619E+1	0.6079E+2	-0.2866E+3	0.1030E+4
3	0.4	8.0	1.159	-0.5641E+1	0.1198E+3	-0.4603E+3	0.8270E+3
1	0.5	1.0	1.279	-0.2064E+1	0.8336E+2	-0.6956E+3	0.2808E+4
1	0.5	2.5	1.148	-0.6521E+1	0.1636E+3	-0.1016E+4	0.2456E+4
3	0.5	10.0	0.925	-0.1341E+2	0.2297E+3	-0.9345E+3	0.1439E+4

Table 3.1: Model parameters and power spectra (numbered from 1 to 30). Column 1: number of massless neutrino species; Column 2: volatile fractional density; Column 3: redshift at which the volatile component becomes non-relativistic (in units of 10^4); Column 4: Normalization coefficient Columns 4 to 8: fitting parameters of the transfer functions [see eq.(3.10)].

L/Mpc	cold	hot	baryons	total
0.2000E+05	1	1	1	1
0.5120E+03	1	1	1	1
0.2048E+03	0.9995E+00	0.9996E+00	0.9995E+00	0.9995E+00
0.8192E+02	0.1001E+01	0.1002E+01	0.1001E+01	0.1001E+01
0.3277E+02	0.1003E+01	0.1004E+01	0.1003E+01	0.1003E+01
0.1311E+02	0.1003E+01	0.1004E+01	0.1003E+01	0.1003E+01
0.5243E+01	0.1005E+01	0.1003E+01	0.1005E+01	0.1004E+01
0.2097E+01	0.1007E+01	0.1012E+01	0.1007E+01	0.1009E+01
0.8389E+00	0.1006E+01	0.1036E+01	0.1006E+01	0.1015E+01
0.2000E+05	1	1	1	1
0.5120E+03	1	1	1	1
0.2048E+03	0.9995E+00	0.9996E+00	0.9995E+00	0.9995E+00
0.8192E+02	0.1001E+01	0.1001E+01	0.1001E+01	0.1001E+01
0.3277E+02	0.1003E+01	0.1002E+01	0.1003E+01	0.1003E+01
0.1311E+02	0.1003E+01	0.1002E+01	0.1003E+01	0.1003E+01
0.5243E+01	0.1005E+01	0.1001E+01	0.1005E+01	0.1005E+01
0.2097E+01	0.1007E+01	0.1008E+01	0.1007E+01	0.1007E+01
0.8389E+00	0.1006E+01	0.1026E+01	0.1006E+01	0.1008E+01

Table 3.2: Ratio between transfer functions in volatile and thermal models (T (vol)/ T (ther)) at various comoving scales for different components. The upper part refers to models with $\Omega_h = 0.3$ and 3 massive neutrinos, the lower part to models with $\Omega_h = 0.1$ and 1 massive neutrino. In both cases $\Omega = 1$, $h = 0.5$ and $\Omega_b = 0.1$.

4 Comparison with Observations

4.1 Introduction

In this Chapter we will compare some predictions from the previously discussed cosmological models with observations. We will restrict our analysis to quantities that can be predicted using linear theory, disregarding all the issues related to non-linear structure formation.

Linear theory is valid in the nearby Universe only for objects on very large scale, while going back in time towards higher redshifts it can be applied to fluctuations on smaller and smaller scales. CMB fluctuations are observed now as they were at $z \simeq 1000$, so they can be predicted with linear theory on all relevant scales. Fluctuations on galactic scale can be considered linear only up to $z \simeq 3 - 4$, while the smallest objects we assume to be still in a linear stage today are galaxy clusters. Even if in principle CMB fluctuations are predictable with high accuracy on all scales, observations, that have only been performed on scales bigger than $\simeq 10$ arcmin, still show big errorbars. Therefore, nowadays comparison of predictions with the observations is performed normalizing the power spectrum to COBE (i.e. to very large scale CMB fluctuations) and then computing the predicted quantities concerning large scale structure (LSS). Very recent attempts of all present CMB data to constrain cosmological parameters already allow to draw some conclusions, even if still with great uncertainties. Future CMB experiments will provide very accurate determination of the CMB power spectrum down to scales $\simeq 10$ arcmin, therefore ensuring a significant overlap with scales probed by LSS. It is therefore evident that a joint analysis of CMB and LSS will become more and more necessary in the future.

4.2 The mass variance and the shape parameter

In the previous Chapter we introduced the matter power spectrum $P(k)$. Here, in order to provide a more quantitative description of the clustering, we compute σ_M , which is defined as the r.m.s. fluctuation amplitude:

$$\sigma_M^2 = \frac{1}{2\pi^2} \int_0^\infty dk k^2 P(k) W^2(kR_M), \quad (4.1)$$

where the length scale associate to the mass scale M , $R_M = (4\pi\bar{\rho}/3)^{-1}M^{1/3}$, is the radius of the top-hat sphere whose Fourier representation is given by $W(x) = 3(\sin x - x \cos x)/x^3$ ¹. The mass variance is the quantity that most directly shows which scales are getting non-linear first. In a CDM model, the mass variance is always increasing with the wavenumber k , so that we expect fluctuations on small scales to become non-linear first, and structures on bigger scales to form for assemblage of small lumps. This scenario is usually referred to as *bottom-up* structure formation. The situation, however, may be different in models where the power spectrum is highly dumped on small scales, as, for example, in WDM models. If this is the case, the mass variance stops growing on scales where the contribution of the power spectrum become negligible. In fig.4.1 the mass variance of a CDM case and of a gravitino-WDM case is plotted. According to fig.4.1, it turns out that the effect of replacing the CDM component with light gravitinos is that of eliminating the hierarchical clustering below some free-streaming mass scale. In order to provide an estimate of the free-streaming mass scale for gravitino-WDM models, we resort to the almost Gaussian cutoff at large k , to define it as

$$M_{fs} = (2\pi R_{fs}^2)^{3/2} \bar{\rho} \simeq 0.55 \left(\frac{g_*}{100} \right)^{-4} (\Omega_{\tilde{G}} h^2)^{-3} \Omega_0 h^2 M_{12}, \quad (4.2)$$

where $\bar{\rho}$ is the average cosmic density and $M_{12} = 10^{12} M_\odot$. Therefore, eq.(4.2) provides the limiting mass for the development of hierarchical clustering: structures of smaller masses form after structure of mass larger than M_{fs} , as a product of their fragmentation. As a consequence, we expect that a crucial constraint for the whole class of WDM-dominated models will come from the abundance of high-redshift cosmic structures.

A quantity strictly related to the mass variance is the shape parameter Γ . The shape parameter was introduced by [131], and is defined as:

$$\Gamma = 7.13 \times 10^{-3} (\sigma_8/\sigma_{25})^{10/3}. \quad (4.3)$$

¹In this Thesis the mass variance is equivalently referred to as σ_M or σ_R , where $R \equiv R_M$. For example, σ_8 is the mass variance over a scale of $8h^{-1}$ Mpc.

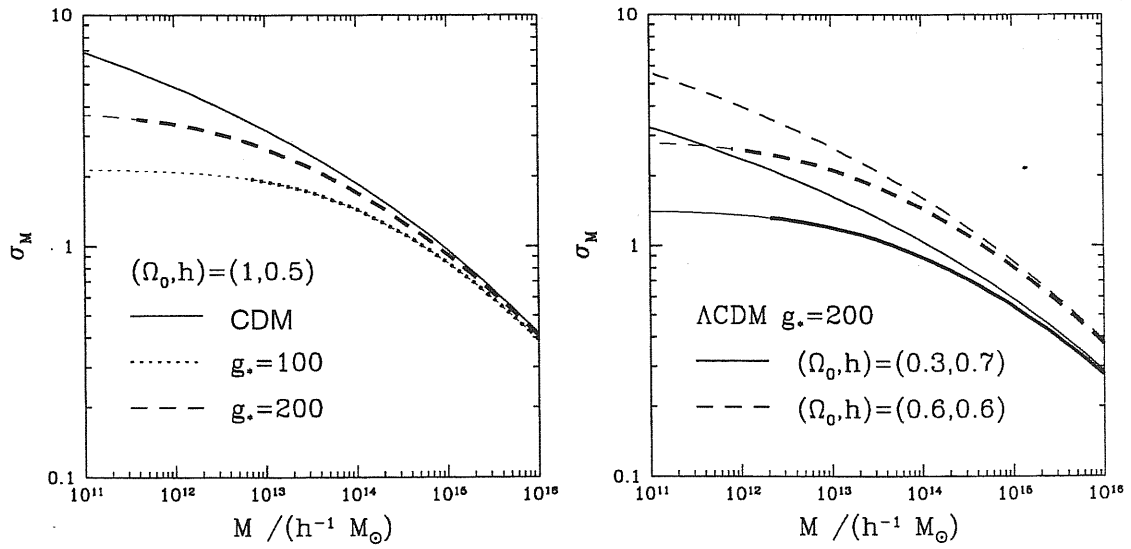


Figure 4.1: The mass-scale dependence of the r.m.s. density fluctuations within a top-hat sphere. Left and right panels are for the same models as reported in fig.3.1. Heavy and light curves are for WDM and CDM cases. As for the WDM curves, the value of M at which they become lighter corresponds to the value of the free-streaming mass.

It is related to the *excess power* parameter

$$EP = \frac{(\sigma_{25}/\sigma_8)}{(\sigma_{25}/\sigma_8)_{CDM}}$$

by the relation: $\Gamma \simeq 0.5(EP)^{-3.3}$. It has been argued that CDM transfer function may well be parametrized by Γ . In fact, Γ is related to background quantities $\Gamma \simeq \Omega_o h$, while the more precise value $\Gamma = \Omega_o h \exp(-\Omega_b - \sqrt{2h}\Omega_b/\Omega_o)$ accounts for the presence of a non-negligible baryon fraction Ω_b [132]. Note, however, that this is not generally the case for mixed models, since the presence of the hot component may well affect the $8h^{-1}$ Mpc scale. For the sake of comparison with observations, we considered the result obtained from APM galaxies $\Gamma = 0.23 \pm 0.04$ [133]. In a more recent work, Borgani et al. (1997) [134] give the interval 0.18–0.25 obtained from the Abell/ACO sample.

4.2.1 Bulk Velocities

The rms bulk velocity, $V_{\text{bulk}}(R)$, is defined as the rms matter velocity after smoothing over a volume of size R . For $\Omega_o = 1$ it is connected to the power-spectrum according to

$$V_{\text{bulk}}^2(R) = \frac{f(\Omega) H_0^2}{2\pi^2} \int_0^\infty P(k) W^2(kR) dk, \quad (4.4)$$

where $W(kR)$ is the window function specifying the shape of the smoothing volume, and $f(\Omega_o)$ is the linear growing factor $f(\Omega_o) \approx \Omega_o^{0.6}$. By comparing eqs.(4.1) and (4.4), it is clear that $V_{\text{bulk}}(R)$ gives more weight to long wavelength modes than σ_M . Therefore, we expect bulk velocities on large scales to depend only on the Q_{rms-PS} normalization and not on the profile of the transfer function.

Since bulk flows refer to quite big scales, when theoretical models are compared to the data the main information one can obtain is on the spectral index. As we will see below, bulk flows are quite insensitive, for example, to the content of hot dark matter of the model.

The first report of bulk velocities for ellipticals within spheres of $\sim 60h^{-1}$ Mpc is $V_{\text{bulk}} = 599 \pm 104$ [135], but

it has been soon recognized that this value had been overestimated and that the effective window should have been much smaller. A more recent estimate report $V_{\text{bulk}} = 360 \pm 40$ [136].

Reliable V_{bulk} data for top-hat spheres centered on the Local Group on scales of few tens of Mpc are provided by the POTENT reconstruction method (e.g. [137]; see also [138], and references therein).

It should be mentioned, however, the attempt of recovering the power spectrum from the smoothed mass density field reconstructed by POTENT [139]. These authors estimated the power spectrum in the interval $0.04 \leq k \leq 0.2 h\text{Mpc}^{-1}$, and found a logarithmic slope of the power spectrum at $k = 0.1$ of -1.45 ± 0.5 . This feature translates into the estimate $\sigma_8 \Omega^{0.6} \simeq 0.7 - 0.8$. These authors also claim that a comparison of the mass power spectrum on scales $\sim 100 h^{-1}\text{Mpc}$ with the large-scale fluctuations observed by COBE rules out low Ω_o values ($\Omega_o \sim 0.2$), independently of the Λ value. Standard CDM, as well, is rejected at the 2σ level, while each of the following modification provide a good fit: $n \leq 1$, $\Omega_\nu \sim 0.3$, $\Omega_o \leq 1$. We computed bulk velocities for volatile models only. We didn't compute the bulk velocities for the gravitino-WDM model because we don't expect WDM predictions to differ much from CDM ones.

4.2.1.1 Volatile particles and bulk flows

In fig.4.2 we compare our model predictions with the latest POTENT data (courtesy of A. Dekel).

In order to account for the velocity smoothing procedure in the reconstruction method, we convolved the power-spectrum in eq.(4.4) with a Gaussian filter of radius $R_f = 12 h^{-1}\text{Mpc}$. As expected, any difference between models at large scales is negligible and all of them are in remarkable agreement with data. On smaller scales ($\lesssim 40 h^{-1}\text{Mpc}$) the predicted V_{bulk} values tend to be larger than the observational one. In this respect, models with $\Omega_X \geq 0.4$ perform better, thanks to the steep $P(k)$ profile at large k , although this is unfortunately inconsistent with galaxy clustering data. On the other hand, independent estimates of bulk flows (e.g. [140]) agree with the POTENT one only on scales $R \simeq 50\text{--}60 h^{-1}\text{Mpc}$. Therefore, we do not regard this marginal discrepancy as a serious problem for any of the models we have considered.

4.3 Press–Schechter theory

The comparison we make between theory and observations, based on the spectrum integrated with a top-hat filter, is well established in the literature.

However, there are exceptions, namely the calculations based on objects abundances, which contain greater theoretical uncertainties than other measures. We will therefore discuss this point more in detail.

The standard technique consists in using Press–Schechter theory [141], which is

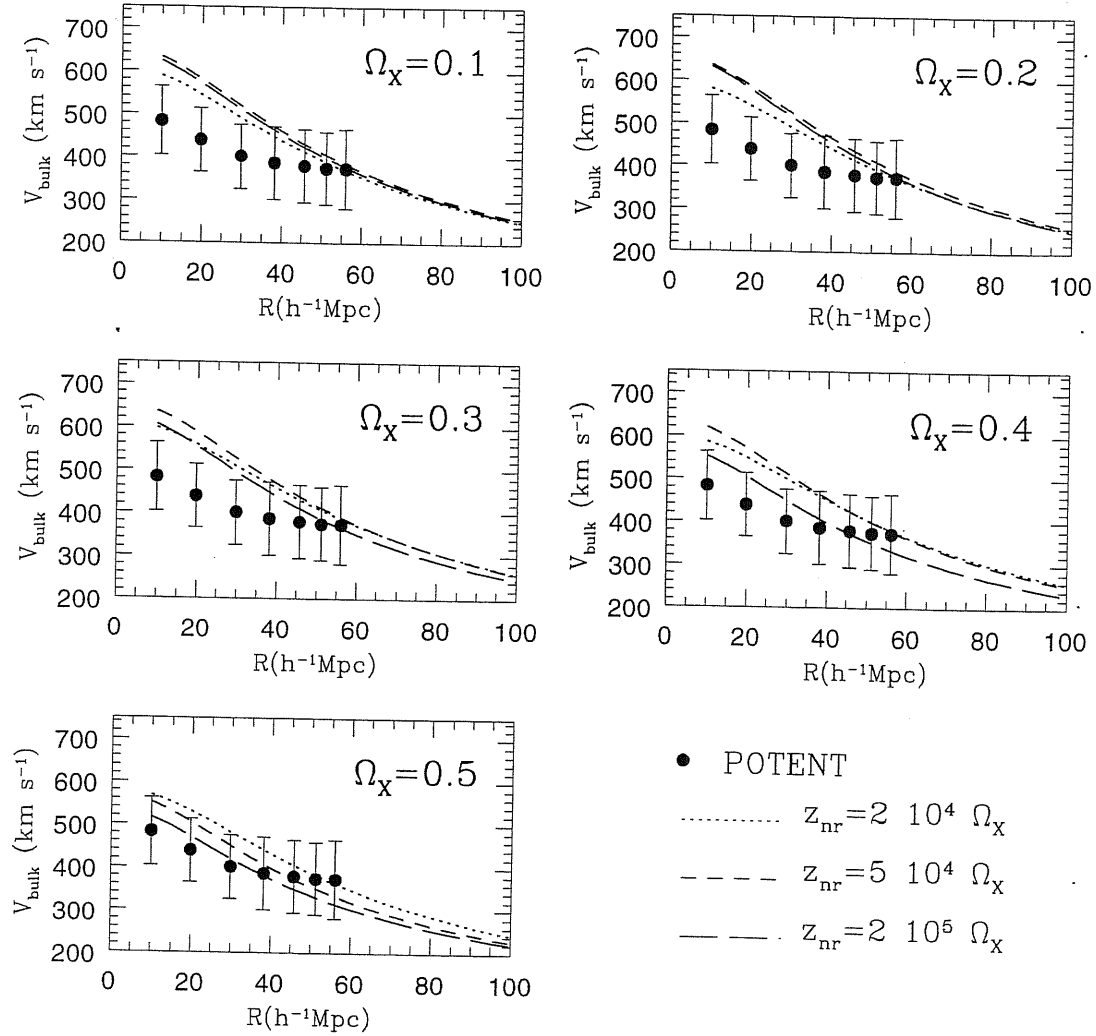


Figure 4.2: Comparison between the POTENT bulk flow (filled dots) and that provided by the CVDM models. Different panels are for different Ω_X values. In each panel, different curves refer to the different values for z_{nr} .

by now well tested against numerical simulations [142, 143]. In the following we shall use it to obtain prediction on the abundancies of Damped Ly- α systems and galaxy clusters in different cosmological models.

When a smoothing window with a given radius is applied to a gaussian random field, a smoothed density field is obtained. This field is also gaussian, provided that its dispersion is smaller than one. It is then easy to compute the fraction of space in the Universe occupied by regions where the linearly evolved smoothed density contrast exceeds some given threshold value. Press and Schechter assumed that for the correct threshold value this fraction could be identified with the fraction of matter in the Universe which is part of gravitationally bound objects with a certain minimum mass, the relation between the size of the regions and the minimum mass of the bound objects depending on the smoothing window applied to the underlying density field. The main problem of this approach is that in linear theory half of the volume of the Universe is always composed of regions with a negative smoothed density contrast, and therefore only half of the matter in the Universe is available to form bound structures (which is clearly not the case in the real Universe). This problem arises because one is not taking into account the matter in the regions whose linearly evolved density contrast does not exceed the threshold value, and thus are not considered to be bound according with the above criterion, but which are part of bigger regions whose linearly evolved density contrast does exceed the threshold value, and are therefore bound. Press and Schechter proposed a solution to this problem allowing for the matter in those regions simply by assuming they contain as much matter as the matter contained within the regions which are bound according with the original criterion. The main motivation for this assumption is that it is the simplest way of allowing all the matter of the Universe to be available to form gravitationally bound structures.

4.3.1 Cluster abundance

According to the standard Press & Schechter approach, the number density of collapsed structures arising from Gaussian initial fluctuations and having mass larger than M is given by

$$N(> M) = \int_M^\infty n(M') dM'. \quad (4.5)$$

Here $n(M) dM$ is the number density of objects with mass in the range $[M, M + dM]$ and is related to the power-spectrum according to

$$n(M) dM = \frac{1}{\sqrt{2\pi}} \frac{\delta_c}{f} \int_R^\infty \frac{\eta_R}{\sigma_R} \exp\left(-\frac{\delta_c^2}{2\sigma_R^2}\right) \frac{dR}{R^2}, \quad (4.6)$$

where

$$\eta_R = \frac{1}{2\pi^2\sigma_R^2} \int k^4 P(k) \frac{dW^2(kR)}{d(kR)} \frac{dk}{kR}. \quad (4.7)$$

In the above expressions, we assume that the mass scale M is related to the length scale R according to $M = f\bar{\rho}R^3$, with f the “form factor”, which is specified by the shape of the filter W and $\bar{\rho}$ the average density. For the Gaussian window it is $f = (2\pi)^{3/2}$, while $f = 4\pi/3$ for a top-hat window. The parameter δ_c is the critical density contrast, which represents the threshold value for a fluctuation to turn into an observable object, if evolved to the present time by linear theory. For a top-hat spherical collapse one has $\delta_c = 1.68$, but the inclusion of non-linear effects, as well as aspherical collapse, may lead to a lower value of δ_c . For example, Klypin & Rhee [144] (KR94 hereafter) found that the cluster mass function in their CHDM N-body simulations is well fit by eq.(4.6) by taking $\delta_c = 1.5$ for the Gaussian window.

4.3.2 High-redshift objects

A further constraint on power spectra comes from observations of high-redshift objects. The most reliable such constraint concerns the abundance of damped Ly- α systems (DLAS). These are observed as wide absorption troughs in quasar spectra, due to a high HI column density ($\geq 10^{20} \text{ cm}^{-2}$). The fact that at $z \sim 3$ the fractional density of HI gas associated with DLAS is comparable to that contributed by visible matter in nearby galaxies, suggests that DLAS actually trace a population of collapsed protogalactic objects (see [145] for a comprehensive review). In this context, a crucial question is to understand whether the observed Ω_g provides a fair representation of the collapsed gas fraction at a given redshift. Effects like gas consumption into stars, amplification biases due to gravitational lensing of background QSOs [146] and dust obscuration [147] could well alter final results. However, such effects are believed to play a role at low redshift ($z \sim 1-2$), while they are expected to be less relevant at the highest redshifts at which DLAS data are available. For this reason, we will consider as the most constraining datum the value of Ω_g reported by Storrie-Lombardi et al. [148] at redshift $z \simeq 4.25$ and will assume that all the HI gas at that redshift is involved in the absorbers.

Several authors recognized DLASs as a powerful test for DM models using both linear theory and numerical simulations [149, 150, 151, 152, 153, 154, 155]. The recent availability of high-resolution spectra for several DLAS systems, allowed Prochaska & Wolfe [156] to use the internal kinematics of such systems to severely constrain a CDM model.

Lanzetta et al. (1995) [157] and Wolfe et al. (1995) [158] presented data on DLAS up to the redshift $z \simeq 3.5$, while the compilation by Storrie–Lombardi et al. (1995) [148] pushed this limit to $z \simeq 4.25$. Based on these data, the latter authors claimed the first detection of a turnover in the fractional density, Ω_g , of neutral gas belonging to the absorbing systems at high redshift.

Based on a linear theory approach, several authors [151, 149, 150] concluded that the standard CHDM scenario with $\Omega_\nu = 0.3$ is not able to generate enough collapsed structures at $z \gtrsim 3$, due to the lack of power on galactic scales. However, either lowering Ω_ν to about 0.2 [152] or ‘bluering’ the primordial spectrum, $P(k) \propto k^n$ to $n \simeq 1.2$ [153] keeps CHDM into a better agreement with data. Katz et al. (1995)[159] resorted to numerical simulations of DLAS and found that even the CDM model with a normalization as low as $\sigma_8 = 0.7$ satisfies the DLAS constraint.

In order to connect model predictions from linear theory with observations, let

$$\Omega_{\text{coll}}(M, z) = \text{erfc} \left(\frac{\delta_c}{\sqrt{2}\sigma(M, z)} \right), \quad (4.8)$$

be defined as the fractional density contributed at the redshift z by collapsed structures of mass larger than M . Accordingly, it is $\Omega_g = \alpha_g \Omega_b \Omega_{\text{coll}}$, where α_g is the fraction of HI gas which is involved in the absorbers.

One expects the value of α_g , to decrease well below unity at low redshift, due to gas consumption into stars. Note that varying this number turns into a linear rescaling of Ω_g . Since we assume here that $\alpha_g = 1$, we compare data and predictions at the highest redshift allowed by the data, $z = 4.25$ [148]. We estimate $\sigma(M, z = 4.25)$ for a Gaussian window, by explicitly computing the transfer function at that redshift, so as to take into account effects of residual free-streaming of the volatile component.

As for the value of the critical density contrast δ_c , results based on N-body approaches [160, 152] suggest that $1.3 \lesssim \delta_c \lesssim 1.5$ for a Gaussian window, while other authors [150] found indications for $\delta_c \simeq 1.7$ – 1.8 for a top-hat window. In the following we will report results for $\delta_c = 1.5$ and gaussian window; while the effect of varying this parameter is discussed in more detail in ref. [153]. Lacey & Cole (1994)[143] have realized a detailed test of the Press–Schechter theory against scale-free N-body simulations, by checking the effects of varying the window and the halo identification method. As a result, they found that $\delta_c \simeq 1.3$ and $\delta_c \simeq 1.8$ are in general adequate to describe the halo mass function for Gaussian and top-hat window, respectively. In any case, we verified that rather similar results are obtained either using $\delta_c = 1.5$ with a Gaussian window, or $\delta_c = 1.7$ with a top-hat window.

4.4 Volatile models with radiative decay

4.4.1 Cluster abundance

In order to account for the rather poor knowledge of δ_c , we prefer to compute $N(> M)$ for different values of this parameter in the range $[1.4, 1.7]$.

The results of this analysis are reported in fig.4.3, where we also compare them with observational results. Values of $N(> M)$ for $\delta_c = 1.5$ are also listed in table 4.1. Following White et al. (1993) [161], we take $M = 4.2 \times 10^{14} h^{-1} M_\odot$ for the limiting mass at which to estimate the mass function. We prefer not to consider a larger value, $\sim 10^{15} h^{-1} M_\odot$, since this would correspond to the exponential tail of the cluster mass function (e.g. Bahcall & Cen 1992[162],[163]) and, as a consequence, large variations in the cluster abundance would be associated with uncertainties in the cluster mass estimates. The dashed band in fig.4.3 corresponds to the range between the observational result of White et al. ([161]; lower limit) based on X -ray data, and that of Biviano et al. ([164]; upper limit) based on velocity dispersions. We note that realistic observational uncertainties are probably larger than the difference between such two results. They may be due to systematic effects, related to assumptions used to connect X -ray temperature and DM potential profiles, or to biases in estimating cluster masses from internal velocities under the virial assumption.

Even bearing such warnings in mind, it seems difficult to reconcile with the data those models which overproduce clusters by one order of magnitude or more, for any δ_c value. This is the case for $\Omega_X = 0.1$ and, in general, for those models having a large value of z_{nr} . Even though taking the larger baryonic fraction decreases the cluster abundance, its effect is nevertheless only marginal for those models which have an exceedingly large $N(> M)$.

It is not clear whether such large discrepancies may be overcome on the ground of observational biases. For instance, let us consider the model with $\Omega_X = 0.2$, $z_{nr} = 10^4$ (model 5 in table 3.1) as a case providing a large $N(> M)$. If we allow for an underestimate of cluster masses by a factor 2 (i.e., $M = 8.4 \times 10^{14} h^{-1} M_\odot$; see, however, Evrard, Metzler & Navarro 1996[165], for arguments in favour of precise mass determinations from X -ray data) and take $\delta_c = 1.5$, it would give $N(> M) \simeq 1.2 \times 10^{-5} (h^{-1} \text{Mpc})^{-3}$, which is still quite far from the observational band.

On the other hand, we do not believe that the observational situation is clear enough to rule out at a large confidence level models which are discrepant by a factor 2–3 with respect to the reported abundances. Even adopting such a rather conservative position, it is fair to say that only models with $\Omega_X \geq 0.2$ and low z_{nr}

are not excluded by this constraint. In this respect, the availability of more and more determinations of cluster masses based on the independent technique of weak gravitational lensing (e.g. [166]) will be extremely welcome.

4.4.2 High-redshifts objects

The results of our analysis are reported in fig.4.4, where we plot the neutral gas fraction associated to DLAS, Ω_g , for all the models with $\Omega_b = 0.05$ and compare them with the observational data. In the light of all the above-mentioned uncertainties in realising such a comparison, we prefer here to adopt a conservative approach and to consider in this comparison the result of Storrie-Lombardi et al. (1995[148]; $\Omega_g = 2.2 \pm 0.5$ at $z = 4.25$ for $\Omega_0 = 1$ and $h = 0.5$) as a lower bound. Consistently, the dashed areas in fig.4.4 are delimited by the above 1σ lower limit. Only model falling below this limit are ruled out. The effect of varying the limiting mass of the protogalaxy hosting DLAS by an order of magnitude may be judged by comparing open and filled dots, which correspond to $M = 5 \times 10^9 h^{-1} M_\odot$ and $M = 5 \times 10^{10} h^{-1} M_\odot$, respectively. Numerical values of Ω_g for all the models are reported in column 5 of Table 4.1, where also results for CDM and CHDM are given.

As expected, taking lower Ω_X and larger z_{nr} make easier the agreement with data. All the models with $\Omega_X \leq 0.2$ are able to pass the DLAS test, while larger volatile fractional densities are only allowed for large z_{nr} , which however turns into a wrong power-spectrum shape.

Although several models can clearly be ruled out already at this level on the ground of DLAS data, nevertheless it is clear that more precise conclusions can only be reached with a better knowledge of the variables entering in the Press-Schechter prediction for Ω_g (i.e. the mass M , and the parameters δ_c and α_g). A more accurate definition of what is a DLAS in a given DM model can only be achieved with numerical simulations involving hydrodynamics ([159]), which would be able to trace the history of galaxy formation. As for observations, the possibility that systematic biases may affect the final results have been recently suggested. For instance, Bartelmann & Loeb (1996) [146] have pointed out that amplification biases due to gravitational lensing of QSOs by DLAS could lead to an overestimate of Ω_g , by an amount which however decreases with redshift. Fall & Pei (1996)[147] argued that dust obscuration may act in the opposite direction so as to bias downwards the estimated Ω_g . Verifying the actual relevance of such effects surely requires a substantial investment of observational and theoretical effort.

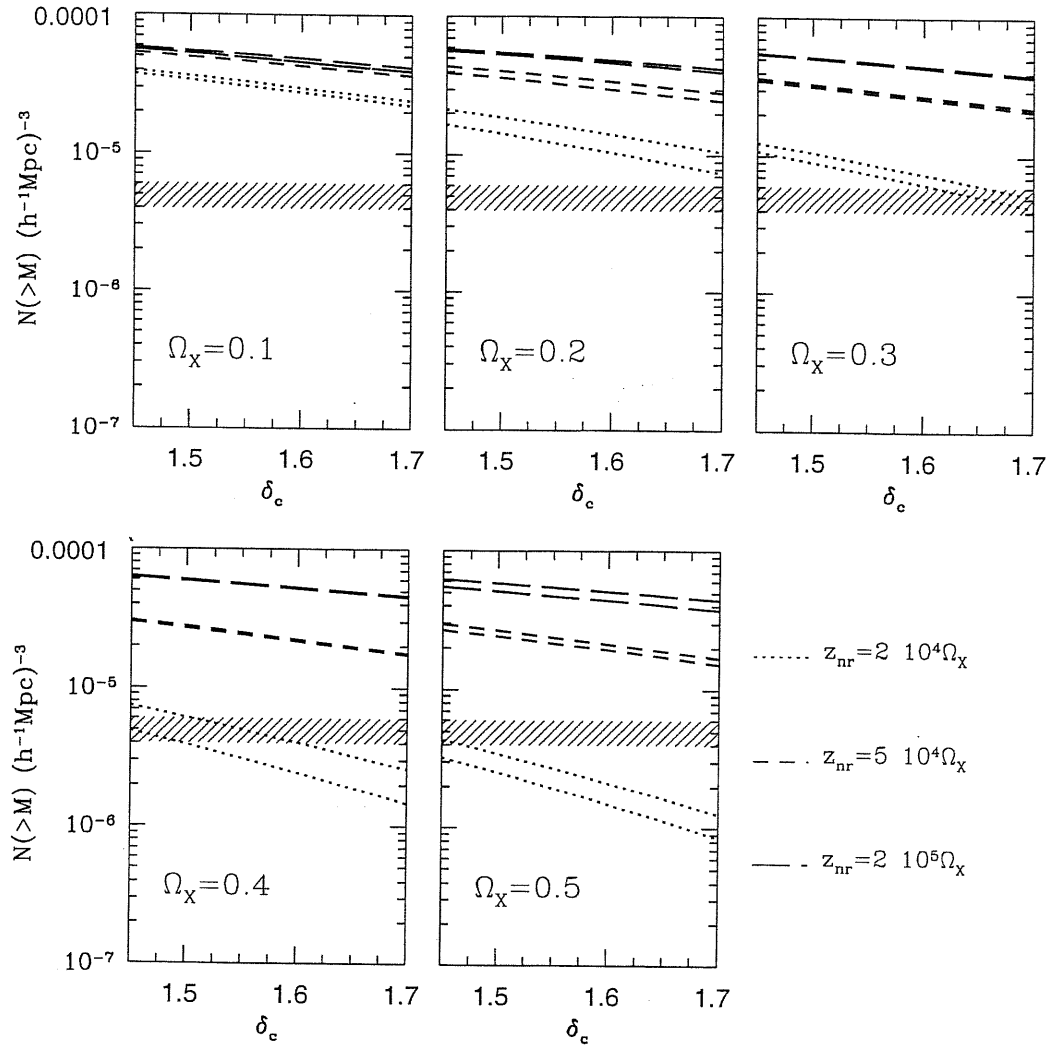


Figure 4.3: The abundance of galaxy clusters with $M > 4.2 \times 10^{14} h^{-1} M_{\odot}$. The shaded area is delimited by the observational results by Biviano et al. (1993; upper limit) and by White et al. (1993; lower limit). In each panel, corresponding to different Ω_x values, dotted, short-dashed and long-dashed curves are for the three different values of z_{nr} . Each pair of curves correspond to the two values of Ω_b , the lower one being for $\Omega_b = 0.08$ and the higher one for $\Omega_b = 0.05$.

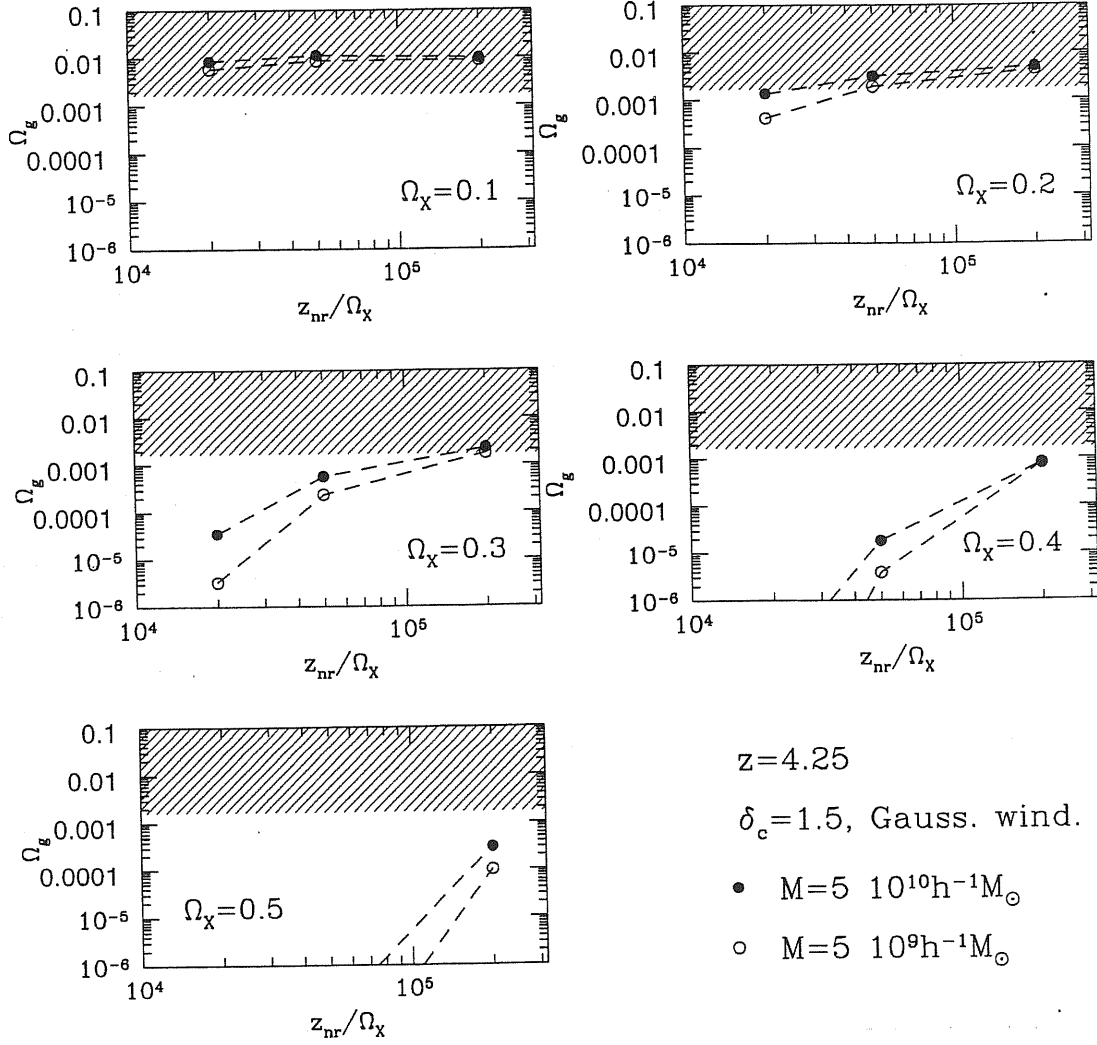


Figure 4.4: The fractional density of neutral gas involved in DLAS at redshift $z = 4.25$. The shaded area is the observational constraint and is delimited from below by the 1σ lower limit by Storrie-Lombardi et al. (1995). Each panel refers to a fixed Ω_x value and reports the predicted Ω_g as a function of z_{nr} . Filled and open dots correspond to $M = 5 \times 10^9 h^{-1} M_\odot$ and $M = 5 \times 10^{10} h^{-1} M_\odot$ for the limiting mass of the protostructures hosting DLAS. We assume a Gaussian window with $\delta_c = 1.5$ and $\alpha_g = 1$ for the HI gas fraction involved in the absorber.

4.5 Volatile particles with non-radiative decay

In analyzing these models, we performed a selection based on both LSS and CMB observations. More in detail, we considered the following prescriptions: (i) We set the numerical constant A , in the power spectrum, so that C_2 is consistent with COBE 3σ intervals for $Q_{rms,PS}$ (for different n 's).

(ii) Once the normalization is fixed at small k , we test the large k behaviour, first of all on the $8h^{-1}\text{Mpc}$ scale. The mass M_λ , within a sphere of radius $L = \lambda h^{-1}\text{Mpc}$, is $M_\lambda = 5.96 \cdot 10^{14} \Omega h^2 M_\odot (\lambda/8)^3$. Therefore, the cumulative cluster density $n(> M) = \sqrt{2/\pi} (\rho/M) \int_{\delta_c/\sigma_M}^\infty du [M/M(u)] \exp(-u^2/2)$ for $M = 4.2h^{-1} \cdot 10^{14} M_\odot$ is directly related to the value of σ_8 . We take $M(u)$ defined so that the mass variance (evaluated with a top-hat window function) satisfies the relation $\sigma_{M(u)} = \delta_c/u$.

Let us then consider $N_{cl} = n(> M)(100h^{-1}\text{Mpc})^3$ for the above M value. Optical and X-ray observations give a value of N_{cl} which is still not so different from ~ 4 , as found by White et al. (1993) and Biviano et al. (1993). Both the observational value and its theoretical prediction are however subject to a number of uncertainties. For instance, observations have some problems to fix cluster masses. From the theoretical side, non-linearity effects and mechanism turning fluctuations into clusters cannot be said to be completely under control. It is also wise recalling that N_{cl} and σ_8 feel the slope of the spectrum, around $8h^{-1}\text{Mpc}$, in a slightly different way. Henceforth, we shall further comment on σ_8 values, after discussing the spectral slope.

The above arguments tell us that, in our systematic search, it is wise to keep models with $1 \lesssim N_{cl} \lesssim 10$.

(iii) Models that could survive the previous test were then used to evaluate the expected density parameters Ω_g . More specifically, using such expression, we evaluated $DLAS \equiv \Omega_{gas} \times 10^3/\alpha$, taking $z = 4.25$, $\delta_c = 1.69$ and $M = 5 \cdot 10^9 h^{-1} M_\odot$. According to Storrie-Lombardi 3σ lower limit, we passed models only when $DLAS > 0.5$.

(iv) As long as Γ is concerned, we kept 0.27 as top acceptable value, which is both the upper limit given for APM and the $\sim 3\sigma$ upper limit for Abell/ACO. Owing to previous considerations, we took 0.13 as lower limit, assuming that an underestimate of non-linear effects by $\sim 6-8\%$ cannot be excluded.

4.5.1 Relations between different constraints

As already mentioned, the constraint on Γ , together with a suitable constraint on σ_8 , implies a constraint on N_{cl} . Checks of σ_8 , N_{cl} and Γ are, therefore, strictly related.

For instance, an observational value for σ_8 can be deduced from X-ray data on the gas temperature T_g in galaxy clusters. If clusters are substantially virialized and the intracluster gas is isothermal, the mass M of a cluster can be obtained once the ratio

$$\beta = \frac{\text{galaxy kinetic energy/mass}}{\text{gas thermal energy/mass}}$$

is known; then, the temperature function can be converted into a mass function, which can be fit to a Press & Schechter expression, yielding the normalization of $\sigma(M)$ (variance as a function of the mass scale M) and hence σ_8 .

An alternative possibility, of course, amounts to deducing masses from galaxy velocities obtained from optical data. Both pattern imply some problem.

The value of β is currently obtained from numerical models. Henry & Arnaud (1991)[168], assuming $\beta = 1.2$, estimated $\sigma_8 = 0.59 \pm 0.02$ from a complete X-ray flux-limited sample of 25 clusters they compiled. Various authors followed analogous patterns (see, e.g., White et al. 1993[161], Viana & Liddle 1996[169]). Eke et al. (1996)[170], adding observational uncertainties and β error, claimed that $\sigma_8 = 0.50 \pm 0.04$. An essential issue to obtain such result is that Navarro et al. (1995)[171] simulations allow to take $\beta = 1$ with an error $\lesssim 6\%$.

However, there seems to be a conflict between expected galaxy velocities, obtained assuming $\beta = 1 \pm 0.06$ and optical data. In fact, the latter give a virial velocity dispersion in clusters $\sigma_v \simeq 800$ km/s, a value consistent with $\beta \gtrsim 1.5$ ([172],[173]).

It is possible that the critical assumption is that clusters are isothermal. In many clusters, cooling flows may play an important role and a fit to a cooling-flow cluster with a simple isothermal model may yield a mean emission-weighted temperature significantly reduced in respect to the virial value (see, e.g., Allen & Fabian 1998[174]). However, according to Eke et al. (1998[175]), cooling flows would cause a z -trend in disagreement with available data. More data on high- z clusters are however needed to strengthen this statement. Other authors (Frenk et al. 1990[176], Borgani et al. 1997[134]) claimed that the conflict between predicted and observed σ_v originates from contamination of optical data by groups accreting onto the clusters.

4.6 Constraining volatile models

4.6.1 Volatile particles with radiative decay

The results we have presented demonstrate that the CVDM hypothesis yields potentially interesting models of structure formation. We have shown that rather slight changes in the parameters of volatile dark matter can make a significant difference to the transferred power spectrum. This contrasts with the case of a cold component, where the physical properties of the candidate particle do not really matter at all, in that the physical origin of the hot particles may leave a detectable imprint in the clustering pattern. In this context it is important to verify up to which point the shape of the distribution function causes differences compared to the standard scenario based on relic thermal neutrinos.

The ability to change z_{nr} almost independently of Ω_X is especially significant in this respect: the power spectra we have obtained display considerable variations at a fixed value of Ω_X . Indeed, although the CVDM class of models involves one more parameter than is the case for CHDM, we have shown that observational data nevertheless allow us to put rather stringent constraints on the permitted values of z_{nr} and Ω_X , even at the level of linear-theory. The most stringent of these constraints comes from the simultaneous requirement for a model to satisfy the observed abundance of high-redshift DLAS and of galaxy clusters. As for DLAS, the rather large value of the HI gas fraction involved in the absorbing systems, Ω_g , implies a substantial amount of power on galaxy scales, so as to favour models with $\Omega_X \lesssim 0.2$. A larger volatile component would be allowed only resorting to a high value of $z_{nr} \simeq 2 \times 10^5 \Omega_X$ (cf. fig.4.4). On the other hand, models with small Ω_X and/or large z_{nr} behave too much like the standard CDM model, drastically overproducing clusters (cf. fig.4.3).

Therefore, the overall result would be that models with $z_{nr} \gtrsim 5 \times 10^4 \Omega_X$ have a hard time, quite independently of Ω_X . Among the models inspected, the only model which passes all the tests, or at least which can not be confidently ruled out, is the one with $\Omega_X = 0.2$ and $z_{nr} = 4 \times 10^3$. It is worth recalling, however, that such a model with low z_{nr} requires that volatile particles occupy at least 5 helicity states [cf. eq.(3.9)]. We recall that this can be accommodated only if (a) $g^* = 7$ is allowed by standard nucleosynthesis and (b) two neutrino species are sufficiently massive that they have already decayed at the nucleosynthesis epoch.

An alternative possibility, holding if the physics of the decay is quite different from the axino model suggested in [76], is that the decay itself takes place after the

nucleosynthesis epoch. This would make low z_{nr} models compatible with all N_ν . It must, however, be remembered that changing N_ν itself causes an alteration of the transfer function, and a straightforward extrapolation of the above results to greater N_ν values is not allowed. Changing the relation between N_ν and z_{nr} opens the way to inspecting different models and, in this context, we should also bear in mind that our analysis has been based on assuming a scale-free primordial spectrum, while variations around this model are allowed by some classes of inflationary schemes. For instance, taking $P(k) \propto k^n$ with $n < 1$ [177, 178] decreases the amount of power on the cluster mass scale, so as to alleviate the problem of cluster overproduction displayed by “colder” models. However, the amount of this tilt can not be too large, in order not to conflict with CMB [179] and large-scale peculiar motions constraints [180]. On the other hand, the case of “antitilting”, with $n \simeq 1.2$, has been recently advocated to alleviate some of the problems of the CHDM scenario [181, 182]. However, the subsequent increase of power on small scales goes in the undesired direction as far as the cluster abundance is concerned [183, 153].

As a final remark, we should remind that the analysis presented here is only preliminary and is entirely based on linear calculations. In order to be more definitive on we would like to study the non-linear evolution of some of these model by performing numerical calculations using N-body and other procedures.

4.6.2 Volatile models with non-radiative decay

While in the previous case we always kept $n = 1$, here we allowed $1 \leq n \leq 1.4$, according with COBE predictions. We resume the criteria we chose in selecting the models. Firstly, we normalized the spectrum so that C_2 is consistent with COBE 3σ intervals for $Q_{rms,PS}$. Then, we kept models with whose prediction on the cluster abundance satisfied $1 \leq N_{cl} \leq 10$. We then considered the Damped Ly- α systems (DLAS). According to [148], observations give $DLAS = 2.2 \pm 0.6$. Therefore, we passed models only when $DLAS > 0.5$. It must be outlined that varying this limit by a factor ~ 2 would cause only marginal changes for models accepted. Slight shifts of Ω_h or d usually cause significant variation of $DLAS$ and this constraint turns out to be a fairly substantial one. Bulk velocities were also evaluated and compared with POTENT reconstructions of velocity fields. They cause no constraint at the 2σ level.

As long as Γ is concerned, we kept 0.27 as top acceptable value, which is both the upper limit given for APM and the $\sim 3\sigma$ upper limit for Abell/ACO. On the contrary we took 0.13 as lower limit, assuming that an underestimate of non-linear

effects by $\sim 6-8\%$ cannot be excluded.

Considering the mass variance within $8h^{-1}\text{Mpc}$, we considered that models with σ_8 in an interval 0.45–0.75 should be viable. As expected, models passing previous tests keep comfortably inside such interval. The top σ_8 needed by models in fig. 4.6 is 0.70 (for $\Omega_h = 0.26$, $d = 1$, $n = 1.2$) and the bottom σ_8 is 0.50 (for $\Omega_h = 0.18$, $d = 16$, $n = 1.2$). If the constraint on Γ is dropped (fig. 4.5), just two models with $\sigma_8 = 0.70$ (both yielding $\Gamma < 0.10$) and a model with $\sigma_8 = 0.48$ ($\Omega_h = 0.22$, $d = 16$, $n = 1.3$, $\Gamma = 0.11$) are added.

Some of the transferred spectra are plotted in figs. 3.6 – 3.9, together with spectral data obtained from Las Campanas survey (LCRS) [110], kindly provided by Lin. It is however worth outlining soon that such comparison, although suggestive, is not so discriminatory.

A detailed description of LCRS is given by [184]. The survey encloses 3+3 “slices” $1^\circ.5 \times 80^\circ$ wide, in the northern and southern emispheres. Data were taken using two multifiber systems. Fields $1^\circ.5 \times 1^\circ.5$ wide were inspected above suitable photometric limits, chosen so that there were more galaxies per field than available fibers. Then, target galaxies in each field were randomly selected and a “field sampling factor” f was memorized, to be used in any further statistical analysis. The average values of f are different for the two multifiber systems, which are able to inspect 50 and 112 objects, and amount to 0.58 and 0.70, respectively. The nominal photometric limits are also different for the two systems, amounting to $16 \leq m \leq 17.3$ and $15 \leq m \leq 17.7$, respectively. A further geometric effect is due to the impossibility to inspect galaxies, in a given field, if nearer than $55''$.

The actual situation for power spectrum measurement from LCRS appears to fall into two regimes. On scales $L < 80-100 h^{-1}\text{Mpc}$ ($k > 0.2 h$) a fair determination of the spectrum is obtained. In this range, LCRS results strengthen results from other surveys. Larger scales would be more discriminatory, but here errors are greater and the sample variance might cause further shifts.

When compared with such observational spectra, a reasonable transferred spectrum should lie *below* observational errorbars, up to $\sim 80-100 h^{-1}\text{Mpc}$; the gap between theoretical and observational spectra is related to the amount of *bias* (constant gap means a scale-independent bias level). For k values much beyond this scale, requiring a detailed fit may be excessive. Although there are mixed models which provide it, we see no reason to disregard models whose spectrum falls within $\sim 3\sigma$ errorbars from the reconstructed spectrum. An example of such models are ΛCDM models, with various Λ contents, which were shown also by [110], but not

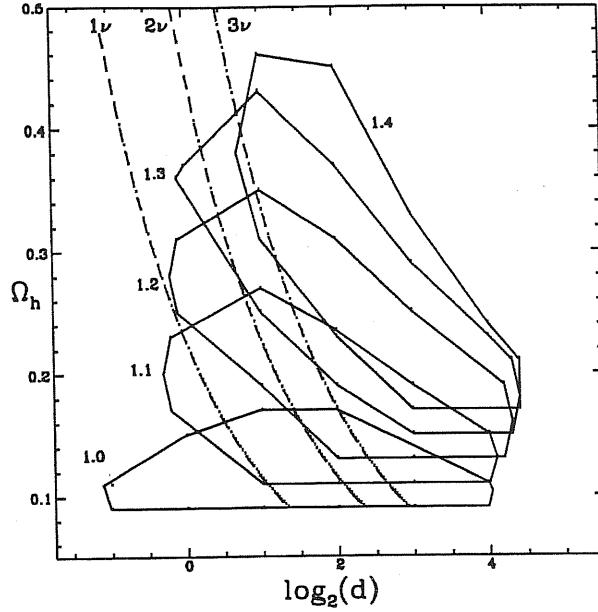


Figure 4.5: The curves enclose areas where models predict LSS linear features consistent with observations. Each curve refers to the value of n written aside. Point-dashed lines refer to models with HDM made of massive ν 's. Restrictions can be applied to the latter models only after addition of a suitable amount of SMLC. See the text for a more detailed comparison of the LSS they predict with volatile models. The constraints taken into account are: cluster abundance, σ_8 value, gas in damped Ly- α systems.

treated here.

Results on parameter constraints are summarized in figs.4.5 – 4.6. As was already known, a number of such models with Ω_h up to 0.30 pass the above tests. If $n = 1$, volatile models allow little extra freedom, namely for high z_{der} . The situation is already different for $n \simeq 1.1$. Here models with $z_{der} \simeq 600$ are allowed for Ω_h up to 0.14 and greater Ω_h are allowed for values of z_{der} still much lower than those allowed by neutrino models. The range of Ω_h values allowed with $z_{der} \simeq 600$ extends upwards as n increases and overcomes 0.20 for $n = 1.4$. The greatest value found for Ω_h is 0.30 for $z_{der} = 10^4$ with $n = 1.2$. Thermal models with 2 or 3 massive neutrinos and a suitably added SMLC arrive to $\Omega_h \simeq 0.28$, for $n = 1.2$ and $n = 1.3$, respectively.

These values may not seem too large, in respect to Ω_h values currently used in the literature (with thermal models). It must be outlined, however, that our acceptance criteria are more stringent than usual. With such criteria, no thermal model with $\Omega_h > 0.16$ is accepted for $n \leq 1$.

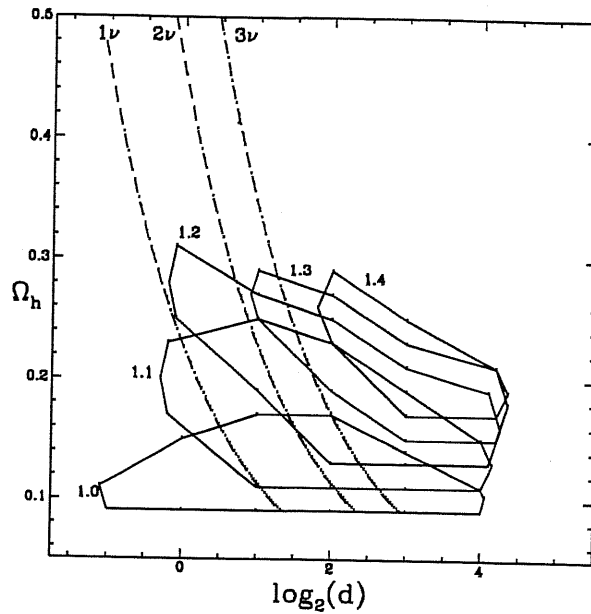


Figure 4.6: As in fig.4.5, but here the value of the extra-power parameter Γ is also constrained.

Let us also draw the attention on the very low values of z_{der} that volatile models with large n allow. As an example of low z_{der} , in fig. 3.8 we show the transferred spectrum of a model with 22 % of HDM and $z_{der} = 625$, which, for a fairly high value of COBE quadrupole, has excellent fits with all linear constraints. HDM particles of this and similar models have a mean square velocity ~ 500 km/s today, still away from potential wells. Such speed is likely to guarantee them not to cluster with baryon or CDM on any scale. Dynamical mass estimates, in a world containing such component, might lead to observe ~ 75 – 80 % of critical density.

It should be also mentioned that, if the constraint on Γ is dropped, greater Ω_h 's seem allowed (see fig. 4.5). The top value we found is $\Omega_h = 0.45$ with $z_{der} \simeq 5000$. With 3 or 2 massive neutrinos the highest Ω_h obtainable are 0.40 and 0.38, respectively. As already outlined, in figs. 4.5 – 4.6 neutrino model curves are overlapped to volatile model parameter space, but the allowed regions apply to them only after adding suitable SMLC.

Other authors [185], in a paper focused on $n \leq 1$ models, mentioned that a model with $\Omega_h = 0.35$, $n = 1.2$, $h = 0.4$ agreed with the linear constraints they imposed. Using our linear constraints, Ω_h is to be lowered to ~ 0.30 . Volatile models do not need to lower h so far, to agree with data, as they naturally have SMLC, which induces fairly similar effects. Also thermal models can agree with data keeping to

$h = 0.5$, rising n , with or without extra SMLC. Figs.3.10 – 3.12 illustrate some spectra for such models.

Models with high HDM content and high average kinetic energy, could also ease the problem of the apparent baryon excess in several galaxy clusters. It has been known for several years ([186, 187, 188, 161]) that the baryon mass fraction in galaxy clusters is high, in respect to expectations in flat, pure CDM models. According to [161], even neglecting baryons in galaxies, the *observed* baryon fraction yields

$$\Omega_b h^{3/2} = 0.05 \pm 0.02 \quad (4.9)$$

for flat, pure CDM models. BBN limits of [189] required then that $\Omega_b h^2 = 0.0125 \pm 0.0025$.

Much work was then performed to analyze individual clusters and lists of baryon contents in cluster samples were presented by several authors [190]. The situation is summarized in a recent paper by [191] who obtains the constraint

$$\Omega_b h^{3/2} = 0.060 \pm 0.003 \quad (4.10)$$

This is to be taken with recent BBN limits on Ω_b . *E.g.*, [192] give $0.007 < \Omega_b h^2 < 0.024$ and therefore $\Omega_b \simeq 0.1$ with $h = 0.5$ is marginally allowed. For $h = 0.5$, as we assumed here, eq.(4.10) gives a central value $\Omega_b = 0.17$ and a 3σ minimum $\Omega_b \simeq 0.14$.

If HDM does not cluster with CDM and baryons, a measure of Ω_b would however yield $\Omega_{b,app} = \Omega_b / (1 - \Omega_h)$. Within mixed models, therefore, agreement with data requires $\Omega_h > 0.41$ or > 0.29 , respectively. We have shown in this work that the latter value is coherent with LSS constraints, if $1.2 \leq n \leq 1.4$; as n increases, compatible models have z_{der} values decreasing, down to ~ 2500 .

Limits become more permissive if masses obtained from lensing are replaced to those obtained from X-ray data (see, e.g., [174]). High baryon density, however, seems a widespread feature. Perhaps the limits shown in eq.(4.10) are to be reset, taking greater cluster masses, but, if $\Omega_o = 1$, there seems to be a definite evidence of a component which tends not to cluster with CDM. The debate is related to the discussion on σ_8 limits in section 4.5.1.

In the literature, mixed models with $n \leq 1$ were often considered and allow to predict acceptable values of a number of observable quantities, if low rates for the HDM component are taken. Considering $n > 1$ is at least as legitimate as taking $n < 1$ and leads to a range of mixed models allowing fair predictions on the same quantities. We showed that models with $n > 1$ require and allow higher HDM

contents. They could therefore improve our understanding of why Ω_o measures seem to give increasing values when greater scales are considered. This was one of the basic motivations to introduce mixed models, more than a decade ago.

4.6.3 Volatile models compared to CMB experiments

In this section we give the CBR spectra of the hot-volatile models and compare them with available data, ranging from $l = 2$ to $l \lesssim 500$.

We evaluated the spectra for several parameter choices allowed by LSS constraints (see figs. 4.5 – 4.6). Significant example of C_l spectra are shown in figs. 4.7 – 4.11 while the corresponding LSS

predictions are summarized in table 4.2.

Some parameter sets are compatible with neutrino hot dark matter, while models with a low z_{der} and $n \gtrsim 1$ are obtainable with volatile hot dark matter. Since the height of the first doppler peak is very sensitive to the baryon abundance, we considered two values of Ω_b , namely 0.05 and 0.1. Spectra are normalized to $Q_{rms,PS}$ assuming no contribution of gravitational waves. As is known, their contribution would raise the low- l tail of the C_l spectrum, therefore reducing the gap between the Sacks-Wolfe *plateau* and the top of the first doppler peak.

Models with $\Omega_b = 0.1$ systematically show a peak less pronounced than models with $\Omega_b = 0.05$. It is well known that models with a given h and hot component show a lower doppler peak for smaller Ω_b ; in top of that, here there is a further effect: LSS constraints often are compatible with a part of the observational $Q_{rms,PS}$ interval, and low Ω_b models tend to be consistent with low $Q_{rms,PS}$ values.

In figs. 4.7 – 4.11 we compare models with data from COBE [193] Saskatoon [128] and CAT [130] experiments only.

Figs. 4.7 – 4.11 show a systematic trend: for a given large l value, C_l increases with both n and $d = 10^4/z_{der}$. On the contrary, for a given large k value, the matter fluctuation spectrum $P(k)$ increases with n but is damped for large d , so that these two effects tend to compensate.

This is one of the reasons why LSS constraints can be compatible with n as high as 1.4. On the contrary, figs. 4.11 show that CBR spectra already disfavour $n = 1.3$ if $d \gtrsim 4$ ($z_{der} \lesssim 2500$) is considered, no matter the value of Ω_b . Volatile models with $n > 1.2$ are largely out of the errorbars, and should be considered as scarcely viable. Nevertheless, even for $n = 1.2$, volatile models allow a higher first doppler peak without raising the following ones, and therefore fit the data better than neutrino models, if no reionization is assumed. Just as large n , also large d causes conflict

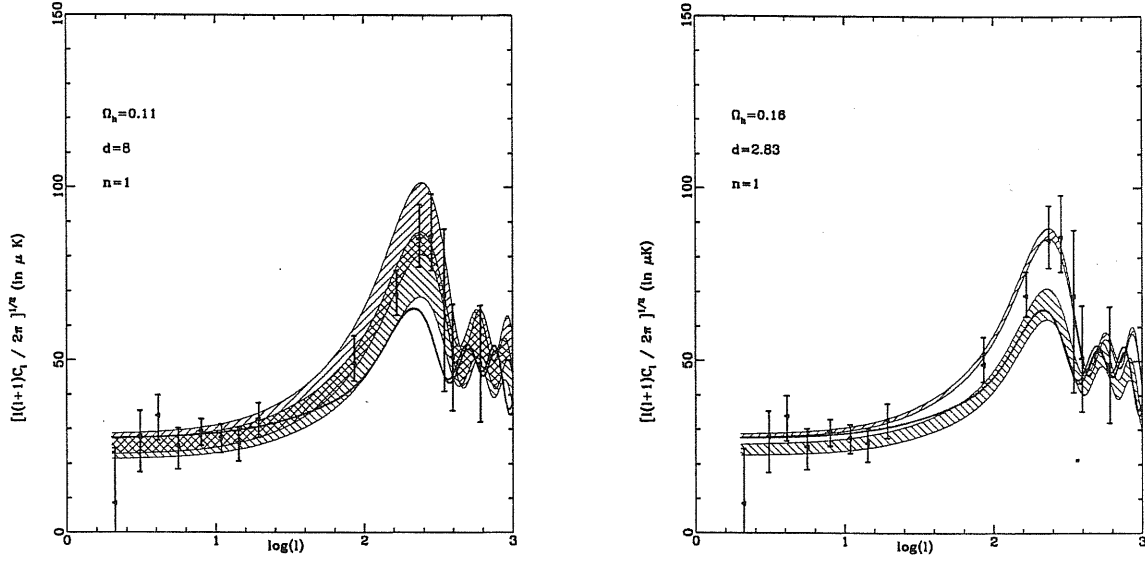


Figure 4.7: volatile spectra are compared with the observational data from COBE, Saskatoon and CAT experiments. The errorbars correspond to 1σ errors. Solid bold lines refer to standard CDM ($h = 0.5$, $n = 1$, $\Omega = 1$) and a neutrino model with $\Omega_h = 0.3$. Shaded areas are the volatile spectra with parameters specified in the figure. Upward shading refers to $\Omega = 0.1$ models while downward shading to $\Omega = 0.05$. Notice that $z_{der} = 10^4/d = 1250$ (left panel) and $z_{der} = 3533$ (right panel).

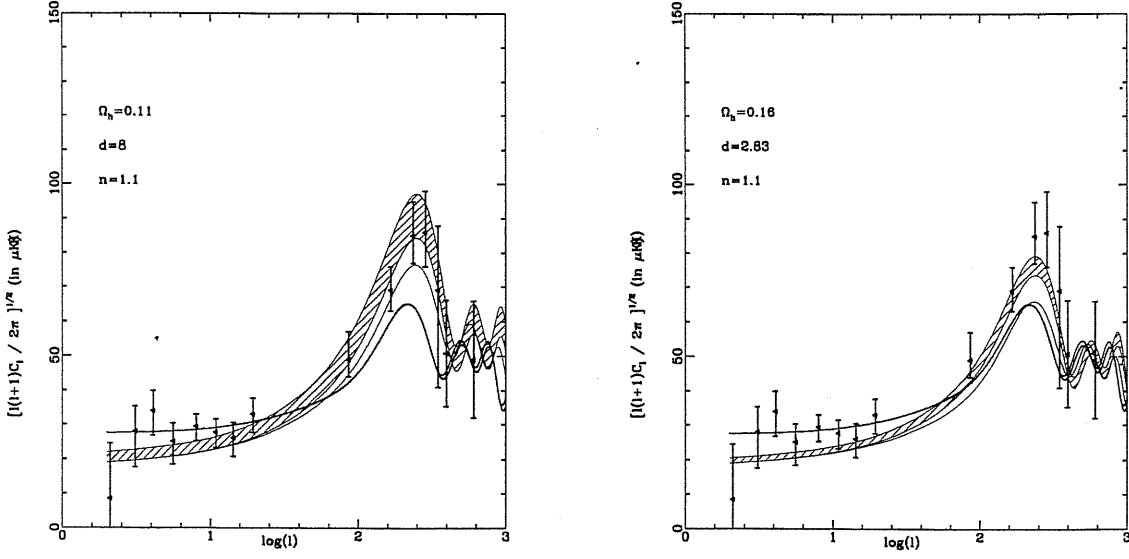


Figure 4.8: volatile spectra compared to the data. $z_{der} = 1250$ (left panel) and $z_{der} = 3533$ (right panel).

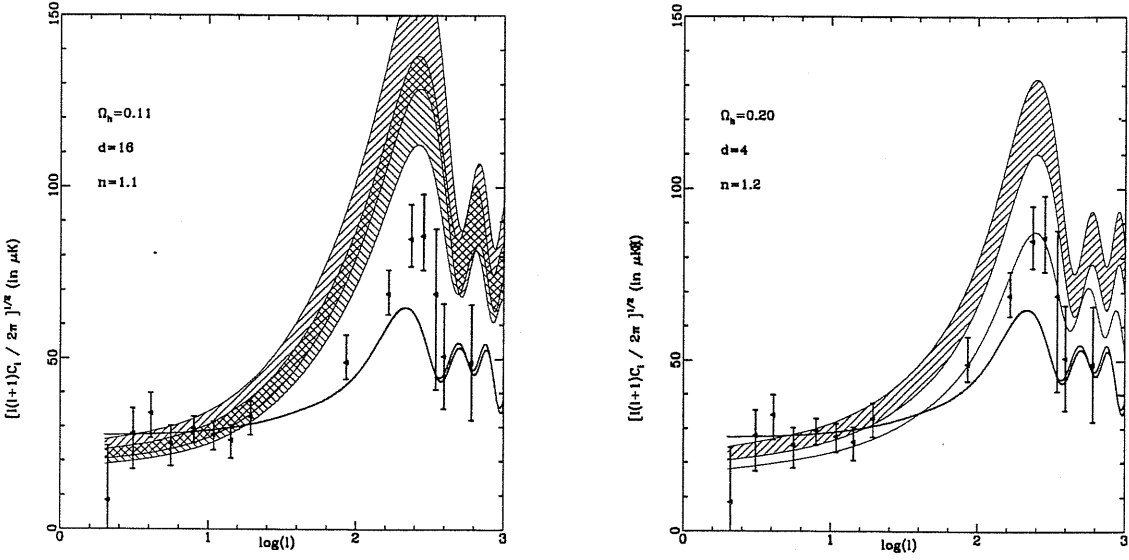


Figure 4.9: volatile spectra compared to the data. $z_{der} = 625$ (left panel) and $z_{der} = 2500$ (right panel).

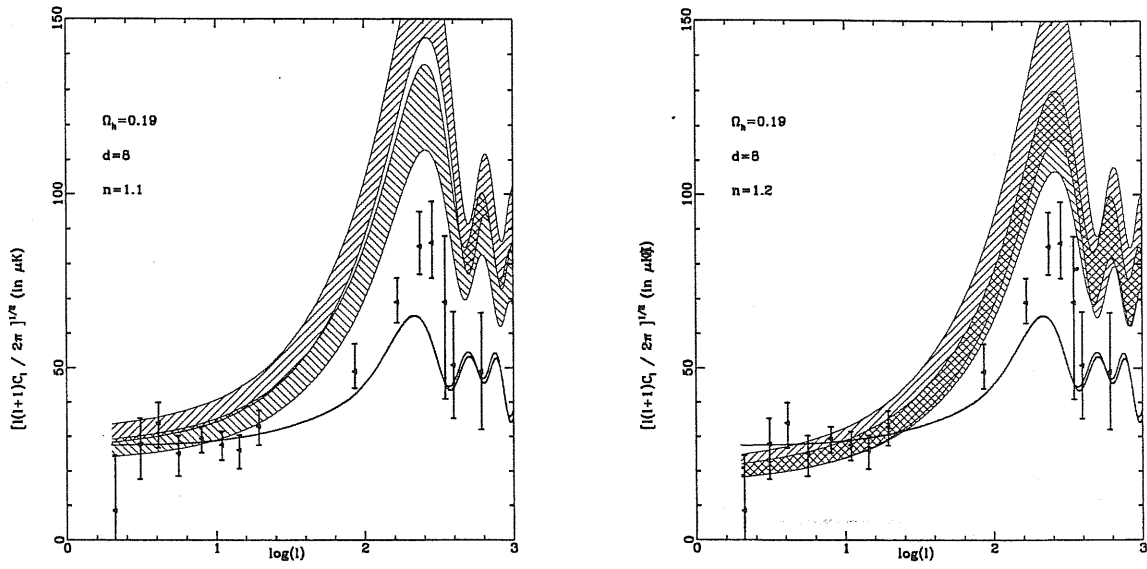


Figure 4.10: volatile spectra compared to the data. $z_{der} = 1250$ (left panel) and $z_{der} = 1250$ (right panel).

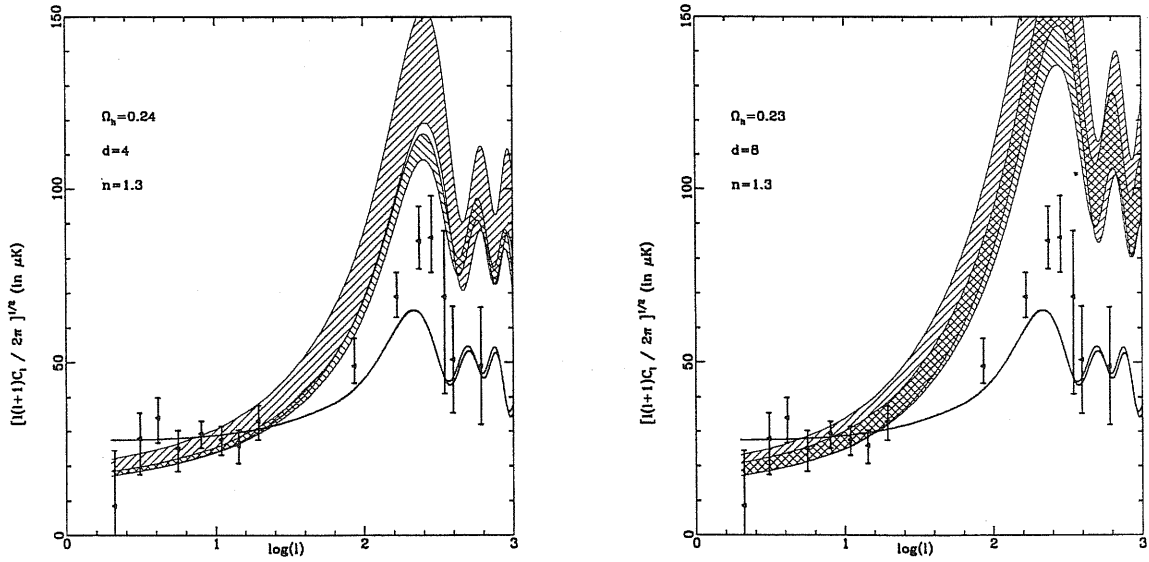


Figure 4.11: volatile spectra compared to the data. $z_{der} = 2500$ (left panel) and $z_{der} = 1250$ (right panel).

with data, by itself. For example, fig. 4.9 (left panel) show that models with $d = 16$ are disfavoured, even with low Ω_h and $n = 1.1$.

As pointed out in Chapter 1, volatile models require a sterile component whose energy density is proportional to $\Omega_h d$. Its effective number of degrees of freedom is linked to the equivalence redshift, which in turn affects both the shape parameter Γ and the height of the first doppler peak. Dodelson et al. (1994) [119] considered the matter power spectrum in the case of a τ -neutrino decay (τ CDM model), and found that even in that case the effective number of degrees of freedom $g_{\nu,eff}$ is bigger than in standard CDM. They outlined that, in order to lower Γ at least down to 0.3 [133], in a $h = 0.5$ universe with $n = 1$, an equivalent number of massless neutrinos ($N_{\nu,eff} \equiv g_{\nu,eff}/2$) as high as 16 is needed. Other authors [125], who also consider τ CDM models but with a lighter neutrino, also pointed out that the predicted Γ of these models is lower due to the high $g_{\nu,eff}$, and show that a lower Γ implies a higher first doppler peak. Their work, however, is only qualitative, and they don't infer any restriction in the parameter space using the data. Looking at the data, we found out that if $n = 1.1$, CBR data models with an equivalent number of neutrino species $N_{\nu,eff} \gtrsim 10$ as in figs. 4.9 (left panel), 4.10 (left panel) and 4.11 (right panel) are disfavoured. Models like the one shown in fig. 4.8 (left panel, $N_{\nu,eff} \simeq 7$) seem to better fit the data, although even lower $N_{\nu,eff}$ ($\simeq 5$), as provided by the model in fig. 4.8 (right panel), should not be disregarded.

Keeping to $n = 1$, LSS already exclude very high $\Omega_h d$ values, so that a low $N_{\nu,eff}$ is automatically ensured. The models shown in figs. 4.7 seem to well fit the data, with a corresponding $N_{\nu,eff} = 5 - 7$.

4.6.4 Summary on volatile models

Let us summarize, in the end, the conclusions on volatile models.

We have analyzed mixed models from the point of view of both LSS and CMB predictions. We considered different hot dark matter components: the standard neutrino case and the volatile case in which particles come from the decay of heavier ones.

First we tested the mixed models on available LSS data requiring fair predictions for σ_8 , Γ , DLAS and N_{cl} . This analysis shows that it must be $\Omega_h \lesssim 0.3$. This comes as no surprise, as mixed models with greater Ω_h have not been considered since long. The new result is that taking n up to 1.4 does not ease the problems previously found for large Ω_h .

On the contrary, volatile models together with $n > 1$ significantly widen the

parameter space in the low z_{der} direction and viable models even with $z_{der} \sim 600$ can be found. In fact, as far as $P(k)$ is concerned, we found a nearly degenerate behaviour of the parameters n and z_{der} , as the damping on the high k values due to low z_{der} can be compensated by high n .

CBR data, apparently, break the degeneracy. In section 4.6.3 we have shown that the CBR spectrum of volatile models is significantly different from standard CDM and also from neutrino models usually considered. In fact SMLC and late z_{der} volatiles cause a late z_{eq} and, henceforth, a higher first doppler peak. Minor effects are caused by the typical momentum distribution of volatiles. These effects amounts to 2 % at most in the C_l spectrum and only an accurate analysis of the results of future satellites, as MAP and Planck, could allow to detect it.

CBR spectra of volatile models were then compared with available data from different experiments, namely those from COBE, Saskatoon and CAT experiments. Data on CBR spectrum at large l imply that temperature fluctuations $\Delta T/T \sim 10^{-5}/l$ are appreciated. Therefore, measures of the CBR spectrum, for high l values, still need to be treated with some reserve. It seems however clear that recent observations tend to indicate a doppler peak higher than expected both for pure CDM and for mixed models with early derelativization, such as most neutrino models. Taking $n > 1$ and/or late derelativization raises the doppler peak and affects the CBR spectrum at high l . The first question we tried to answer is how far we can and have to go from pure CDM and $n = 1$ to meet current large l data.

We found that volatile models could cure this discrepancy, while ensuring a viable scenario for structure formation.

In turn, large l data imply restrictions in the parameter space, complementary to the ones derived from LSS while a fit of such data requires only a slight departure from pure CDM and $n = 1$. For example, figs. 4.8 show the C_l behaviour for $n = 1.1$ and HDM ranging from 11 % to 16 %. Such models provide excellent fits to current data and, as explained in [86], are also in agreement with LSS.

Other models, for larger n and Ω_h or lower z_{der} , show only a marginal fit with current observations. Hopefully, future data on high l 's will be more restrictive and allow safer constraints. At present, such models cannot be ruled out, although they are more discrepant from pure CDM and $n = 1$ than high l data require.

In our opinion, however, CBR data can already be said to exclude a number of models which fitted LSS data. In general, models with $n > 1.3$ and $z_{der} < 1000$ seem out of the range of reasonable expectations.

Altogether, three kinds of departures from CDM and Zel'dovich were considered:

large Ω_h , low z_{der} and $n > 1$. Large (but allowed) Ω_h values, by themselves, do not ease the agreement of models with high l data. Taking $n > 1$ eases the agreement of models with data for $l \sim 200$, as is expected, but seems to rise the angular spectrum above data for greater l 's. Taking low z_{der} , instead, raises the doppler peak, but does not spoil the agreement with greater l data. Current data, therefore, seems to support models with a limited amount of HDM or volatile materials, possibly in association with n slightly above unity, to compensate some effects on LSS.

Note that the analysis of this work is carried out keeping $h = 0.5$, allowing for no cosmological constant, and constraining the total density to be critical. E.g., raising h would probably allow and require a stronger deviation from pure CDM and $n = 1$. We plan to widen our analysis of the parameter space in the near future, also in connection with the expected arrival of fresh observational data on the CBR spectrum.

4.7 Light gravitinos warm dark matter

In analyzing warm dark matter models, our procedure was the following. The amplitude A of the power spectrum ($P(k) = AT^2(k)k^{n_{pr}}$) is determined by following the recipe by Bunn & White [194] to normalize both low-density flat and open models to the 4-year *COBE* data. Here we did not consider the case of non-negligible contribution of tensor mode fluctuations to the CMB anisotropies. Indeed, such an effect would lead to a smaller spectrum amplitude, with a subsequent delay of the galaxy formation epoch that, as we will see, represents a major problem for WDM-dominated models.

For each model, the corresponding free-streaming mass scale was computed and from fig.4.1 it is apparent that such a scale is always at least of the order of a large galaxy halo. The flattening of σ_M at small masses represents the imprint of non-hierarchical clustering. On the other hand, it turns out that the behaviour on the scales of galaxy clusters, $\sim 10^{15}h^{-1}M_\odot$, is rather similar to that of the CDM-dominated case. In the following we will use the abundance of local galaxy clusters and of high-redshift protogalaxies, through data about damped Ly- α systems, to constrain the whole class of WDM-dominated models. Constraints on larger scales, like bulk-flows data [138, 195], are much more similar to the CDM case.

The first constraint that we consider comes from the abundance of neutral hydrogen (HI) contained within damped Ly- α systems.

Even in this case, we considered the results reported by Storrie-Lombardi et al. [148] at redshift $z \simeq 4.25$ and assumed that all the HI gas at that redshift is involved

in the absorbers.

In our analysis, we considered $\delta_c(z)$ in eq.(4.8) as the critical density contrast whose value predicted by the model for the collapse of a spherical top-hat fluctuation in a critical density universe, $\delta_c = 1.69$ independent of the redshift. This value has been confirmed by N-body simulations [143]. We used the expressions for $\delta_c(z)$ provided in ref.[196] for both low-density flat and open universes. We note, however, that at the redshift $z=4.25$, that we are considering, the resulting δ_c value is always very close to 1.69.

We note that the Press & Schechter approach [141], on which eq. (4.8) is based, holds only in the case of hierarchical clustering. In our case of WDM models, hierarchical clustering only takes place on mass scales larger than M_{fs} . On smaller scales, the lack of fluctuations causes the flattening of σ_M . Therefore, by estimating σ_M at arbitrarily small masses, one obtains the r.m.s. fluctuations at the free-streaming mass scale. In our approach, we will give up the dependence on mass scale M , which amounts to assume that DLASs are hosted within protostructures of mass of about M_{fs} ; protostructures of smaller mass, instead, are produced later by fragmentation of larger lumps.

In the light of all the above uncertainties in directly relating Ω_g to Ω_{coll} , we prefer to maintain a conservative approach here and to consider a model as ruled out if it predicts Ω_g to be less than the observational 1σ lower limit. At this level of comparison we do not consider as reliable to put constraints to model producing too high a Ω_g value.

Furthermore, we should also rescale appropriately the value by Storrie-Lombardi to include the more general $\Omega_0 < 1$ cases. Therefore, the limiting value that we consider is

$$\Omega_g = 0.0009 h^{-1} f(\Omega_0, \Omega_\Lambda, z = 4.25), \quad (4.11)$$

where

$$\begin{aligned} f(\Omega_0, \Omega_\Lambda, z) &= \left(\frac{1 + \Omega_0 z}{1 + z} \right)^{1/2} ; & \Omega_\Lambda &= 0 \\ f(\Omega_0, \Omega_\Lambda, z) &= \frac{[(1 + z)^3 \Omega_0 + \Omega_\Lambda]^{1/2}}{(1 + z)^{3/2}} ; & \Omega_\Lambda &= 1 - \Omega_0. \end{aligned} \quad (4.12)$$

As for the cluster abundance, it has been recognized to be a sensitive constraint on the amplitude of the power spectrum [161]. Based on the Press & Schechter approach [141], it is easy to recognize that the number density of clusters with mass exceeding a given value is exponentially sensitive to the r.m.s. fluctuation on the cluster mass scale. Fitting the local X-ray cluster temperature function with the

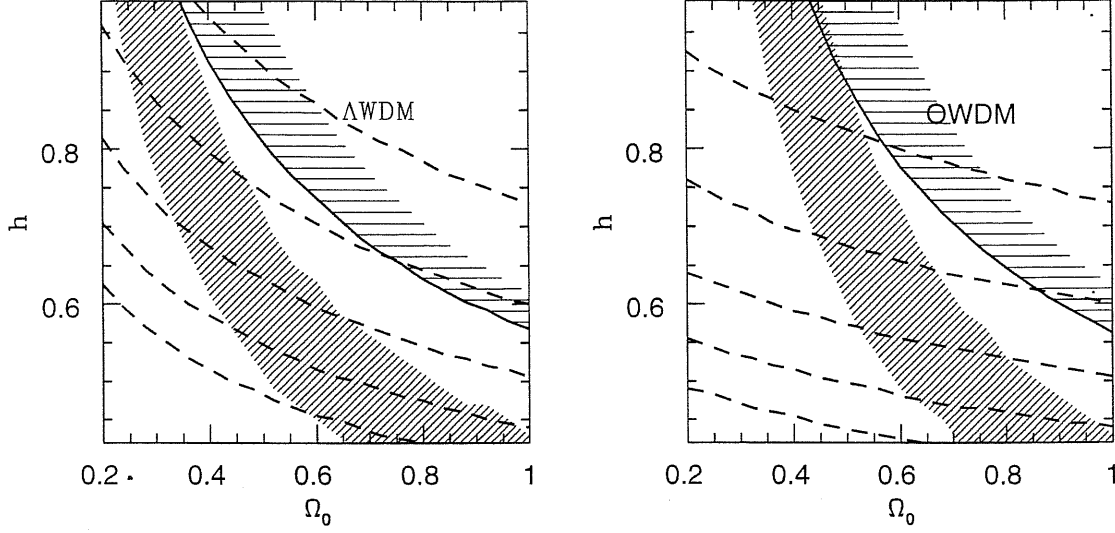


Figure 4.12: Observational constraints for *COBE*-normalized WDM models, with $g_* = 150$, on the (Ω_0, h) parameter space, for flat low-density (Λ WDM) and open (OWDM) models. The finely shaded area corresponds to the 95% c.l. region allowed by the cluster abundance, as estimated by Viana & Liddle (see text). The heavy solid curve delimiting the coarsely shaded area represents the limit of the region allowed by the data about the Ω_g in DLAS at $z = 4.25$, as given by Storrie-Lombardi et al. (see text); models lying below such curves are excluded. Horizontal dashed curves connect models having the same age of the Universe: $t_0 = 9, 11, 13, 15, 17$ Gyrs from upper to lower curves.

Press–Schechter approach led several authors to obtain rather stringent relationships between σ_8 , the r.m.s. fluctuation value within a top-hat sphere of $8 h^{-1} \text{Mpc}$ radius, and Ω_0 [169, 170, 197]. In the following we will resort to the constraint by Viana & Liddle, who provided the most conservative and, probably, realistic estimate of errors, mostly contributed by cosmic variance effects on the local cluster population:

$$\begin{aligned}
 \sigma_8 \Omega_0^{\alpha(\Omega_0)} &= 0.60^{+0.22}_{-0.16} \\
 \alpha(\Omega_0) &= 0.36 + 0.31\Omega_0 - 0.28\Omega_0^2 \quad ; \quad \Omega_\Lambda = 0 \\
 \alpha(\Omega_0) &= 0.59 - 0.16\Omega_0 + 0.06\Omega_0^2 \quad ; \quad \Omega_\Lambda = 1 - \Omega_0, \quad (4.13)
 \end{aligned}$$

with uncertainties corresponding to the 95% confidence level.

As for the purely WDM models, we plot in fig.4.12 the constraints on the (Ω_0, h) plane, for $g_* = 150$, from DLAS and cluster abundance. Only scale-free primordial spectra (i.e., $n_{pr} = 1$) are considered here. Left and right panels correspond to

the low-density flat (Λ WDM) and open (OWDM) cases, respectively. The solid line delimiting the coarsely shaded area indicates the limit for the region of the parameter space which is allowed by the observed Ω_g in DLASs: model lying below such curves should be considered as ruled out, since they produce a too small Ω_g value at $z = 4.25$. The cluster abundance constraint by eq.(4.13) is represented by the finely shaded region. The dashed curves connect models having the same age of the Universe: $t_0 = 9, 11, 13, 15$ and 17 Gyrs from upper to lower curves.

As a main result, we note that there is almost no overlapping between the regions allowed by the two observational constraints: for fixed values of the Hubble parameter, cluster abundance tends to select relatively smaller Ω_0 in order to satisfy the low-normalization request of eq.(4.13). On the other hand, the DLAS constraint favours higher density parameters, which has the effect of both decreasing the free-streaming scale and to increase the small-scale power even in the absence of any free-streaming. Judging from this plot, one would conclude that the whole class of gravitino-dominated WDM models would be ruled out by combining constraints on the cluster and on the galaxy mass scale. A residual possibility seems to exist to reach a concordance for $\Omega_0 \lesssim 0.4$ ($\Omega_0 \lesssim 0.5$) and a high Hubble parameter, $h \gtrsim 1$ ($h \gtrsim 0.9$) for OWDM (Λ WDM) models. However, two main problems arise in this case: (a) all the current determinations of the Hubble constant indicates $0.5 < h < 0.8$ [198]; (b) the resulting age of the Universe would be definitely too small, especially for OWDM models, even on the light of the new recalibration of globular cluster ages, based on the recent data from the Hypparcos satellite [199].

We also checked the possibility of considering non-scale-free primordial spectra ($n_{pr} \neq 1$), although results are not explicitly presented here. We verified that assuming either blue ($n_{pr} > 1$) or red ($n_{pr} < 1$) spectra does not improve the situation. In the first case, power is added on small scales, with the result that smaller Ω_0 are allowed by DLASs. However, the price to be paid is a rapid increase of the cluster abundance, that also pushes toward smaller Ω_0 the finely shaded area. As for red spectra, the opposite situation occurs: the reduction of small-scale power leads both constraints to favour relatively larger Ω_0 values, with no overlapping with the two allowed regions of the (Ω_0, h) plane ever attained.

As a matter of fact, the situation becomes even worse when considering $\Omega_0 = 1$ WHDM models. Results for this class of models are reported in fig.4.13 on the (Ω_ν, n_{pr}) plane. Left and right panels are for $h = 0.5$ and 0.6 , respectively; smaller h values are disfavoured by H_0 determinations, while larger values are constrained by the age of the Universe. In both cases the regions allowed by DLAS and cluster

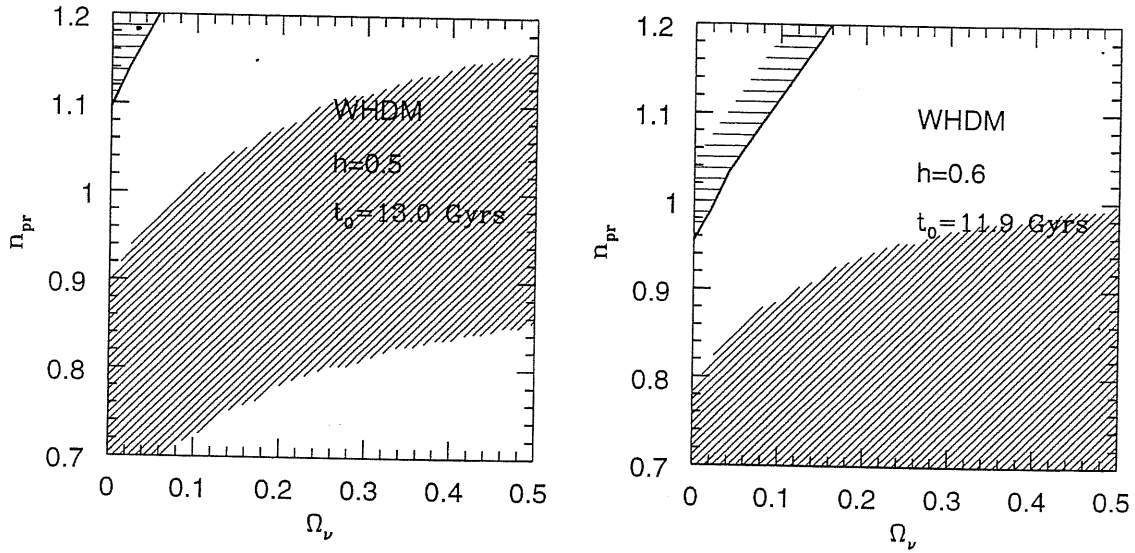


Figure 4.13: Observational constraints for *COBE*-normalized WHDM models, with $g_* = 150$, on the (Ω_ν, n_{pr}) plane, for $h = 0.5$ (left panel) and $h = 0.6$ (right panels). A vanishing tensor mode contribution to CMB temperature anisotropies is assumed for $n_{pr} < 1$ models. The two shaded areas have the same meaning as in fig.4.12.

abundance are largely disjointed, especially as higher Ω_ν are considered. Indeed, increasing the neutrino fraction has the effect of further reducing the power on small scales, thus further suppressing the high-redshift galaxy formation.

Based on such results we should conclude that none of the variants of the WDM gravitino-dominated scenario is able to account at the same time for the relatively small abundance of clusters at low redshift and for the relatively high Ω_g in collapsed structures at high redshift. It is worth reminding that this result has been obtained with the rather conservative choice of $g_* = 150$. As we have shown in the previous section, more realistic value of g_* should be even smaller, thus putting WDM-dominated model in an even worse shape.

Which are the consequences of such results on the low-energy SUSY breaking models that we described in Chapter 1? Of course, a first possibility is that gravitinos were so light as to be irrelevant from the point of view of cosmic structure formation. For instance, the current understanding of high-energy physics phenomenology would surely allow for $m_{\tilde{G}} \sim 1$ eV. In this case, $\Omega_{\tilde{G}}$ would be negligible. Of course, since \tilde{G} represents the LSP, the source for a cold DM component should

be found in this case outside the spectrum of SUSY particles (e.g., axions).²

On the other hand, if a scenario with $m_{\tilde{G}} \sim 100$ eV will turn out to be preferred, a non-negligible $\Omega_{\tilde{G}}$ can not be escaped. In this case, three possible alternative scenarios can be devised. The first one is to allow for cold + warm DM. However, since gravitinos have a much smaller free-streaming scale than neutrinos with $m_\nu \sim 5$ eV, this scenario would suffer from the same pitfalls of the standard CDM one, unless one takes $\Omega_0 < 1$. The second possibility would be to have a substantially larger g_* , so that gravitinos behave much like CDM. However, as we have seen in Section 2.2, it is not clear how a substantially larger g_* can be attained within plausible SUSY models. The third possibility would be to abandon the assumption of Gaussian fluctuations in favour of texture seeded galaxy formation [201], which would ease the formation of high redshift objects. However, also this possibility has been recently shown to suffer from serious troubles in producing a viable power spectrum of density fluctuations [202], which make texture-based models as virtually ruled out.

One may argue that the gravitino abundances will be diluted to a cosmologically negligible level by late-time entropy production. On the other hand, as the low value of g_* suggests, the reheat temperature after the entropy production should be lower than the electro-weak scale to avoid the re-thermalization of the gravitinos, which severely constraints possible ways to generate the baryon asymmetry of the Universe.

²See however a recent proposal that a sneutrino in the messenger sector can be a CDM candidate[200].

Model	σ_8	Γ	$N(> M)$	Ω_g
Observ.	0.90 ± 0.05	0.25 ± 0.05	(4-6)	2.2 ± 0.5
1	1.05	0.30	36	8.7
2	1.23	0.34	53	11
3	1.23	0.35	53	10
4	0.87	0.19	19	1.4
5	1.10	0.25	40	3.2
6	1.23	0.33	53	5.1
7	0.76	0.13	11	4E-02
8	1.02	0.21	33	0.6
9	1.22	0.36	52	2.3
10	0.68	0.10	6.1	4E-05
11	0.96	0.18	28	2E-03
12	1.29	0.53	60	0.8
13	0.62	0.08	3.4	1E-11
14	0.95	0.21	27	1E-04
15	1.27	0.59	58	0.3
CDM	1.33	0.47	62	30
CHDM	0.86	0.16	18	1E-02
16	1.03	0.28	34	6.0
17	1.20	0.31	50	8.8
18	1.26	0.33	55	8.9
19	0.81	0.16	14	0.4
20	1.05	0.21	36	1.9
21	1.26	0.30	55	4.3
22	0.74	0.10	9.1	3E-03
23	1.01	0.18	32	0.2
24	1.21	0.35	51	1.8
25	0.64	0.08	3.9	2E-07
26	0.95	0.17	27	4E-03
27	1.27	0.48	59	0.8
28	0.60	0.07	2.5	2E-15
29	0.93	0.14	24	2E-06
30	1.19	0.53	51	0.1
CDM	1.28	0.44	58	20
CHDM	0.82	0.15	15	6E-03

Table 4.1: Volatile models with radiative decay: statistical properties of large-scale structure. Col. 2: r.m.s. fluctuations within a top-hat sphere of $8 h^{-1}\text{Mpc}$ radius. Observational result refers to the APM galaxy distribution in real space. Col. 3: ‘extra power’ parameter; observational result from Peacock & Dodds (1994). Col. 4: number density of clusters with mass $M > 4.2 \times 10^{14} h^{-1} M_\odot$ (units of $10^{-6} (h^{-1}\text{Mpc})^{-3}$). Lower and upper values for the observational result are from White, Efstathiou & Frenk (1993) and Biviano et al. (1993), respectively. Col. 5: fractional density of neutral gas within collapsed structures of mass $5 \times 10^{10} h^{-1} M_\odot$ at $z = 4.25$ (units of 10^{-3}); the Gaussian window with $\delta_c = 1.5$ is assumed;

Ω_h	d	n	$N_{\nu,eff}$	σ_8	Γ	$N(> M)$
$\Omega_b = 0.05$						
0.11	8	1	6.9	0.53–0.68	0.23	1.8–9.8
0.11	8	1.1	6.9	0.63	0.27	6.9
0.16	2.83	1	5	0.60–0.68	0.20	4.0–9.3
0.16	2.83	1.1	5	0.67	0.24	8.9
0.11	16	1.1	10.7	0.52–0.64	0.24	1.6–7.3
0.19	8	1.1	9.7	0.55–0.66	0.16	2.0–7.7
0.19	8	1.2	9.7	0.55–0.67	0.19	2.1–8.1
0.20	4	1.2	6.5	0.67	0.20	8.3
0.24	4	1.3	7.2	0.64–0.69	0.17	6.4–9.4
0.23	8	1.3	8.9	0.57–0.68	0.17	2.7–9.3
$\Omega_b = 0.1$						
0.11	8	1	6.9	0.52–0.65	0.21	1.4–7.6
0.11	8	1.1	6.9	0.58–0.67	0.24	3.6–8.9
0.16	2.83	1	5	0.66–0.68	0.18	7.4–9.0
0.16	2.83	1.1	5	0.60–0.65	0.21	4.4–7.1
0.11	16	1.1	10.7	0.47–0.67	0.22	1.0–7.9
0.19	8	1.1	9.7	0.57–0.68	0.14	2.9–8.7
0.19	8	1.2	9.7	0.49–0.67	0.17	1.0–8.0
0.20	4	1.2	6.5	0.66–0.68	0.13	7.1–8.0
0.24	4	1.3	7.2	0.54–0.69	0.14	1.6–8.8
0.23	8	1.3	8.9	0.52–0.70	0.15	1.2–10

Table 4.2: Model parameters and power spectra. Column 1: volatile fractional density; Column 2: redshift at which the volatile component becomes non-relativistic ($d = 10^4/z_{der}$); Column 3: total number of equivalent massless neutrinos ($N_{\nu,eff} = g_{\nu,eff}/2$); Column 4: n value considered; Columns 5–7: Large scale structure predictions.

Summary and Conclusions

This Thesis deals with the problem of structure formation and the dark matter content of the Universe. The problem of finding a model for structure formation that can account for all the observational tests is one of the most challenging problem in modern cosmology. It is well known that two main theories can be advocated in order to explain the observed dishomogeneities.

A first possibility consists in assuming that some topological defects act as seeds for the perturbations in the energy density. The topological defects scenario naturally leads to non-Gaussian perturbations, which some authors claim to be seen in COBE data ([203], note however that this result is in contrast with other results, see e.g. [204]). Defect models also allow to resurrect the possibility of hot and warm dark matter scenarios, in fact they provide a way to form structure on small scales where hot and warm dark matter scenario fail. Standard scaling defects models, however, seem to have big difficulties in matching both LSS and CMB data [205, 201], so that some variants of the basic scheme must be advocated. This is currently a subject of research.

The second possibility consists in assuming that the observed anisotropies originated by quantum fluctuations of the inflaton field in the early Universe. The basic inflationary paradigm implies that fluctuations have a Gaussian distribution, and predict a power-law initial power spectrum with spectral index close to one. Within the inflationary scenario, many different models for structure formation can be realized, just varying the matter content of the Universe and the nature of the dark matter. Large scale structure and CMB data can already discriminate between different dark matter models; for example it has been shown that the standard CDM model does not provide a viable scenario for structure formation.

The aim of this Thesis was to predict and test the structure formation in two different classes of dark matter models, namely the light gravitino dark matter and the volatile dark matter models. The motivations for these works rely on both

particle-physics and astrophysics.

As long as the light gravitino model is concerned, our first aim was to test the gauge-mediated SUSY breaking models, which predict the gravitino with a mass in the range $\simeq 100 \text{ eV} - 1 \text{ keV}$ to be the lightest SUSY particle. Therefore we analyzed the cosmological consequences of assuming the dark matter to be dominated by such light gravitinos. We pointed out that gravitinos with such a mass behave like warm dark matter (WDM), since their free-streaming mass scale is comparable to the typical galaxy mass scale. Since it has already been shown that pure WDM models with $\Omega_o = 1$ do not provide a viable scenario for structure formations, we analyzed some of its variants, namely we considered low Ω_o models with and without cosmological constant and Warm + Hot dark matter models (WHDM), with the hot component provided by a massive neutrino. We decided to study this latter case because, given the success of Cold + Hot dark matter models in reproducing the large scale structure, we wanted to test if WHDM models as well gave good results.

Our procedure was the following: after estimating the number of degrees of freedom of relativistic species at the gravitino decoupling, g_* , we resorted to a Boltzmann code to compute the appropriate WDM transfer functions. These were used as the starting point to compare gravitino-dominated model predictions to observational data about the abundance of HI within high-redshift damped Ly- α systems and about the abundance of local galaxy clusters.

The main results of our analysis can be summarized as follows.

- (a) Low-density WDM models with both flat (Λ CDM) and open (OCDM) geometry can not satisfy the two observational constraints at the same time, unless a rather small Ω_o value ($\lesssim 0.4$) and a rather large Hubble parameter ($\gtrsim 0.9$) are assumed. However, such requests would conflict with measurements of the Hubble constant and with current constraints about the age of the Universe.
- (b) As for warm + hot (WHDM) models, we found that they have an even harder time. The combined free-streaming of both neutrinos and gravitinos generates a strong suppression of fluctuations at $\sim 1 h^{-1} \text{ Mpc}$ scale. This makes extremely difficult to form high-redshift ($z \sim 4$) protogalactic objects if we require the model to match the low- z cluster abundance.

Based on such results we claim that no variant of a light gravitino DM dominated model is viable from the point of view of cosmic structure formation. Therefore, in the framework of GMSB models, this amounts to require the gravitino to be light enough ($m_{\tilde{G}} \lesssim 50 \text{ eV}$) so as to be cosmologically irrelevant. In this case, however, one would lose the LSP candidate for implementing a CDM-dominated scenario.

We then studied a class of mixed dark matter models in which the hot component is not provided by the standard massive stable neutrino, but is made of a particle produced in the decay of a heavier one (volatile models). Mixed models are at the moment among the best available theories for structure formation. In fact, their matter power spectra, when normalized to COBE, show less power of CDM on the galaxy cluster scale, which is desirable in order to not overproduce clusters, and at the same time still assure enough power on galaxy scale to form objects at an appropriate redshift. Volatile models mime the behaviour of standard mixed models, and are therefore potentially very interesting. Particle physics can provide a suitable framework for volatile models if extensions of the standard model are considered. We studied the case of both radiative and non-radiative two-body decay, and considered that the decay took place at very early times ($z \gtrsim 10^7$).

In the case of volatile models, the peculiar way hot dark matter particles are produced causes them to have a different phase-space distribution if compared to massive neutrinos whose original phase-space distribution is thermal. One of our aims was to test the relevance of this difference on the radiation and matter power spectra. We discussed the parameter space for the volatile case and compared the transfer functions for thermal and volatile HDM, for values of both the hot component abundance Ω_h and the derelativization redshift z_{der} which both models allow. Power spectra differences between thermal and volatile models are then really significant only as far as the sterile scalar eventually produced in non-radiative decays is concerned.

A second important feature of volatile models is that, owing to the production mechanism of the hot dark matter particle, the hot dark matter abundance Ω_h and the derelativization redshift z_{der} can be varied almost independently. As a consequence, volatile models with radiative decay are already different from standard CHDM models. Moreover, we pointed out that such feature allows in principle to realize models with a high Ω_h and a low z_{der} . Such a feature may help to alleviate the problem of the high baryon abundance observed in galaxy clusters. Our second aim was therefore to select the allowed region in the $\Omega_h - z_{der}$ plane, on the basis of large scale structure and CMB data.

Our procedure was the following: after evaluating the matter transfer function for volatile models with radiative and non-radiative decay, with $\Omega_o = 1$ and $h = 0.5$, we obtained the expected values of several observable quantities, which can be estimated using linear theory. In particular we worked out the expected cluster number density, the abundance of Damped Lyman α clouds (DLAS), the mass variances at 25 and

$8 h^{-1}\text{Mpc}$. From them we also estimated the extra power parameter Γ .

While analyzing volatile models with radiative decay, we found that the most stringent constraint comes from the requirement for a model to satisfy the observed abundance of high-redshift DLAS and of galaxy clusters at the same time. As for DLAS, the rather large value of the HI gas fraction involved in the absorbing systems, Ω_g , implies a substantial amount of power on galaxy scales, so as to favour models with a volatile abundance $\Omega_h \lesssim 0.2$. A larger volatile component would be allowed only resorting to a high value of z_{der} ($z_{der} \simeq 2.25 \times 10^5 \Omega_h$). On the other hand, models with small Ω_h and/or large z_{der} behave too much like the standard CDM model, drastically overproducing clusters.

Therefore, the overall result would be that models with $z_{der} \gtrsim 5.64 \times 10^4 \Omega_h$ have a hard time, quite independently of Ω_h . Among the models considered, the only model which passes all the tests is the one with $\Omega_h = 0.2$ and $z_{der} \simeq 4.5 \times 10^3$. This model should be also considered as a reference for further investigations, involving for example N-body simulations. Note, however, that our analysis has been based on assuming a scale-free primordial spectrum, while variations around this model are allowed by some classes of inflationary schemes. Taking $P(k) \propto k^n$, both $n < 1$ and $n > 1$ are viable variations. Allowing for $n < 1$ decreases the amount of power on the cluster mass scale, so as to alleviate the problem of cluster overproduction displayed by “colder” models. On the other hand, the case of “antitilting”, with $n \simeq 1.2$, has been considered in order to alleviate some of the problems of the CHDM scenario. However, the subsequent increase of power on small scales goes in the undesired direction as far as the cluster abundance is concerned.

While considering the non-radiative decay, we performed a similar large scale structure analysis, allowing also values of the spectral index $n \geq 1$.

Looking at large scale structure only, we found that the most stringent constraint comes from the extra power parameter Γ . Considering all constraints together, a wide portion of the parameter space Ω_h – z_{der} is allowed, also in conjunction with high n values. This is mainly due to the fact that for a given large k value, the matter fluctuation spectrum $P(k)$ increases with n but is damped for low derelativization redshifts z_{der} , so that these two effects tend to compensate.

However, when also CMB spectra are considered, a further restriction of the parameter space occurs, especially for high n and low z_{der} . In fact, C_l spectra display the following trend: for a given large l value, C_l increases with both n and $d = 10^4/z_{der}$. As a consequence, CBR spectra already disfavour $n = 1.3$ if $d \gtrsim 4$ ($z_{der} \lesssim 2500$) is considered. Volatile models with $n > 1.2$ are largely out

of the errorbars, and should be considered as scarcely viable. Nevertheless, even for $n = 1.2$, volatile models allow a higher first doppler peak without raising the following ones. This feature goes in the direction of a good data fit in the range $200 \leq l \leq 500$. Just as large n , also large d causes conflict with data, by itself. For example, models with $d = 16$ are disfavoured, even with low Ω_h and $n = 1.1$.

Therefore, the models that we would like to test with N-body simulations have n slightly larger than one, a moderate Ω_h (~ 0.2) and the highest d allowed by CMB data ($d = 2 - 4$).

Note that our analysis was carried out keeping $h = 0.5$, allowing for no cosmological constant (for mixed models with cosmological constant see e.g. [206]), and constraining the total density to be critical. For example, raising h would probably allow and require a stronger deviation from pure CDM and $n = 1$. We plan to widen our analysis of the parameter space in the near future, also in connection with the expected arrival of fresh observational data on the CBR spectrum.

Bibliography

- [1] E. Gawiser and J. Silk, *Science* **280**, 1405 (1998).
- [2] S. Colombi, S. Dodelson, and L. Widrow, *ApJ* **458**, 1 (1996).
- [3] C. Burigana *et al.*, *A&ASS* **130**, 551 (1998).
- [4] P. Peebles, in *Principles of Physical Cosmology* (Princeton University Press, ADDRESS, 1993).
- [5] J. Mather *et al.*, *ApJ* **420**, 439 (1994).
- [6] D. Fixen *et al.*, *ApJ* **473**, 576 (1996).
- [7] S. Carroll, W. Press, and E. Turner, *A.R.A.A.* **30**, 499 (1992).
- [8] S. Perlmutter *et al.*, *Nature* **391**, 1 (1998).
- [9] S. Perlmutter *et al.*, *ApJ* in press (1998).
- [10] G. Garavich *et al.*, *ApJ* **493**, L53 (1998).
- [11] R. Daly, E. Guerra, and L. Wan, *astro-ph/9803265*, (1998).
- [12] M. White, *astro-ph/9802295*, (1998).
- [13] B. Chaboyer, P. Demarque, P. Kernan, and L. Krauss, *Science* **271**, 957 (1996).
- [14] H. Maoz and D. Riz, *ApJ* **416**, 425 (1993).
- [15] C. Kochanek, *ApJ* **457**, 228 (1996).
- [16] A. Guth, *Phys. Rev.* **D23**, 347 (1981).
- [17] A. Linde, *Phys. Lett.* **108B**, 389 (1982).

- [18] A. Albrecht and P. Steinhardt, Phys. Rev. Lett. **48**, 1220 (1982).
- [19] A. Liddle and D. Lyth, Phys. Rep. **231**, 1 (1993).
- [20] D. Lyth, Phys. Rev. **D31**, 1792 (1985).
- [21] S. Mollerach, S. Matarrese, and F. Lucchin, Phys. Rev. **D50**, 4835 (1994).
- [22] A. Linde, Phys. Lett. **B249**, 18 (1991).
- [23] A. Linde, Phys. Lett. **B259**, 38 (1991).
- [24] A. Linde, Phys. Rev. **D49**, 748 (1994).
- [25] E. Copeland *et al.*, Phys. Rev. **D49**, 6410 (1994).
- [26] Q. Shafi and A. Vilenkin, Phys. Rev. Lett. **52**, 691 (1984).
- [27] S. Pi, Phys. Rev. Lett. **52**, 1725 (1984).
- [28] Y. Fukuda *et al.*, **hep-ph/9807003**, (1998).
- [29] G. Jungman, M. Kamionkowski, and K. Griest, Phys. Rep. **267**, 195 (1996).
- [30] M. Dine, A. Nelson, Y. Nir, and Y. Shirman, Phys. Rev. **D53**, 2658 (1996).
- [31] J. Ellis, J. Kim, and D. Nanopoulos, Phys. Lett. **B145**, 181 (1984).
- [32] R. Juszkiewicz, J. Silk, and Z. Stebbins, Phys. Lett. **B158**, 463 (1985).
- [33] D. N. J. Ellis and S. Sarkar, Nucl. Phys. **B259**, 175 (1985).
- [34] V. Berezhinsky, Phys. Lett. **B261**, 71 (1991).
- [35] M. Kawasaki and T. Moroi, Prog. Theor. Phys. **93**, 879 (1995).
- [36] H. M. T. Moroi and M. Yamaguchi, Phys. Lett. **B303**, 289 (1993).
- [37] P. data group, Phys. Rev. **D54**, 1 (1996).
- [38] D. Chung, E. Kolb, and A. Riotto, **astro-ph/9805473**, (1998).
- [39] H. Nilles, Phys. Rep. **110**, 1 (1984).
- [40] M. Dine, W. Fischler, and M. Srednicki, Nucl. Phys. **B189**, 575 (1981).
- [41] S. Dimopoulos and S. Raby, Nucl. Phys. **B192**, 353 (1981).

- [42] M. Dine and W. Fischler, Phys. Lett. **B110**, 227 (1982).
- [43] M. Dine and M. Srednicki, Nucl. Phys. **B202**, 238 (1982).
- [44] L. Alvarez-Gaume, M. Claudson, and M. Wise, Nucl. Phys. **B207**, 96 (1982).
- [45] C. Nappi and B. Ovrut, Phys. Lett. **B113**, 175 (1982).
- [46] M. Dine and A. Nelson, Phys. Rev. **D48**, 1277 (1993).
- [47] M. Dine, A. Nelson, and Y. Shirman, Phys. Rev. **D51**, 1362 (1995).
- [48] A. de Gouvêa, T. Moroi, and H. Murayama, **hep-ph/9701244**, (1997).
- [49] S. Ferrara, L. Girardello, and F. Palumbo, Phys. Rev. **D20**, 403 (1979).
- [50] K.-I. Izawa, Y. Nomura, K. Tobe, and T. Yanagida, **hep-ph/9705228**, (1997).
- [51] Y. Nomura and K. Tobe, **hep-ph/9708377**, (1997).
- [52] E. Kolb and M. Turner, in *The Early Universe*, edited by F. in Physics Vol. 70 (Addison Wesley, Chicago IL, ADDRESS, 1990).
- [53] H. Pagels and J. Primack, Phys. Rev. Lett. **48**, 233 (1982).
- [54] M. Carena *et al.*, Nucl. Phys. **B503**, 387 (1997).
- [55] S. Park, in *"Search for New Phenomena in CDF", 10th Topical Workshop on Proton-Antiproton Collider Physics*, edited by R. Raja and J. Yoh (AIP Press, ADDRESS, 1995).
- [56] S. Dimopoulos, M. Dine, S. Raby, and S. Thomas, Phys. Rev. Lett. **76**, 3494 (1996).
- [57] S. Ambrosanio *et al.*, Phys. Rev. Lett. **76**, 3498 (1996).
- [58] S. Ambrosanio *et al.*, Phys. Rev. **D54**, 5395 (1996).
- [59] S. Dimopoulos, S. Thomas, and J. Wells, Phys. Rev. **D54**, 3283 (1996).
- [60] K. Babu, C. Kolda, and F. Wilczek, Phys. Rev. **77**, 3070 (1996).
- [61] J. Lopez and D. Nanopoulos, Mod. Phys. Lett. **A11**, 2473 (1996).
- [62] J. Lopez and D. Nanopoulos, Phys. Rev. **D55**, 4450 (1997).

- [63] P. Peebles, *Astrophys. J.* **258**, 415 (1982).
- [64] J. Bond, A. Szalay, and M. Turner, *Phys. Rev. Lett.* **48**, 1636 (1982).
- [65] K. Olive and M. Turner, *Phys. Rev.* **D25**, 213 (1982).
- [66] S. Borgani, A. Masiero, and M. Yamaguchi, *Phys. Lett.* **B386**, 189 (1996).
- [67] M. Kawasaki, N. Sugiyama, and T. Yanagida, *Mod. Phys. Lett.* **A12**, 1275 (1997).
- [68] E. Pierpaoli, S. Borgani, A. Masiero, and M. Yamaguchi, *Phys. Rev.* **D57**, 2089 (1998).
- [69] G. Dvali, G. Giudice, and A. Pomarol, *Nucl. Phys.* **B478**, 31 (1996).
- [70] K. Assamagan *et al.*, *Phys. Rev.* **D53**, 6065 (1996).
- [71] D. Buskalic *et al.*, *Phys. Lett.* **B349**, 585 (1995).
- [72] R. Kolb and M. Turner, *Phys. Rev. Lett.* **62**, 509 (1989).
- [73] S. Bonometto, F. Gabbiani, and A. Masiero, *Phys. Rev.* **D49**, 3918 (1994).
- [74] S. Borgani, A. Masiero, and M. Yamaguchi, *Phys. Lett.* **B386**, 189 (1996).
- [75] S. Ghizzardi and S. Bonometto, *A&A* **307**, 697 (1996).
- [76] E. Pierpaoli and S. Bonometto, *A & A* **300**, 13 (1995).
- [77] E. Pierpaoli, P. Coles, S. Bonometto, and S. Borgani, *ApJ* **470**, 92 (1996).
- [78] C. Burigana, G. D. Zotti, and L. Danese, *ApJ* **379**, 1 (1991).
- [79] K. Olive, G. Steigman, and E. Skillman, *ApJ* **483**, 788 (1997).
- [80] C. Ma and E. Bertschinger, *ApJ* **455**, 7 (1995).
- [81] H. Kodama and M. Sasaki, *Prog. Theor. Phys. Suppl.* **78**, 1 (1984).
- [82] V. Mukhanov, H. Feldman, and R. Brandenberger, *Phys. Rep.* **215**, 205 (1992).
- [83] P. Peebles, in *The Large Scale Structure of the Universe* (Princeton University Press, ADDRESS, 1980).
- [84] W. Press and S. Teukolsky, in *Numerical Recipes in Fortran* (PUBLISHER, ADDRESS, 1992).

- [85] J. Bond and A. Szalay, *ApJ* **274**, 443 (1983).
- [86] S. Bonometto and E. Pierpaoli, *New Astronomy* **3**, 391 (1998).
- [87] E. Pierpaoli and S. Bonometto, *M.N.R.A.S.*, submitted `astro-ph/9806037`, (1998).
- [88] J. Bardeen, J. Bond, N. Kaiser, and A. Szalay, *ApJ* **304**, 15 (1986).
- [89] S. Bonometto and R. Valdarnini, *Phys. Lett.* **A103**, 369 (1984).
- [90] R. Valdarnini and S. Bonometto, *A&A* **146**, 235 (1985).
- [91] S. Bonometto and R. Valdarnini, *ApJ* **299**, L71 (1985).
- [92] S. A. F. Occhionero and R. Scaramella, *ApJ* **299**, 577 (1985).
- [93] J. Holtzman, *ApJS* **71**, 1 (1989).
- [94] R. Schaefer, Q. Shafi, and F. Stecker, *ApJ* **347**, 575 (1989).
- [95] A. vanDalen and R. Schaefer, *ApJ* **398**, 33 (1992).
- [96] R. Schaefer and Q. Shafi, *Nature* **359**, 199 (1992).
- [97] M. Davis, F. Summers, and D. Schlegel, *Nature* **359**, 393 (1992).
- [98] J. Holtzman and J. Primack, *ApJ* **405**, 428 (1993).
- [99] A. Klypin, J. Holtzman, J. Primack, and E. Regös, *ApJ* **415**, 1 (1993).
- [100] M. Kawasaki, N. Sugiyama, and T. Yanagida, *Mod. Phys. Lett.* **A12**, 1275 (1997).
- [101] J. Primack, in *Proceeding of the Princeton 20th Century Anniversary Conference, Critical Dialogues in Cosmology*, edited by N. Turok (World Scientific, ADDRESS, 1997).
- [102] D. Y. Pogosyan and A. Starobinski, *ApJ* **447**, 465 (1995).
- [103] H. Reeves, *Rev. Mod. Phys.* **66**, 193 (1994).
- [104] T. Walker *et al.*, *ApJ* **376**, 51 (1991).
- [105] K. Olive and S. Scully, *ApJ* **446**, 272 (1995).
- [106] N. Hata *et al.*, *Phys. Rev. Lett.* **75**, 3977 (1995).

- [107] K. Gorski *et al.*, ApJ **430**, L89 (1994).
- [108] E. W. G. Smoot, C. Bennett, and P. Lubin, ApJ **436**, 443 (1994).
- [109] K. Gorski, R. Stompor, and A. Banday, **astro-ph/9502033**, (1995).
- [110] H. Lin *et al.*, ApJ **471**, 617 (1996).
- [111] U. Seljak and M. Zaldarriaga, ApJ **469**, 437 (1996).
- [112] W. Hu, D. Scott, N. Sugiyama, and M. White, Phys. Rev. **D52**, 5498 (1995).
- [113] W. Hu and N. Sugiyama, ApJ **444**, 489 (1995).
- [114] W. Hu, in *Wandering in the Background: A Cosmic Microwave Background explorer*, edited by P. thesis (Univ. of California at Berkeley, ADDRESS, 1995).
- [115] R. Sachs and A. Wolfe, ApJ **147**, 63 (1967).
- [116] S. Dodelson, E. Gates, and A. Stebbins, ApJ **467**, 10 (1996).
- [117] G. deGasperi, P. Muciaccia, and N. Vittorio, ApJ **439**, 1 (1995).
- [118] S. Burns, **astro-ph/9711304**, (1997).
- [119] S. Dodelson, G. Gyuk, and M. Turner, Phys. rev. Lett. **72**, 3754 (1994).
- [120] S. Bharadwaj and S. Sethi, ApJS **114**, 37 (1998).
- [121] S. McNally and J. Peacock, M.N.R.A.S. **277**, 143 (1995).
- [122] S. Hannestad, **astro-ph/9804053**, (1998).
- [123] J. Adams, S. Sarkar, and D. Sciama, M.N.R.A.S., submitted **astro-ph/9805108**, (1998).
- [124] S. Dodelson, E. Gates, and M. Turner, Science **274**, 69 (1996).
- [125] M. White, G. Gelmini, and J. Silk, Phys. Rev. **D51**, 2669 (1995).
- [126] R. Lopez, S. Dodelson, R. Scherrer, and M. Turner, **astro-ph/9806116**, (1998).
- [127] S. Hannestad, **astro-ph/9804075**, (1998).
- [128] C. Netterfield *et al.*, ApJ **474**, 47 (1997).

- [129] C. Bennet *et al.*, ApJ **464**, L1 (1996).
- [130] P. Scott *et al.*, ApJ **461**, L1 (1996).
- [131] G. Efstathiou, J. Bond, and S. White, M.N.R.A.S. **258**, 1p (1992).
- [132] N. Sugiyama, ApJS **100**, 281 (1995).
- [133] J. Peacock and S. Dodds, M.N.R.A.S. **267**, 1020 (1994).
- [134] S. Borgani *et al.*, New Astr. **321**, 1 (1997).
- [135] A. Dressler *et al.*, ApJ **313**, 42 (1987).
- [136] S. Courteau, S. Faber, A. Dressler, and J. Willick, ApJ **412**, L51 (1993).
- [137] E. Bertschinger *et al.*, ApJ **364**, 370 (1990).
- [138] A. Dekel, A.R.A.A. **32**, 371 (1994).
- [139] T. Kolatt and A. Dekel, ApJ **479**, 592 (1997).
- [140] L. da Costa *et al.*, ApJ **468**, L5 (1996).
- [141] W. Press and P. Schechter, ApJ **187**, 452 (1974).
- [142] C. Lacey and S. Cole, M.N.R.A.S. **262**, 627 (1993).
- [143] C. Lacey and S. Cole, M.N.R.A.S. **271**, 676 (1994).
- [144] A. Klypin and G. Rhee, ApJ **428**, 399 (1994).
- [145] A. Wolfe, in *Relativistic Astrophysics and Particle Cosmology*, edited by A. C.W. and S. M.A. (New York Acad. Sci., New York, ADDRESS, 1993).
- [146] M. Bartelman and A. Loeb, ApJ **457**, 529 (1996).
- [147] S. Fall and Y. Pei, in *QSO Absorbtion Lines*, edited by B. Springer Verlag (PUBLISHER, ADDRESS, 1996).
- [148] L. Storrie-Lombardi, R. McMahon, M. Irwin, and C. Hazard, in *Proceeding of the ESO Workshop on QSO Absorbtion Lines*, edited by preprint astro-ph/9503089 (PUBLISHER, ADDRESS, 1995).
- [149] H. Mo and J. Miralda-Escudé, ApJ **430**, L25 (1994).
- [150] C. Ma and E. Bertschinger, ApJ **434**, L5 (1994).

- [151] G. Kauffmann and S. Charlot, *ApJ* **430**, L97 (1994).
- [152] A. Klypin, S. Borgani, J. Holtzman, and J. Primack, *ApJ* **444**, 1 (1995).
- [153] S. Borgani, F. Lucchin, S. Matarrese, and L. Moscardini, *M.N.R.A.S.* **280**, 749 (1996).
- [154] J. Gardner, N. Katz, L. Hernquist, and D. Weinberg, *ApJ* **486**, 42 (1997).
- [155] M. Haehnelt, M. Steinmetz, and M. Rauch, *ApJ* **495**, 647 (1997).
- [156] J. Prochaska and A. Wolfe, *ApJ* **487**, 73 (1997).
- [157] K. Lanzetta, A. Wolfe, and D. T. D.A., *ApJ* **440**, 435 (1995).
- [158] A. Wolfe, K. Lanzetta, C. Foltz, and F. Chaffee, **preprint**, (1995).
- [159] N. Katz, D. Weinberg, L. Hernquist, and J. Miralda-Escudé, *ApJ* **457**, L57 (1996).
- [160] G. Efstathiou and M. Rees, *M.N.R.A.S.* **230**, 5p (1988).
- [161] S. White, G. Efstathiou, and C. Frenk, *M.N.R.A.S.* **262**, 1023 (1993).
- [162] N. Bahcall and R. Cen, *ApJ* **398**, L1 (1992).
- [163] N. Bahcall and R. Cen, *ApJ* **398**, L81 (1992).
- [164] A. Biviano *et al.*, *ApJ* **411**, L13 (1993).
- [165] A. Evrard, C. Metzler, and J. Navarro, *ApJ* **469**, 494 (1996).
- [166] G. Squires *et al.*, *ApJ* **461**, 572 (1996).
- [167] J. Loveday, G. Efstathiou, S. Maddox, and B. Peterson, *ApJ* **442**, 457 (1995).
- [168] J. Henry and K. Arnaud, *ApJ* **372**, 410 (1991).
- [169] P. Viana and A. Liddle, *M.N.R.A.S.* **281**, 323 (1996).
- [170] V. Eke, S. Cole, and C. Frenk, *M.N.R.A.S.* **282**, 263 (1996).
- [171] J. Navarro, C. Frenk, and S. White, *M.N.R.A.S.* **275**, 720 (1995).
- [172] A. Zabludoff, J. Huchra, and M. Geller, *ApJS* **74**, 1 (1990).
- [173] M. Girardi *et al.*, *ApJ* **404**, 38 (1993).

- [174] S. Allen and A. Fabian, 1998 **astro-ph/9802219**, .
- [175] V. Eke *et al.*, **astro-ph/9802350**, .
- [176] C. Frenk, S. White, G. Efstathiou, and M. Davis, *ApJ* **351**, 10 (1990).
- [177] F. Adams *et al.*, *Phys. Rev. D* **47**, 426 (1993).
- [178] A. Liddle and D. Lyth, *Phys. Rep.* **231**, 1 (1993).
- [179] C. Bennet *et al.*, *ApJ* **430**, 423 (1994).
- [180] G. Tormen, L. Moscardini, F. Lucchin, and S. Matarrese, *ApJ* **411**, 16 (1993).
- [181] G. Dvali, Q. Shafi, and R. Schaefer, *Phys. Rev. Lett.* **73**, 1886 (1994).
- [182] F. Lucchin *et al.*, *ApJ* **459**, 455 (1996).
- [183] D. Pogosyan and A. Starobinsky, *ApJ* **447**, 465 (1995).
- [184] A. Shectman *et al.*, *APJ* **470**, 172 (1996).
- [185] A. Liddle *et al.*, *M.N.R.A.S.* **281**, 531 (1996).
- [186] S. White and C. Frenk, *APJ* **379**, 52 (1993).
- [187] U. Briel, J. Henry, and H. Bohringer, *APJ* **259**, L31 (1992).
- [188] L. David *et al.*, *APJ* **412**, 479 (1993).
- [189] T. Walker *et al.*, *APJ* **376**, 51 (1991).
- [190] S. White and A. Fabian, *M.N.R.A.S.* **273**, 73 (1995).
- [191] A. Evrard, *M.N.R.A.S.* **292**, 289 (1997).
- [192] S. D. Copi C.J. and T. M.S., *Science* **267**, 192 (1995).
- [193] M. Tegmark, *ApJ* **464**, L38 (1996).
- [194] E. Bunn and M. White, *ApJ* **480**, 6 (1997).
- [195] M. Strauss and J. Willick, *Phys. Rep.* **261**, 271 (1995).
- [196] T. Kitayama and Y. Suto, *ApJ* **469**, 480 (1996).
- [197] U. Pen, *ApJ* **498**, 60 (1998).

-
- [198] W. Freedman, in *Proceeding of the Princeton 20th Century Anniversary Conference, Critical Dialogues in Cosmology*, edited by N. Turok (World Scientific, ADDRESS, 1997).
- [199] R. Gratton *et al.*, ApJ **491**, 749 (1997).
- [200] S. Dimopoulos, G. Giudice, and A. Pomarol, Phys. Lett. **B389**, 37 (1996).
- [201] U. Pen, U. Seljak, and N. Turok, Phys. Rev. Lett. **79**, 1611 (1997).
- [202] R. Cen, ApJ **491**, 1 (1997).
- [203] P. Ferreira, J. Magueijo, and K. Gorsky, **astro-ph/9803256**, (1998).
- [204] A. Heavans, **astro-ph/9804222**, (1998).
- [205] A. Albrecht, R. Battye, and J. Robinson, Phys. Rev. Lett. **79**, 4736 (1997).
- [206] R. Valdarnini, T. Kahniashvili, and B. Novosyadlyj, **astro-ph/9804057**, (1998).